

REVIEW

Design of Solid Electrolytes with Fast Ion Transport: Computation-Driven and Practical Approaches

Muhammad Khurram Tufail^{1,2}, Pengbo Zhai¹, Mengyang Jia¹, Ning Zhao^{1*}, and Xiangxin Guo^{1*}

¹College of Physics, Qingdao University, 266071 Qingdao, China. ²College of Materials Science and Engineering, Qingdao University, 266071 Qingdao, China.

*Address correspondence to: n.zhao@qdu.edu.cn (N.Z.); xguo@qdu.edu.cn (X.G.)

For next-generation all-solid-state metal batteries, the computation can lead to the discovery of new solid electrolytes with increased ionic conductivity and excellent safety. Based on computational predictions, a new proposed solid electrolyte with a flat energy landscape and fast ion migration is synthesized using traditional synthesis methods. Despite the promise of the predicted solid electrolyte candidates, conventional synthetic methods are frequently hampered by extensive optimization procedures and overpriced raw materials. It is impossible to rationally develop novel superionic conductors without a comprehensive understanding of ion migration mechanisms. In this review, we cover ion migration mechanisms and all emerging computational approaches that can be applied to explore ion conduction in inorganic materials. The general illustrations of sulfide and oxide electrolyte structures as well as their fundamental features, including ion migration paths, dimensionalities, defects, and ion occupancies, are systematically discussed. The major challenges to designing the solid electrolyte and their solving strategies are highlighted, such as lattice softness, polarizability, and structural disorder. In addition to an overview of recent findings, we propose a computational and experimental approach for designing high-performance solid electrolytes. This review article will contribute to a practical understanding of ion conduction, designing, rapid optimization, and screening of advanced solid electrolytes in order to eliminate liquid electrolytes.

Introduction

Developing solid materials with fast ion migration is essential for conversion devices such as fuel cells, smart battery systems, and high-energy-density solid batteries for electric vehicles (EVs), which are vital to societal shifts toward renewable energy. Solid electrolytes have been regarded as a perfect alternative to organic liquid electrolytes due to their unique properties, including (a) the unwanted side reactions that happen in the liquid electrolyte system can be effectively controlled; (b) the application of the solid electrolytes is anticipated to increase the energy density and calendar life of batteries, enabling high-voltage cathodes and lithium metal anodes; (c) solid electrolytes are inflammable, which evades fire and leakage hazards; (d) a solid electrolyte has superior performance over a broad temperature range; (e) solid electrolytes have a broader electrochemical stability range than liquid electrolytes [1–5]. Solid electrolytes are expected to achieve high ionic conductivity, as well as a wide electrochemical window, good thermal and mechanical stability, and a stable interface between the electrolyte and the electrodes.

Based on the compositions, the solid electrolytes can be classified as oxides, sulfides, polymers, and composite electrolytes.

The oxide-based electrolyte has a modest ionic conductivity ($\sim 10^{-4} \text{ S cm}^{-1}$) but is stable against air [6,7]. The sulfide-based electrolyte has excellent ionic conductivity ($\sim 10^{-2} \text{ S cm}^{-1}$) due to the low electronegativity of sulfur (S), the weak interaction between the S and Li atoms, and the broadening of the lithium channels for migration, which also consequently lowers the activation barrier. The broad electrochemical window of sulfide-based electrolytes and low electronic conductivity will play an important role in developing all-solid-state batteries (ASSBs). However, sulfide-based electrolytes are highly sensitive to moist air and produce hydrogen sulfide (H_2S) gas, limiting their real-world application [8–12]. Polymer electrolytes exhibit low ionic conductivity, but their flexible character can deliver a good interface contact between the electrodes and electrolytes. Flexible ASSBs with composite electrolytes combine the benefits of both inorganic and polymer electrolytes, such as inorganic electrolytes as filler additives and polymer electrolytes as flexible components [13–15].

Research on solid electrolytes has been mainly motivated by the discoveries and designs of novel materials with higher ion conduction [16,17]. Currently, the ionic conductivity of solid electrolytes has been greatly improved, while other performances, such as mechanical properties and electrochemical

Citation: Tufail MK, Zhai P, Jia M, Zhao N, Guo X. Design of Solid Electrolytes with Fast Ion Transport: Computation-Driven and Practical Approaches. *Energy Mater. Adv.* 2023;4:Article 0015. <https://doi.org/10.34133/energymatadv.0015>

Submitted 26 September 2022
Accepted 31 December 2022
Published 28 February 2023

Copyright © 2023 Muhammad Khurram Tufail et al. Exclusive Licensee Beijing Institute of Technology Press. No claim to original U.S. Government Works. Distributed under a Creative Commons Attribution License (CC BY 4.0).

stability, are still far from the application requirements. New descriptors have been projected to achieve rational discoveries of new ion conductors by various high-throughput computational-based screenings [18–21], leading to the finding of new promising solid electrolytes [22–26]. The renewed focus on the critical ionic conductivity of ion conductors has also significantly benefited the novel strategy of developing new solid electrolytes.

Computing methodologies can effectively contribute to screening high-performance solid electrolytes by predicting the required system with specific properties such as mechanical properties and stable phases [23,27–31]. Nevertheless, the traditional synthetic approach requires substantial experimental work accompanied by the waste of raw materials. Therefore, the computation-assisted ion migration mechanism research and computation-directed discoveries of solid electrolytes are deemed promising strategies for quick screening and optimizing high-performance solid electrolytes. In addition, it is still challenging to investigate the ion migration mechanism of solid electrolytes at the atomic scale in experiments. Computational simulation can complement experiments by providing exclusive insight into the ion migration mechanism in a superionic conductor.

This review presents the recent progress of computational research of ion conduction mechanisms in different solid electrolytes. We also briefly introduced first-principles methods based on density functional theory (DFT), bond valence (BV), nudged elastic band method (NEB), and ab initio molecular dynamics (AIMD), followed by an outline of the computation findings aiming to design high-performance solid electrolytes. Then, we summarize the ion migration mechanisms of all representative oxide electrolytes, including perovskites, Na superionic conductors (NASICONs), garnets, and sulfide-based electrolytes [Thio-LISICON (lithium super ion conductor), Argyrodites, Li_3PS_4 , and $\text{Li}_{10}\text{GeP}_2\text{S}_{11}$ (LGPS) electrolytes], by analyzing point defects and ion hopping. In recent years, high-throughput theoretical approaches have led to new guidelines for materials discovery, which makes it possible to screening and optimization of novel solid electrolytes efficiently. Considering the application requirements, experimental strategies such as defect introduction, lattice softening, and lattice polarizability suggest novel electrolyte designs as well as an ion migration facilitative framework. The combined methodologies provide a unique perspective on the fundamental ion migration regardless of the ion species, offering a comprehensive guideline for the future development of solid electrolytes.

Conduction Mechanism

Defect chemistry and ion migration mechanism

The imperfection in the normal geometric alignment of the atoms is known as a defect. The crystallographic defects are responsible for the ion conduction mechanism. Defect chemistry is the first stage of understanding the ion conduction mechanism in solid electrolytes. There are several types of defects including line defects, point defects, planner defects, and volume defects. Among all the defects in crystal structures, point defects play a vital role in ion migration. The most common point defects are the Frenkel defects (the anion-based vacancies accompanied by an interstitial cation ion) and the Schottky defects (the cation-based vacancies accompanied by an anion vacancy). Defect engineering has been extensively discussed

in this section. Generally, the formation of defects can be classified into ionic vacancy and doping approaches. The defects play an important role because of the chemical and structural tailoring of solid electrolytes, such as the improvement of the ion migration kinetics, which has been summarized in Fig. 1. In addition, the point defects can also interrelate to produce localized clusters that have noteworthy effects on ion migration properties. Equation 1 is applied to calculate the formation energy of the point defects under the charge state:

$$\Delta H_{df} (E_F \{ \mu_i \}) = E_{d,q} - E_0 - \sum_i n_i \mu_i + q (E_V + E_F) \quad (1)$$

where ΔH_{df} is the formation energy, d is a defect in the charge state q , $E_{d,q}$ is the total amount of energy with respect to the supercell, and n_i and μ_i are the chemical potentials for spaces of atoms and its defects (i_{th}) with a respective number of removed or added atoms in the crystal system. E_V and E_F denoted the valence band maximum in bulk and Fermi level correlated to E_V , accordingly. In the case of the vacancy defects (atom removed), n_i is denoted with a negative sign. On the other hand side, if the defects are interstitial (atom added), n_i is denoted with a positive sign [32].

There are 3 common mechanisms of ion migration: defect (vacancy) mechanism where ions hop onto adjacent vacant sites, the interstitial mechanism in which ions move between the interstitial position, and the interstitialcy mechanism where neighboring lattice ions are displaced by migrating interstitial ions to other interstitial position. The ion diffusion via the interstitial and vacancy mechanisms comprises only one ion hops on an isolated sublattice, but interstitialcy mechanism involves 2 ions. Understanding ion conduction mechanisms in ionic conductors is vital because they can improve the concentration of charge-carrying defects or the concentration of possible lattice positions/sites by doping as well as substitution approaches. For example, in a cation vacancy mechanism-enabled conductor, introducing more charge-containing cation vacancy (donor doping) could improve the ionic conductivity, whereas adding more cation interstitial (acceptor doping) could boost the ionic conductivity with an interstitial mechanism-enabled material.

The practical determination of the migration properties which are proportional to defect concentration as a function of temperature and anion partial pressure. By using Brouwer's experiments, it is possible to determine how the defect concentration varies with anion partial pressure. DC (direct current) polarization analysis with blocking electrodes is also a fundamental method to determine which charge carriers contribute to bulk conductivity. Solid electrolytes could support ion migration, and defect concentration varies with temperature, which can be measured by defect formation energy. A cation conductor cannot always be classified into one of the aforementioned conduction mechanisms based on the defect extant. The difficulty arises partly because the naming and identification of defects is dependent on the chosen reference state. For example, Li ions occupy the interstitial octahedral and tetrahedral sites in cubic $[\text{Li}_7\text{La}_3\text{Zr}_2\text{O}_{12}$ (LLZO)] garnets in a disordered manner. Although these sites are interstitial in accordance with the anion framework, Li^+ on these sites is typically not indicated by the symbol as Li_i^+ , but unoccupied interstitial sites are referred to as V_{Li}^+ . Instead, unoccupied interstitial Li_i^+ is typically recommended to nonequilibrium sites in the conductive frameworks outside of the interstitial sites [33,34].

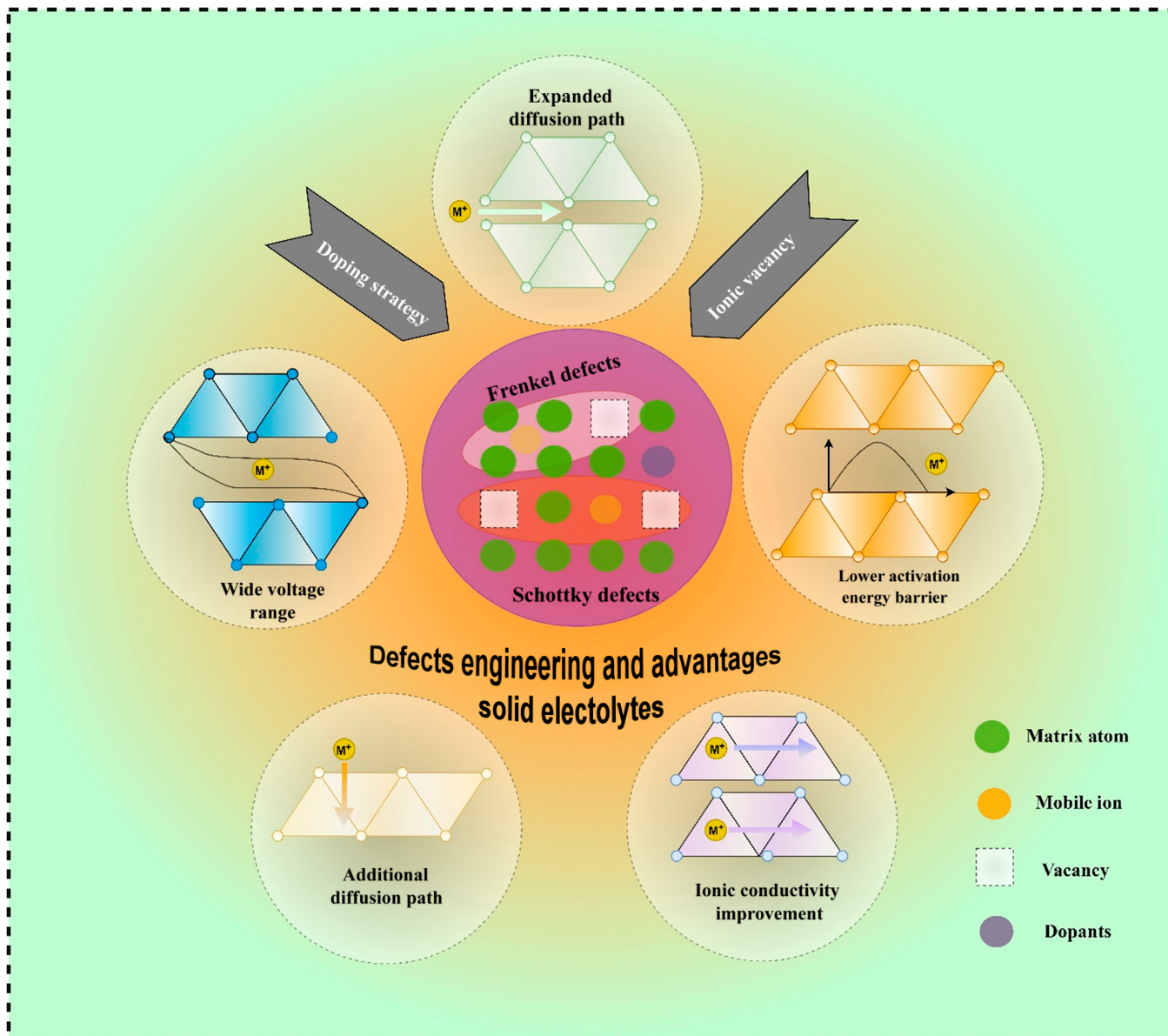


Fig.1. Defect engineering and advantages for the solid electrolytes.

Vacancy mechanism

In the vacancy mechanism, the ion can migrate from the prior equilibrium site of a nearby vacancy in order to achieve ion diffusion. The ion migration kinetic is mainly affected by the vacancy concentration in the crystal system, which can elaborate the ion migration channels and energy barriers for the additional vacancies in Fig. 2A. In order to further explain the vacancy-associated mechanism in the light of the LLTO ($\text{Li}_{0.5}\text{La}_{0.5}\text{TiO}_3$) example, the Li-ions are positioned on the A-site of the crystal structure. The Li-ion migrates via a bottleneck surrounded by the 4 oxygen ions to adjacent empty sites (3c) [35]. The Li-ion insertion process comprises 2 steps in which Li-ions could insert from the A-site into the vacancy due to least activation energy than 3c sites; then, the Li-ion would percolate in between the neighboring empty A-sites via bottleneck 3c sites, generating the rotational behavior of octahedral unit TiO_6 . The lithium concentration could affect the Li/La order in the structure, which can cause variation in the ion

conduction dominations. In Li-poor $\text{Li}_{3x}\text{La}_{(2/3-x)\cdot(1/3-2x)}\text{TiO}_3$ ($0.03 \leq x < 0.1$) perovskites, the ion migration is facilitated by 2D with the arrangements of Li/La atoms (Fig. 2B and C). In comparison, in the Li-rich $\text{Li}_{3x}\text{La}_{(2/3-x)\cdot(1/3-2x)}\text{TiO}_3$ ($0.1 \leq x < 0.167$) perovskites, the ion migration undergoes 3-dimensional (3D) disordered arrangements of Li/La [36,37]. Meanwhile, many other conduction mechanisms were proposed, but generally, the 3D conduction mechanism is considered to improve ion conduction in LLTO. The ion migration in the cubic garnet was also proposed to follow the vacancy mechanism. The oxygen vacancies could also be beneficial for ionic conductivity and limit the number of electron holes. Oxygen vacancies occur in cubic garnet and can significantly affect the cation defect formation, thus improving the Li-ion conductivity [38].

Interstitial mechanism

In interstitial or nonvacancy mechanism, the interstitial ion can directly migrate to a nearby interstitial position. Commonly,

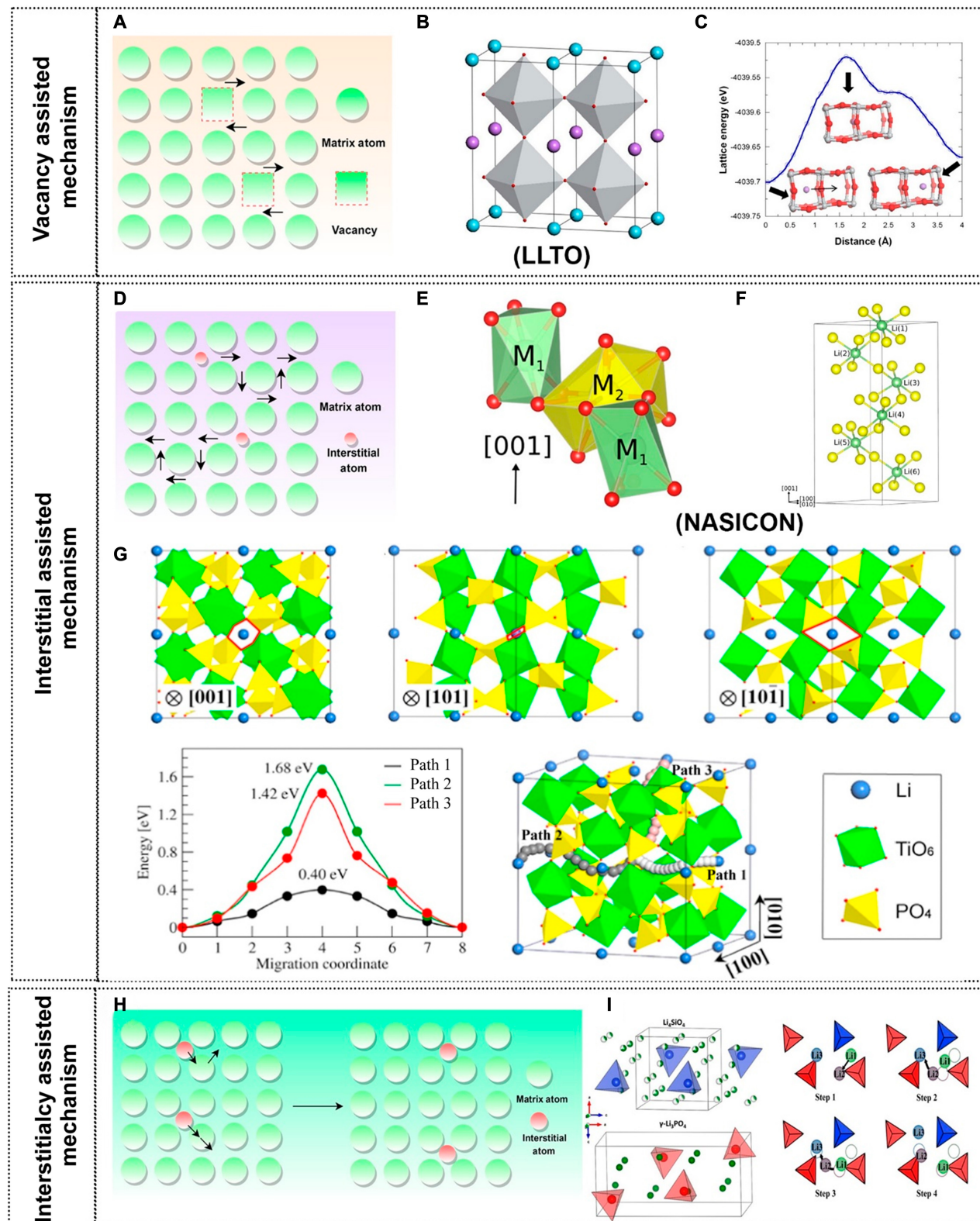


Fig. 2. (A) Representation of the vacancy-associated mechanism. (B) Perovskite/lithium lanthanum titanate oxide, TiO_6 octahedra (gray), lithium (purple ball), lanthanum (blue ball), and oxygen (red ball). (C) Energy barrier and their related structure of A-site Li^+ migrate in the perovskite crystal. Adopted with permission from [35]. Copyright 2015, American Chemical Society. (D) Illustration of the vacancy-associated mechanism. (E) M_1 and M_2 Li atom sites in the $\text{LiTi}_2(\text{PO}_4)_3$ crystal structure. (F) Migration channels for Li^+ in the $\text{LiTi}_2(\text{PO}_4)_3$ crystal structure comparing M_1 and M_2 sites. Adopted with permission from [39]. Copyright 2015, American Chemical Society. (G) Various demonstrations of $\text{LiTi}_2(\text{PO}_4)_3$ crystal along $[001]$, $[101]$ and $[\bar{1}01]$ directions in a first row; representation of Li-ion migration channels and their activation energies of paths 1, 2, and 3 according to the directions in the second row. Reprinted with permission from [40]. Copyright 2017, Elsevier. (H) Representation of the interstitialcy mechanism. (I) Structure of LISICON and the knock-on mechanism in $\text{Li}_{3.5}\text{Si}_{0.5}\text{P}_{0.5}\text{O}_4$, where the migration interstitial Li-ion transfers another Li-ion toward a neighbor site. Adopted with permission from [44]. Copyright 2015, American Chemical Society.

the interstitial ions are smaller in size than matrix atoms, and great lattice strain is produced during this mechanism. In this mechanism, the interstitial ion first hits the matrix atom and later migrates to another nearby interstitial site, as shown in Fig. 2D. The NASICON $M_{1+x}Al_xTi_{2-x}(PO_4)_3$ ($M = Li, Na$) conductors [39–42] are generally recognized as the interstitial-associated ion conduction mechanism. The mobile ions (Li, Na) in the NASICON conductor occupy the M1 site in between the PO_4 and TiO_6 polyhedra [39]. The Li-ions locate at position M1, which bonds with 6 O atoms. The second structural Li-ion (M2) position in between the 2 M1 sites along irregular 10-fold O-coordination is shown in Fig. 2E. The Li-ion movement in the crystal structure is motivated by thermally activated ion hopping between the interstitial sites. The arrangement of the conduction channels in an alternative pattern and the 3D ion diffusion network construct throughout the crystal structure are shown in Fig. 2F. There are 3 different probable pathways for the interstitial-associated M ion migration along the [001] and [101] and [$\bar{1}01$] directions in the MTi(PO_4)₃ system, as shown in Fig. 2G. When the vacancy is formed, the M-ions at neighboring 6b sites move to this empty site. For instance, in $LiTi_2(PO_4)_3$, dislocations for the neighboring lithium ions hopping to the lithium vacancy along 3 different directions are 6.10, 8.62, and 6.10 Å. The migration channels with [001], 101, and [$\bar{1}01$] directions show their respective migration activation energies. The activation energies for the lithium hopping of [001] [101] and [$\bar{1}01$] are calculated to be 0.40, 1.68, and 1.42 eV, showing that the Li^+ migration along path 1 is relatively more accessible than that along other paths. In the proposed migration path 1, Li^+ hops from the 6b site to nearby 6b empty vacancy by 18e (M2) sites are more efficient, as shown in Fig. 2G. In addition, the activation energy for the interstitial Li ion is calculated to be 0.25 eV in $LiTi_2(PO_4)_3$, which means that a common approach to improving conductivity in NASICONs is implementing interstitials rather than vacancies [40].

Interstitialcy mechanism

An interstitialcy mechanism (a kick-out mechanism), where the site ion is kicked out through interstitial ions, is shown in Fig. 2H [43]. There are at least 2 atoms in this mechanism migrating simultaneously. The LISICON-type ionic conductor is based on γ - Li_3PO_4 structure and a wide range of other possible compositions, including $Li_{2+2x}Zn_{1-x}GeO_4$ [31,44,45]. The standard structure could be designated as the Li-ion occupying the interstitial position between the tetrahedral framework.

γ - Li_3PO_4 exhibits orthorhombic symmetry along the Pnma space group. The P atoms are coordinated with 4 O atoms in a tetrahedral manner, as depicted in Fig. 2I. Solid solution of Li_3PO_4 - Li_4SiO_4 is the reference condition, which includes substantially extrinsic lithium interstitials, making interstitialcy the predominant mechanism. Both γ - Li_3PO_4 and Li_4SiO_4 are closely related to the LISICON conductor with the XO_4 -based tetrahedral units ($X = Si$ or P). An interstitial Li-ion knocks off a lattice Li-ion toward another nearby site, resulting in further facilitating Li-ion migration. The migrating interstitial Li-ion knock-on occurs when nearby Li-ion migrates into an interstitial position within the surrounding polyanion layer [44]. In contrast to the vacancy-assisted mechanism, the nonvacancy mechanism is more difficult due to the higher activation energy barrier. This cooperative process accelerates the Li-ion transport and improves the ionic conductivity in these mixed compositions.

Li-ion transport in the amorphous region

The free volume model commonly describes the ion migration mechanism in the amorphous region. The Li-ion is positioned at the appropriate coordination sites of the polymeric chain segments, for example, -CN in polyacrylate, -O- in the polyethylene oxide, and -NR in the polyimide. The polymeric chain experiences the local segment motions like a quasi-liquid with a little free volume around it. Consistently, the lithium-ion could hop from the solitary coordination site to another via free volume in the single polymeric chain or various chains under the electric field effects [46,47]. The ion migration in the solid polymer type of electrolytes primarily happens in the amorphous region above their T_g [48]. The relationship between ion conduction and temperature depending on the free volume model can be calculated and explained by the Vogel-Tamman-Fulcher (VTF) equation.

Li-ion migration is also associated with the degree of crystallinity in solid polymer electrolytes (SPEs). The lithium-ion transport in the crystalline phase is less dependent on the segmental motion as compared to polymeric material and is also explained by the Arrhenius equation. In fact, the ion migration kinetics of the amorphous region with a polymeric chain segment is much faster than that of the crystalline phase [49]. As shown in Fig. 3A to C, the crystalline phase and polymer segments of PEO: $LiXF_6$ ($X = P, As$) [49,50] and LiI [49,51] are folded to create the cylindrical tunnels for the lithium-ion, which are positioned at the -O- coordination sites of PEO and XF_6^- ($X = P, As$) anions. The lithium-ion can migrate along the cylindrical tunnels by neighboring coordinated sites without

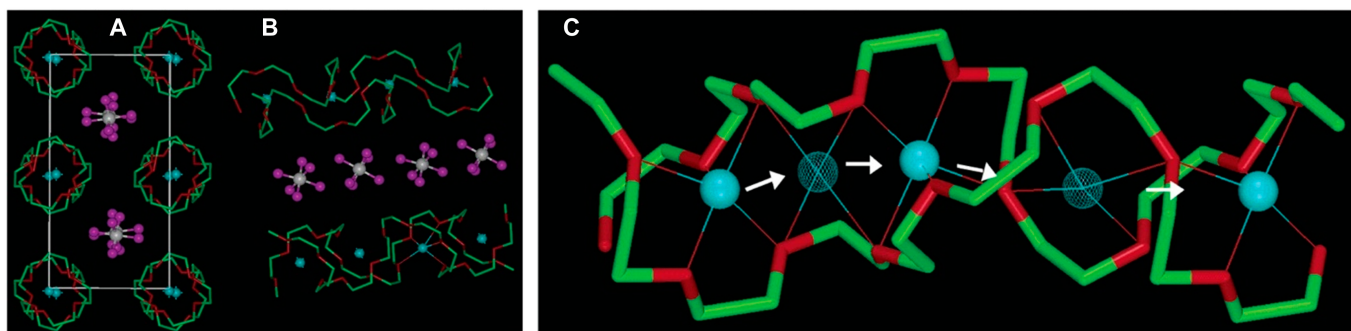


Fig. 3. The structural diagram of PEO₆:LiAsF₆. (A) Structural view along representative Li-ion rows. (B) Relative position of the chains in the polymeric electrolyte; white ball, arsenic; magenta, fluorine; green, carbon; red, oxygen. (C) Representative diffusion of the Li-ion in PEO₆:LiPF₆. In the diagram, the solid blue ball represents Li-ion and the meshed blue ball represents Li-ion in the intermediate state in 4 coordinate sites. Adopted with permission from [52]. Copyright 2003, American Chemical Society.

the help of the segmental motion in the polymeric chains [46,52,53]. The ion transportation mechanism in polymeric materials is very complex because the material nature also depends on certain factors including polymer type, temperature effects, polymeric structure, the concentration of ion-based salts in the polymer, and molecular weight. It can be concluded that ion migration in the polymer phase is still unclear and needs to be continued research.

Evaluation of ion conduction

The ionic conductivity of the inorganic solid electrolyte associated with the ion hopping mechanism can be calculated by the VTF and Arrhenius equation. The conductivity can be articulated as the sum of all moving charge species (i), and ionic conductivity can be calculated by

$$\sigma = \sum_i q_i c_i u_i = \sigma_0 \exp(-E_a / kT) \quad (2)$$

where c_i , q_i , and u_i are the charge concentration, charge number, and mobility of the charge, respectively. σ_0 is a pre-exponential factor and is also associated with the number of charges, E_a denotes the activation energy of mobile ions, T is the absolute temperature, and k is the Boltzmann constant. The activation energy is calculated by nonlinear least-squares fitting. The value of E_a is obtained from the plot of $\log \sigma$ versus $1/T$ [54]. The solid electrolytes follow the linear Arrhenius variations in which ion migration happens by a hopping mechanism.

The ion migration in the SPEs relates to inter- and intra-chain hopping, which is associated with the transfer of polymeric chain segments with coordinated sites. Despite some disagreements, the VTF model is comparatively widely accepted for describing the ionic conduction behavior in SPEs.

$$\sigma = \sigma_0 T^{1/2} \exp(-B / k_B T - T_0) \quad (3)$$

In the above equation, B is called pseudo-activation energy, which is explained by the unit of E_a/T and T_0 , also known as the reference temperature, and k_B is the Boltzmann constant. VTF behaviors are commonly pragmatic in SPE above the glass transition temperature of the polymeric matrix.

Computational Approaches for Ion Migration Mechanism

The Li-ion migration requires addressing the various time scales, length scales, and ion migrations depending on the ion aggregation and changes in solvation architectures. The computational method is deemed the best way to describe these interactions and ion migration mechanisms.

Nudged elastic band method

NEB is an effective approach for discovering the minimum energy path (MEP) between the initial and final positions. A NEB simulation takes the input, the initial and final position of the mobile ion/vacancy, an initial supposition of migrating channels, and determines energy values along the ionic pathway [55]. NEB is widely applied to determine the transition rates via harmonic transition state theory approximation [56]. The transition state's energy between the initial and final position is also known as activation energy (E_a). The crystal structure of solid electrolytes may display several ion transport

channels that link the same or different ion positions and follow various energy barriers.

Zeier et al. [58] also explained the vacancy-mediated diffusion and interstitially medicated diffusion mechanism of the Li-ion of the $\text{Li}_4\text{P}_2\text{S}_6$ solid electrolytes. Two nonequivalent Li-ion vacancies are achieved by removing Li-ion from the Wyckoff position (Li2) or (Li1), in which the Li2 vacancy in the ground state at ~ 0.38 eV is below a vacancy on the Li1 site. In in-plane lithium-ion migration, 2 vacancy jumps are plausible, for example, from Li2 to Li2 and Li1 to Li1, as shown in Fig. 4A. The ion migration in the z plane comprises the Li2-Li1-Li2 pattern. Notably, the vacancy transition from Li2 to Li2 is completed by a minor activation barrier (0.2 eV). The Li2 to Li1 and Li1 to Li1 transition is explained, but Li1 has a high-energy ground state and a higher activation barrier for ion migration. Consequently, the vacancy-associated diffusion between Li2 to Li2 would be the dominant ion migration mechanism due to the small value of E_a and is anticipated to be the main Li-ion diffusion channel. There are 3 interstitial sites that are positioned between the sheets of $\text{P}_2\text{S}_6^{4-}$, i.e., the Wyckoff position $6k$ ($x, 0, z$), labeled *int1*, the second one within the sheets of $\text{P}_2\text{S}_6^{4-}$, i.e., Wyckoff position $6k$, and labeled *int2*, and the third one is between sheets of $\text{P}_2\text{S}_6^{4-}$ along the P-P axis, i.e., Wyckoff position $1b$ ($0, 0, 1/2$), named *int3*. The 2 interstitial sites are between sheets of $\text{P}_2\text{S}_6^{4-}$, and the third is within the $\text{P}_2\text{S}_6^{4-}$ polyhedral sheets. *int3* is a more stable site, and the relative stability of the other 2 sites are *int3* (+0.37 eV) and *int1* (+0.04 eV). In the x - y plane, diffusion channels for the lithium-ion comprised 2 stable interstitial defects such as *int1* and *int3*, as shown in Fig. 4B. The migration from *int3* and *int1* led to a minor energy barrier (0.05 eV), but migration to another *int1* requires an energy barrier (0.51 eV). However, the Li-ion migration in an *int3-int1-int1-int3* manner reveals the ideal distance of 2 Å for the hopping mechanism at the x - y plane. The ion-diffusion mechanism along the z plane also comprises 3 sites (interstitial) and follows the *int3-int1-int2-int2* path. The energy barrier between *int3-int1* is low, but *int1-int2* has a high energy barrier (0.5 eV). This jump is followed by high activation barrier, and the positioning of Li-ion at *int2* is energetically unfavorable [57]. In this scenario, unfavorable jump into *int2*, the low activation energy for reverse jump will follow the higher rate of backward ion migration. As a result, the activation energy barrier for ion migration along the z plane makes ion diffusion less likely than in the x - y plane [58].

The NEB calculation is also applied to determine energy barriers for various defects such as interstitials and lithium vacancy in different solid electrolyte systems such as Li_3PO_4 [59,60]. The lithium-ion is also removed from the Li_3PO_4 crystal system, and many neighboring lithium ions can hop into the vacant site and contribute to a 3D ion diffusion. Different possible diffusion channels are considered along with lattice directions. The vacancy mediated migration involves zigzag diffusion such as the $1(d) \leftrightarrow 2(c) \leftrightarrow 3(d)$ path along the a axis. The NEB outcomes for this path presented a smaller activation energy barrier for the first step, and an energy barrier is 0.69 eV for the entire mechanism in Fig. 4C. Along the b axis, the ion migration can continue along the axis direction with a hop between the lowest energy of adjacent sites. In the crystal structure, the distance between the 1 and 4 sites is slightly lower than that between the 4 and 5 sites; thus, the diffusion energy barrier (0.67 eV) is also slightly lower for the shorter path in Fig. 4D. For the vacancy-assisted migration along the c axis, the 2

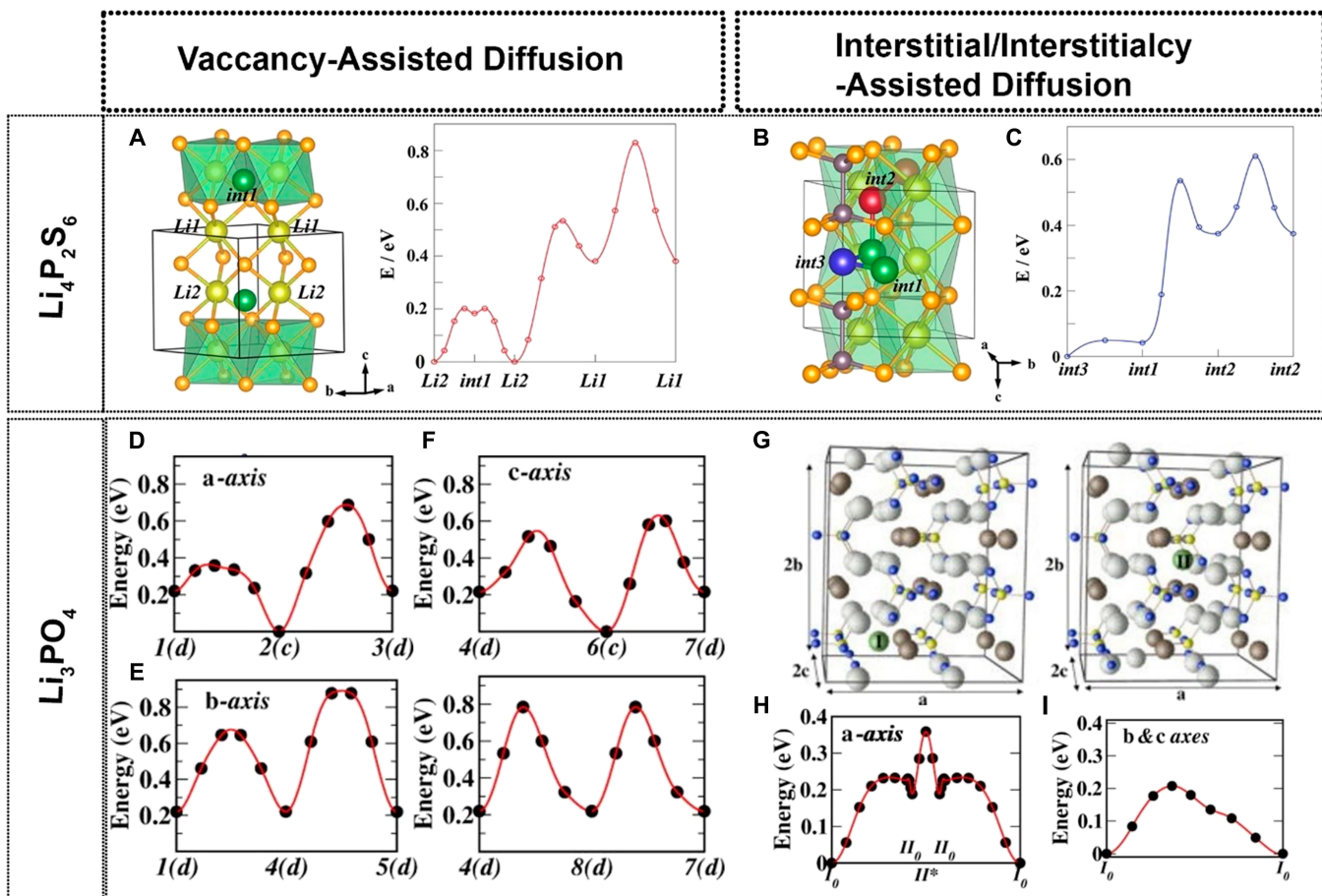


Fig. 4. (A) Structural illustration for the vacancy-assisted diffusion mechanism between the crystal lattice of the lithium sites along the x-y direction (Li1 to Li1 and Li2 to Li2) and z plane (from Li1 to Li2). (B) NEB calculated energy barrier for the vacancy-assisted mechanism representing a small activation barrier for Li2 to Li2 between the sheets of $\text{P}_2\text{S}_6^{4-}$ in the plane. Li1 to Li1 is energetically impossible, as it comprises a diffusion within the $\text{P}_2\text{S}_6^{4-}$ sheets. The z plane stops the long-range jump in $\text{Li}_4\text{P}_2\text{S}_6$ due to the high activation barrier. Along the z axis, the diffusion path comprises 3 favorable interstitial sites. (C) The jump between int1 and int3 is, actively foremost, a large activation energy barrier in the migration via int2 between the sheets of $\text{P}_2\text{S}_6^{4-}$ if lithium is located in int2. Adopted with permission from [58]. Copyright 2016, American Chemical Society. (D) Energy path of the a axis for vacancy-assisted mechanism along with configuration coordinate. (E) Energy path of the b axis for vacancy-assisted mechanism. (F) Energy path of the c axis for vacancy-assisted mechanism representing the 2 possible migration paths. (G) Interstitial configuration of Li_3PO_4 along the b axis. (H) Energy path for the interstitial-assisted diffusion along the a axis between the I and II sites via direct hop and interstitialcy steps. (I) Energy path for the interstitial-assisted diffusion along the b and c axes between neighbored I_0 sites via interstitialcy steps. Reprinted with permission from [59]. Copyright 2007, IOP Publishing.

possible migration paths are highlighted in Fig. 4E. The smaller migration barrier is found for the $4(d) \leftrightarrow 8(d) \leftrightarrow 7(d)$ path, which comprises 2 equivalent portions with a total energy barrier of 0.56 eV. The Li_3PO_4 crystal structure revealed 2 kinds of void paths along the c and b axes. There are 2 metastable interstitial sites along the c and b axes, as shown in Fig. 5F, respectively, labeled I and II. In the interstitialcy mechanism, the interstitial lithium-ion at I_0 sites is kicked out and exchanged with nearby d-type lithium of the host crystal lattice, although the kicked-out lithium-ion occupies similar interstitial I_0 sites. The NEB outcomes represented the migration energy barrier for the interstitialcy step, which is 0.21 eV in Fig. 4I. Along the b and c axes, the diffusion of the interstitial ion is also defined as a series of zigzag steps. This proposed interstitialcy mechanism is more energetic and effective than other interstitial diffusion-based mechanisms. We have considered the direct hopping between I_0 sites and adjacent I_0 or I_1 sites. The diffusion mechanism along the a axis involves types I and II of void path in Fig. 4H. The diffusion comprises 3 steps: (a) $I_0 \leftrightarrow II_0$, (b) $II_0 \leftrightarrow II^* \leftrightarrow II_0$, and (c) $II_0 \leftrightarrow I_0$. For the diffusion step, (a) and

(b) have an energy barrier of 0.23 eV and 0.17 V, respectively [59]. The computational study of the interstitialcy mechanism for ion diffusion calculated their migration energy barrier of $E_a = 0.21$ eV for the b and c axes and $E_a = 0.35$ eV for the a axis, which are considerably lower than experimental values [61–63] and lower than the vacancy-based mechanism energy barrier as well. The NEB method is an efficient approach for finding advanced battery materials such as Li_4SnS_4 and Li_4SnSe_4 [64], Li_3AsS_4 , alloyed with Li_4GeS_4 [65], and Li_2CuPS_4 [66].

MD simulation

The MD computation is based on the dynamics of the mobile ions, in particular, materials with complete atomistic aspects. The MD computation offers ion migration information on the time span of femtoseconds to nanoseconds. The modern MD simulation can be classified into classical MD simulation (interatomic potentials known as force fields) applied for calculating the atomistic forces, as well as AIMD applied for the calculation of the interatomic interactions. The AIMD computation has been very popular since it can be applied to all materials with

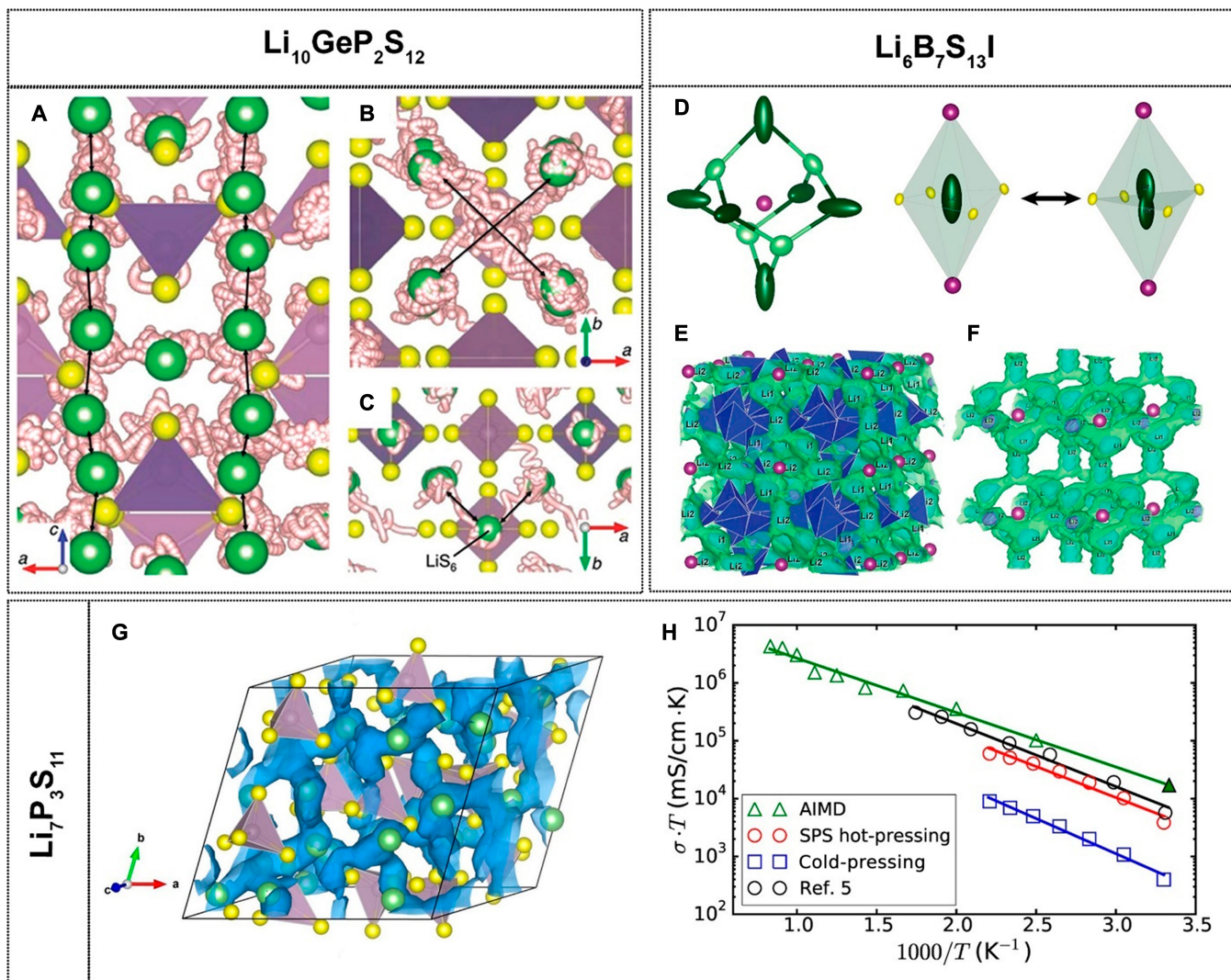


Fig. 5. (A) Li-ion trajectories and diffusion pathway in the ab plane. (B and C) PS_4/GeS_4 (green), sulfur (yellow), and initial position of the nondiffusing atom and all lithium sites. Adopted with permission from [68]. Copyright 2012, American Chemical Society. (D) Li-ion forms a cage around the I^- and LiS_4I_2 octahedron in the structure of $\text{Li}_6\text{B}_7\text{S}_{13}\text{I}$ along with anisotropic displacement of the Li^+ site as well as their split-site illustration. (E and F) Lithium-ion probability density distribution in the $\text{Li}_6\text{B}_7\text{S}_{13}\text{I}$ structure and corresponding lithium cages around the I atom. Adopted with permission from [69]. Copyright 2021, American Chemical Society. (G) Probability density distribution of Li^+ in the $\text{Li}_7\text{P}_3\text{S}_{11}$ solid electrolyte. (H) Arrhenius plots of the $\text{Li}_7\text{P}_3\text{S}_{11}$ solid electrolyte from AIMD simulation and ionic conductivities of the cold-pressed $\text{Li}_7\text{P}_3\text{S}_{11}$ solid electrolyte and the SPS hot-pressed $\text{Li}_7\text{P}_3\text{S}_{11}$ solid electrolyte. Adopted with permission from [70]. Copyright 2016, American Chemical Society.

complex chemistry. In contrast to NEB computation that relied on assumptions of ion migration paths as input, MD computation offered a visual representation of ion trajectory and dynamics. The findings are very useful in observing the diffusion of ions. Figure 5A shows the lithium-ion diffusion in a 1D diffusion path along the c axis in LGPS. The significant lithium hopping is carried out in the ab plane. The diffusion channels in this study are similar to the findings of Kamaya et al. [67]. A new diffusion path connecting one LiS_4 (tetrahedral) link to another PS_4 along the ab plane is shown in Fig. 5B. The ion diffusion along the ab plane is not surprising because there is a void space between the PS_4 tetrahedra and the $(\text{Ge}_{0.5}\text{P}_{0.5})\text{S}_4$ tetrahedra. The additional migration path connects the lithium atoms in the LiS_6 (octahedra) site along the c -axis migration channel in Fig. 5C [68]. The structure of $\text{Li}_6\text{B}_7\text{S}_{13}\text{I}$ facilitates the Li-ion migration, which is determined via AIMD simulation. The 3D migration pathway in the structure displays considerable lithium-ion mobility along $\text{Li}1\text{--Li}2\text{--Li}1$ channels in Fig. 5D

to F. $\text{Li}2$ site reveals a very anisotropic probability density. The lithium ions in the $\text{Li}_6\text{B}_7\text{S}_{13}\text{I}$ structure migrate in a localized trajectory that develops a cage around the I site (center of 8 octants), in which long-range ion migration between the cages is allowed by the links between the fully and partially and highly anisotropic $\text{Li}2$ site in Fig. 5D [69]. In the $\text{Li}_7\text{P}_3\text{S}_{11}$ solid electrolyte, the 3D networks of the ion diffusion, all Li^+ sites are well connected via S_4 tetrahedra [70] in Fig. 5G. These lithium sites are fully occupied in the structure, and the ionic motion is vastly collective, which agrees with other computational and experimental studies in Fig. 5H. The AIMD simulations have also been helpful in order to propose new solid electrolytes such as $\text{Li}_{10-x}\text{SnP}_2\text{S}_{12-x}\text{Cl}_x$ [71], Li_2OHCl [72], and $\text{Li}_2\text{Sc}_{2/3}\text{Cl}_4$ [73]. The AIMD computation has been demonstrated to be quite precise for predicting other characteristics of solid electrolytes such as electrochemical stability [74,75], phase stability [76,77], and activation energy [70,78]. Meanwhile, MD computation yields comprehensive information on the

structure with limitations, such as the size of the simulated system and time scale.

BV model

In the BV model, the relationship between the empirical bond length (R) and BV offers the connection between the structure and ion migration in the solid electrolytes. The BV-based force field has investigated a range of solid electrolytes for high-performance ASSBs. The BV site energy (BVSE) approach is applied to evaluate the ion diffusion path and calculate migration energy barrier height. The rule is that atomic valence should be similar to the sum of BV around the atom, and the migration paths that belong to available sites for mobile ions can be attained. The Morse potential energy and the Coulombic repulsion potential of the ions as well as the migration barrier are permitted to be calculated by the BVSE methods and evaluated. The equations can calculate the Morse potential and Coulombic potential:

$$E(\text{Li})_{\text{Morse}} = D_0 \left\{ \left(\exp \left[\alpha (R_{\min} - R) \right] - 1 \right)^2 - 1 \right\} \quad (5)$$

$$E(\text{Li}-A)_{\text{Coulombic}} = q_{\text{Li}} q_A / R_{\text{Li}-A} \operatorname{erfc} \left(R_{\text{Li}-A} / \rho_{\text{Li}-A} \right) \quad (6)$$

In the above equations, D_0 , α , and R_{\min} are the Morse potential parameters that can be calculated from a large amount of stable materials; R and q correspond to the bond distance between the 2 atoms and the effective charge of the atom, respectively [79].

Adams et al. [80] identified the ion diffusion path and found the structure–property relationship for lithium silicate (Li_2SiO_3). The BV energy model of the 1D Li-ion transport pathway in Li_2SiO_3 is shown in Fig. 6A to D. The projected activation barrier is 1.15 eV for Li-ion (vacancy) diffusion along the zigzag pathways and is also compared to the experimental values of 1.0 eV [80]. Mazza et al. [81] applied the BVS approach, which permitted sketching to a time-averaged path followed by the Li-ion motion in the $\text{La}_{2/3-x}\text{La}_{3x}\text{TiO}_3$ (LLTO) structure. From the simulation, the ionic conductivity could be proposed based on these statements in the LLTO structure. (a) The Li-ion and vacancies are homogeneously distributed over the La2/La1 sites. (b) All the Li-ions are at L2 sites. (c) The La2 site is entirely occupied by Li and La. It has been explained that the third statement disagrees with experimental data. At the same time, the first statement is the distribution of the vacancies and lithium ions in an equal amount over the La2 and La1 sites, exhibiting a high ionic conductivity that is comparable to the experimental conductivity. The second statement also contributes to the Li-ion conduction in LLTO. Brese and O’Keeffe [82] evaluated the bottleneck size using the BV and BVS approach. Inaguma et al. [83] evaluated the bottleneck for the $\text{Li}_{0.55}\text{Li}_{0.35}\text{TiO}_3$ solid electrolyte. The possible migration path is carried along the ab plane of La2. In the ab plane of $\text{Li}_{0.55}\text{Li}_{0.35}\text{TiO}_3$, BVS at the 2d site is bigger than at the 2c site, but the 2d and 2c sites in $\text{La}_{0.62}\text{Li}_{0.16}\text{TiO}_3$ are almost equal. The diffusion via bottleneck at the 2d sites in $\text{Li}_{0.55}\text{Li}_{0.35}\text{TiO}_3$ is illustrated using the dotted line in Fig. 6E and F. The BV simulation, along with the Rietveld refinement of the XRD (x-ray diffraction) data, explained the tetrahedrally connected 24d site Li(1) and Li(2) sites, which are the low-energy sites for lithium in the cubic phase of the LLZO. A 3D path of low activation energy for the Li-ion diffusion in the LLZO involves both sites in the following pathway networks

Li(1)-Li(2)-Li(2)-Li(1), which are interconnected at the Li(1) site (Fig. 6G to I) [84].

A comparative study between the pro-crystal calculation and ΔE_{BVSE} (BVSE results) for Li_4GeS_4 is discussed. Both models proposed the most accessible pathway to move along the b direction, including the 2 kinds of lithium sites, and the third lithium site is isolated. Mapping a higher iso-value allows a migration within the bc plane. However, a higher energy density iso-value is needed to attain 3D ion transportation in Fig. 7A to F [85]. Xiao et al. explored the effects of the ZnO aliovalent substitution on the Li_3PS_4 solid electrolyte using the BV analysis and DFT calculation. This study investigates the atomic configurations and Li-ion diffusion channels of the doped $\text{Li}_{3+3x}\text{P}_{1-x}\text{Zn}_x\text{S}_{4-x}\text{O}_x$ models with $x = 0.0625$ and $x = 0.021$. The migration pathway of the Li-ions is represented by the iso-surface of the potential energies in Fig. 7G to J. After the doping of ZnO, the continuous diffusion pathway is still in the bc plane, indicating the 2D diffusion of Li^+ like pristine Li_3PS_4 . When the Zn dopant is substituting the P sites, the Li-ion pathways disappear around the Zn and would hinder the Li-ion migration around itself. With the addition of the O dopant, the Li-ion diffusion channels around the O dopant are enlarged for both compositions. The Zn–S bond is larger than the P–O bond and decreases the free space for the Li-ion diffusion. With $x = 0.021$, the O dopant prefers appearing in the adjacent Zn and broadening the migration channels for Li-ion around the Zn. In comparison, $x = 0.0625$, the O dopant would be located away from the Zn, which hindered the Li-ion motion around the Zn atom. A small amount of O doping improves Li-ion diffusion in Li_3PS_4 ; small P–O bonds and small O dopant would reduce the volume of the Li_3PO_4 unit cell, which does not facilitate the Li-ion migration. Nevertheless, it is found that the long Zn–S bond forms in $\text{Li}_{3.06}\text{P}_{0.98}\text{Zn}_{0.02}\text{S}_{3.98}\text{O}_{0.02}$ ($x = 0.02$) and O dopants are next to the Zn dopant. The large-sized ZnS_4 tetrahedron structure might also counterbalance the PS_3O unit and minimize the reduction of unit cell volume. The activation energy for $x = 0.021$ is -0.5 meV/atom, while that for $x = 0.021$ is 1.15 meV/atom. In summary, the activation energy of $x = 0.02$ is lower than other materials with doping contents, which has been proved through experiments [86].

Density functional theory

DFT is a modern computational addition to quantum chemistry. In the DFT approach, the system of interacting electrons is mapped onto an effective noninteracting system with the same density. The DFT + U method is an extended functional approach for self-interacting electron correlation. DFT+ U also denotes the approach itself without explicit reference to GGA or LDA or (GGA + U or LDA + U). Within the generalized gradient approximation (GGA), DFT is also carried out to evaluate the change in electronic conductivity after doping and replacing the lithium atom in the system. Currently, the evaluation of the conductor material phase stability using the first-principles calculation has been assisted by the databases of thermodynamic materials such as Open Quantum Materials Database (OQMD), Materials Projects (MP), and automatic flow (AFLW). A thermodynamics convex hull is designed for a chosen material system by comparing the energies of all the samples in the composition space. Convex hull can be used to quantify the phase stability of materials [29]. Potential materials as solid electrolytes have been predicted, designed, and discovered using these computational approaches represented in Table 1.

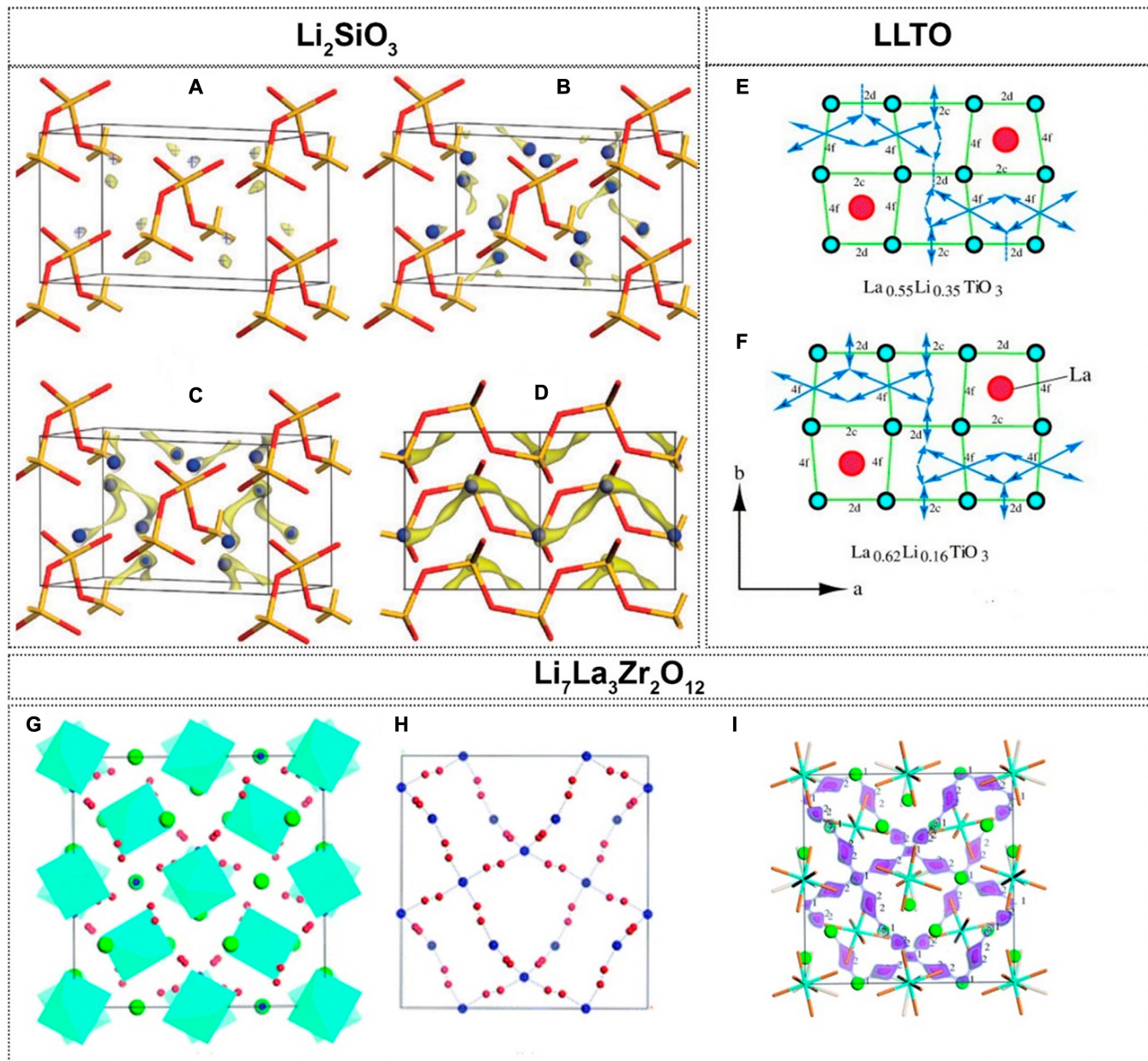


Fig. 6. The BV energy model of the 1D Li-ion transport pathway in Li_2SiO_3 and Li-ion reaches different energy thresholds. (A) Total site energy $E_{\text{pot}}(\text{Li}) = 0.5 \text{ eV}$ Li-ion migration pathway in Li_2SiO_3 is restricted to the equilibrium site. (B) An 0.8-eV local hope to vacant interstitial sites. (C and D) Total site energy $E_{\text{pot}}(\text{Li}) = 1.15 \text{ eV}$. A 1D path is formed. Reproduced with permission from [80]. Copyright 2009, Royal Society of Chemistry. (E) Schematic of Li-ion diffusion pathway in the ab plane for $\text{La}_{0.55}\text{Li}_{0.35}\text{TiO}_3$. (F) Representation of diffusion pathway for Li-ion in the ab plane for $\text{La}_{0.62}\text{Li}_{0.16}\text{TiO}_3$. Reprinted with permission from [83]. Copyright 2006, Elsevier. (G) Projection of the unit cell of cubic LLZO. (H) Network of the Li sites. (I) BV model of Li-ion diffusion pathway presented as 3 iso-surfaces of low lithium site energy. Li(1) on 96h sites: red spheres (A and B); Li(2) on the 24d sites: blue ball; La (green ball), ZrO_6 (blue octahedra). Reproduced with permission from [84]. Copyright 2012, Royal Society of Chemistry.

Computational contribution toward the rational design of solid electrolytes

Li-ion conductors have mainly been discovered by extending known super Li-ion conductor materials into new compositional candidates. Over the past 2 decades, advances in simulation and theoretical methods have enabled the accurate evaluation of material properties. In light of this, high-throughput theoretical screening of materials to a high-throughput combination of material properties has become a promising approach to discovering new Li-ion conductors. The high-throughput theoretical screening approach was applied to material catalogs to discover new superionic candidates. Several key attributes of

the electrolyte materials offer higher Li^+ conductivity, wide electrochemical windows, and chemical stability. As shown in Fig. 8, different calculation approaches with different accuracies and bases can be applied to evaluate different properties of solid electrolytes. In this review, we mainly focus on Li-ion migration, activation energy, and the mechanism of ion transportation within the solid electrolytes. The chemical and structural stability are also important properties of solid electrolytes. The thermodynamic data can be used for the preliminary estimation of decomposition and phase transitions during the stability assessment of materials. Electrochemical windows of solid electrolytes indicate voltage ranges in which the materials are

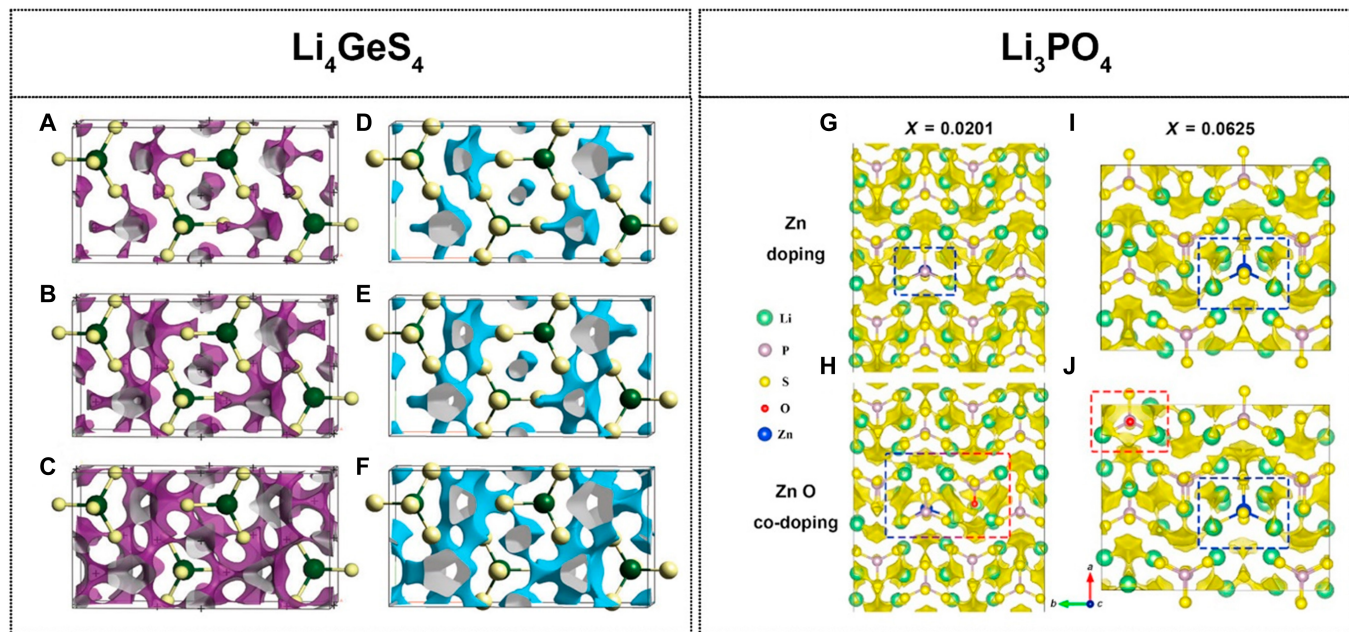


Fig. 7. A comparative study between the pro-crystal and BV analysis for Li-ion diffusion in Li_4GeS_4 in the ab plane. (A to C) ΔE_{BVSE} of 1.0, 1.35, and 1.9 eV, respectively, and (D to F) q_{pro} of 0.0016, 0.0018, and 0.0024 a.u., (atomic unit) respectively. Reproduced with permission from [85]. Copyright 2013, John Wiley and Sons. The Li-ion diffusion pathway is simulated by BV analysis for the Li_3PS_4 electrolytes that is doped with the different concentrations of ZnO . (G and H) $x = 0.021$. (I and J) $x = 0.0625$. The space highlighted in yellow indicates the Li-ion migration pathway, and local pathways around the O and Zn dopants are indicated by the red and blue dashed line boxes, respectively. Reprinted with permission from [86]. Copyright 2019, Elsevier.

stable. Shi et al. [87,88] created a database of the calculated transport properties of the Li-, Na-, K-, Ag-, Cu-, Mg-, Zn-, Ca-, Al-, O-, and F-containing inorganic compounds. This database accelerates the screening of superionic ionic conductors and accumulates descriptors for machine learning (ML), providing a basis for large-scale research on ion migration in inorganic materials [87,88]. A DFT electronic structure calculation reveals that the window width is closely related to the band gap of the solid electrolyte [89]. Fujimura et al. [31] calculated the first-principles MD simulation on the LISICON solid electrolytes in order to optimize the Li-ion conductivity in the modal structures. Generally, this accelerated strategy can also be applied to other systems with more complex chemical structures and chemistries.

Ion Conduction in Various Classes of Solid Electrolytes

Crystalline solid electrolytes consist of coordination polyhedra and a 3D arrangement of mobile species. The coordinated polyhedron designs a conductive network that contains vacancies and interstitials distributed throughout the framework. The amorphous glassy type of solid electrolyte does not have the long-range ordered structure as a crystal structure. Still, it possesses a short-range ordered structure, which contributes to the ionic conductivity in a highly expressive manner. In glassy electrolytes, the ions are transported through the ordered lattices. The ions at the local position are first excited to nearby sites and then migrate collectively at a macroscopic level. An important role is played by structural frameworks and mobile ions when defects exist in the amorphous/glassy electrolytes. Solid electrolytes can be mainly categorized into oxide- and sulfide-based solid electrolytes.

Oxide-based solid electrolyte

Research on oxide electrolytes has recently become more active due to their proximity to natural compounds, and the investigation of this kind of electrolytes is initiated among oxide [84] due to easy handling [90]. Although sulfide-based electrolytes are sensitive and chemically unstable against a moist atmosphere, different oxysalts and $\gamma\text{-Li}_3\text{PO}_4$ -type systems with considerable ionic conductivity were investigated in the 1970s [91]. A comprehensive study on $\gamma\text{-Li}_3\text{PO}_4$ shows a specific relationship between crystal lattice and ionic conductivity. Conversely, the ionic conductivity of materials is enhanced by increasing the lattice volume and broadening the migration channel for the mobile ions [92]. The highest value of the ionic conductivity of oxides is $\sim 10^{-6}$ to 10^{-4} S cm $^{-1}$. However, the major downside of all oxide-based solid electrolytes is high grain boundary resistance, which has not been eliminated.

Lithium phosphorus oxynitride

The lithium phosphorus oxynitride (LiPON) solid electrolyte is a mixture of the high lithium contents and nitrogen in the structure with amorphous nature. LiPON exhibited a good electrochemical stability window (up to 5 V) against Li/Li $^{+}$ [93]. Some double bond bridging N (N_d) and apex substituted N (N_a) are highlighted in the structure of LiPON. No triple bond bridging N (N_t) is detected in the amorphous structure of LiPON in Fig. 9A. The creation of the double bond bridges is realized by reducing the lithium contents, leading to an improved ionic conductivity. Two mechanisms are explained: (a) the increase in structure density, destabilizing the lithium sites via enlarged short-range Li-Li interactions, and (b) the enhancement of N covalency. Compared with N_a /phosphate O, the lithium atom anchored near N_d is shorter, meaning that the saturated valence state of N_d involved in the covalent bonds

Table 1. A detailed comparison of computational-based approaches toward exploration of the solid electrolytes.

NEB	MD	BV	DFT
Output Quantify diffusion energy profile Energy barrier Vacancy/interstitial mechanism	Output Ion hopping Ion diffusion without a pre-assigned diffusion path Calculate the diffusion pathway for the disorder system Conductivity Diffusion coefficient at different temperature Time-dependent ion position Mechanistic information	Output Ion transport pathway as a region of low bond valence 3D bond valence map Estimate the activation energy Determination of lithium occupancies of complex disordered compounds Pathway geometry Approximate energy threshold	Output Energy above the hull E_{hull} Or the energy convex hull Phase stability Phase equilibria Voltage profile Solubility limits Band gap Input Energy values of the materials Modeling program Thermodynamics data
Input Diffusion pathway Vacancy Interstitial Mobile carrier Assigned diffusion path	Input Physical time scale (100 ps to 1 ns) Compositional cost Small size unit cell (few hundred atoms)	Input Bond valence parameters Unit cell volume Crystal structure	Input Metastability, as evaluated using E_{hull} , may not be sufficient to determine the synthesizability of a conductor
Limitations Not calculate the diffusion pathway and carrier for disorder system	Limitations Interatomic potential Large unit cells Vacancy/interstitial mechanism	Limitations Overestimation of a migration barrier The paddle-wheel mechanism makes it difficult to validate	

**Fig. 8.** Using a computation-driven approach, the general schematic representation of the steps to explore the new superionic conductors.

with P reduces its electrostatic interactions with Li-ions. This process can stimulate the movement of nearby Li-ions. The optimal balance between N_d contents and Li is attained for the $\text{Li}_{2.94}\text{PO}_{3.50}\text{N}_{0.31}$ structure, which is denoted as a “Li-deficient” configuration supporting phosphate condensation by the apex-substituted N bridges and keeps a comparatively high Li

concentration [94]. Despite its benefits such as compatibility with lithium metal anode and composite cathode, and exhibited the ionic conductivity of $2.3 \times 10^{-6} \text{ S cm}^{-1}$ at room temperature (RT) [95,96]. The major drawback of the LiPON solid electrolyte is the prerequisite of the special apparatus, such as the sputtering process.

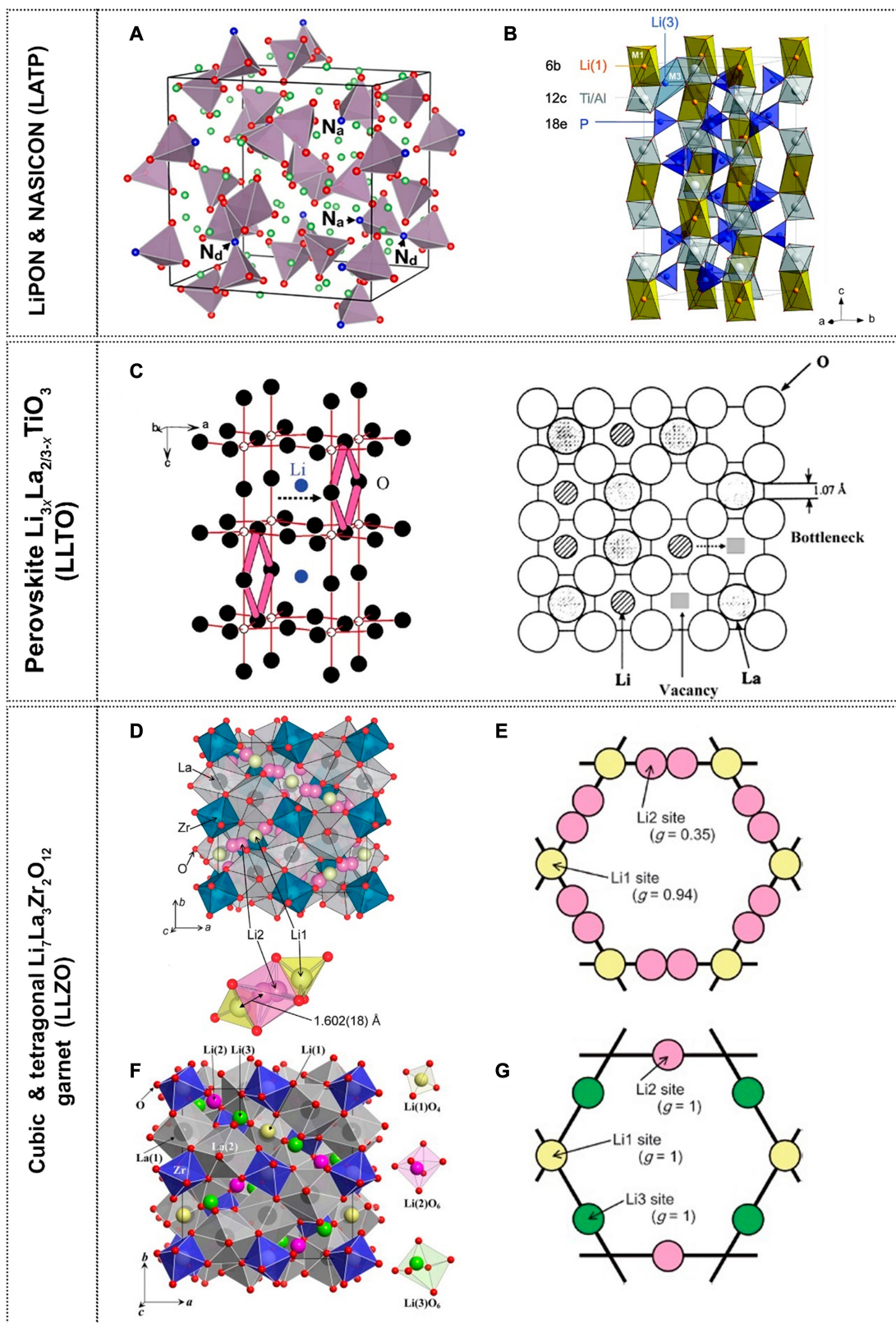


Fig. 9. (A) The crystal structure of $\text{Li}_{2.94}\text{PO}_{3.50}\text{N}_{0.31}$ was achieved by AIMD simulation. Li, P, N, and O are represented by green, gray, blue, and red balls, respectively. Adopted with permission from [94]. Copyright 2018, American Chemical Society. (B) Structure of LATP electrolyte with rhombohedral lattice. The primary M1 site occupied by Li is represented by an orange ball (polyhedra); the Li ions also occupy the M3 sites to a very lesser extent. Reproduced from [97] with permission from the Royal Society of Chemistry. (C) Schematic diagram of the 3D model of the Li-ion migration along the ab and c planes in the $\text{La}_{3-x}\text{La}_{2/3-x}\text{TiO}_3$ (LLTO) crystal structure. Reproduced with permission from [103]. Copyright 2021, Springer Nature. (D) Cubic structure of the garnet LLZO and the position of Li1 and Li2 sites. (E) Loop structure of the lithium arrangement in cubic-LLZO. Adopted with permission from [113]. The Chemical Society of Japan. (F) Tetragonal-LLZO structure. Reproduced with permission from [193]. Elsevier. (G) Loop structure of the lithium arrangement in tetragonal-LLZO. Adopted with permission from [113]. The Chemical Society of Japan.

NASICON

NASICON is an oxide-based solid electrolyte with a 3D skeleton conductive framework. The highest ionic conductivity of NASICON can reach $\sim 10^{-3}$ S cm $^{-1}$. A general formula of NASICON electrolytes is $\text{LiM}_2(\text{PO}_4)_3$, in which Ti, Ge, and Zr occupy the M sites. The conductive framework of NASICON electrolyte consists of corner-sharing PO_4 tetrahedra and MO_6 octahedra constructed to form a 3D network. Mobile ions, i.e., Na^+ , occupy the interstitial sites and diffuse along the c axis. This NASICON-type electrolyte can keep its structure and turn into a lithium-based solid electrolyte when sodium is replaced by lithium. The Li ions occupy most of the M1 positions and minor part of M3 sites. Another study found that in $\text{Li}_{1.5}\text{Al}_{0.5}\text{Ti}_{1.5}(\text{PO}_4)_3$, beside the M1 sites, the lithium ions occupy site closer to M2 and then displace toward b , herein represented as M2'. The substitution of the Ti^{4+} via Al^{3+} ions needs extra Li^+ for charge compensation, and ions occupy the interstitial voids in Fig. 9B [97]. The Li^+ dynamics are affected by this enrichment in charge carriers. A recent investigation of the chemical stability of the superionic sodium conductor (NASICON) $\text{Li}_{1+x}\text{Ti}_{2-x}\text{Al}_x(\text{PO}_4)_3$ electrolyte under humid conditions revealed its good chemical stability. When Li^+ is inserted in the NASICON solid electrolyte because of the weakening of the crystal's bond, the crystal's volume expands, resulting in cracks produced in the materials [98].

Perovskite ABO_3

Perovskite ABO_3 (A = Ca, Sr, La, and B = Ti, Al) is an oxide electrolyte that is first published by Takahashi and Iwahara [99]. Lithium might be added to the conductive framework at the A sites, resulting in the general formula $\text{La}_{3x}\text{La}_{2/3-x}\text{TiO}_3$. It is a cubic geometry in which Ti octahedral coordinates with the O atoms [100]. The ionic conductivity of $\text{La}_{3x}\text{La}_{2/3-x}\text{TiO}_3$ (LLTO) highly depends on the vacancy concentration and lithium content. The Li^+ migration channels allow the lithium ions to diffuse between vacancies via octahedral networks. The lithium-ions diffuse via 2 migration pathways in the LLTO crystal structure: one along the ab plane and another along the c axis. Despite this, the bottleneck size for the c axis is smaller than for the ab plane. As a result, Li^+ ions predominantly diffuse along the ab plane Fig. 9C. Increasing the temperature causes a larger c -axis bottleneck, and Li-ions can diffuse along the c axis [101–104]. The bottleneck size and lattice volume can be optimized by doping rare-earth metal (M = Sm, Pr, Nd, and La) at the A-site. The ionic conductivity of perovskite is highly related with Li and vacancy concentration and their interactions [105]. The $\text{Li}_{0.34}\text{La}_{0.56}\text{TiO}_3$ -type perovskite exhibits a lithium-ion conductivity of $\sim 10^{-3}$ S cm $^{-1}$ [102].

Garnet LLZO

Oxide-based garnet electrolyte $\text{Li}_5\text{La}_3\text{M}_2\text{O}_{12}$ (M = Ta, Nb) was revealed in 2003, and a recent lithium-rich garnet (LLZO) solid electrolyte was synthesized in 2007 and also considered to be an incredible chemical stable against Li metal as well as exhibits good Li-ion conductivity [106,107]. The $\text{B}_3\text{C}_2\text{O}_{12}$ framework comprises B cations at dodecahydrate sites and C cations at the octahedral positions in the typical structure of garnet $\text{A}_3\text{B}_3\text{C}_2\text{O}_{12}$. Several cations can be introduced into the garnet structure, resulting in additional Li^+ sites and high Li-ion conductivity [108–111]. Major structural units are the ZrO_6 octahedra (6-fold coordinated) and the LaO_8 dodecahedra (8-fold coordinated). Two phases exist in the garnet-based electrolytes,

i.e., the tetragonal phase (LaO_8 dodecahedra 8b, 16e, and one ZrO_6 octahedra 16c) and the cubic phase (LaO_8 dodecahedra 24c and ZrO_6 octahedra 16a). The most significant difference is the Li^+ position in the garnet structure, where 2 Li^+ ions occupied positions in the cubic phase of garnet (96 h Li_2 -octahedral gap and 24d Li_1 -tetrahedral void) and 3 Li^+ -ions occupied sites in the tetragonal phase (16 f Li_2 -octahedral gap, 32 g Li_3 -octahedral gap, and 8a Li_1 -tetrahedral void) [112]. The vacancies and lithium sites in tetragonal-LLZO are configured, enabling uncooperative ion migration among the connected positions. Because of the occupancy of lithium atoms and available sites, the ion migration is better in cubic-LLZO than in tetragonal-LLZO. The Li^+ migration loop is adjacent to the tetrahedrons in Fig. 9D to G. The Li^+ migration loop is adjacent to the tetrahedrons. For the cubic garnet, Li_1 and Li_2 are positioned alternately. The lithium-ion occupies at Li_1 and Li_2 sites disorderly when repulsive forces between lithium-ion are taken into account. For instance, the Li_1 position is occupied, and 2 adjacent Li_2 positions are vacant; the following Li_2 positions are occupied, and Li^+ will migrate through this pathway. Cubic-LLZO is more suitable as an ion conductor since it has twice the lithium-ion conductivity of tetragonal-LLZO. Although the cubic phase of pure LLZO is unstable at RT, it can easily convert to tetragonal-LLZO [113–115]. Element doping is effective to stabilize the cubic LLZO. Zirconium (Zr) and lanthanum (La) could be partially replaced/substituted by various transition metals. Li et al. [109] revealed that the garnet-based electrolytes $\text{Li}_{56.4}\text{La}_3\text{Zr}_{1.4}\text{Ta}_{0.6}\text{O}_{12}$ showed an ionic conductivity of 1.0×10^{-3} S cm $^{-1}$ and a low quantity of activation energy of 0.35 eV. Buschmann et al. [110] described a cubic structure of Al-doped LLZO showing an ionic conductivity of 4.0×10^{-4} S cm $^{-1}$, while the pristine tetragonal LLZO exhibited an ionic conductivity of 2.0×10^{-6} S cm $^{-1}$. Aguadero et al. [116] achieved the dense Ga-substituted LLZO under a dry O_2 atmosphere, and the Ga-substituted LLZO showed an ionic conductivity of 2.2×10^{-3} and 1.3×10^{-3} S cm $^{-1}$ at 42 and 24 °C, respectively.

Sulfide-based solid electrolytes

The lithium thiophosphates or sulfide electrolytes are considered prospective solid electrolyte candidates for ASSBs due to their high ionic conductivity and low electronic conductivity [117]. It was also promulgated that thiophosphate crystalline compounds such as $\text{Li}_{10}\text{GeP}_2\text{S}_{12}$, glass-ceramics $\text{Li}_x\text{P}_3\text{S}_{11}$ and Li_3PS_4 , and argyrodite have proven characteristics as superionic conductors [67,118,119].

The sulfide-based electrolytes have received a lot of interest because of their high ionic conductivity ($\sim 10^{-2}$ S cm $^{-1}$), which is comparable to the liquid electrolytes. Furthermore, the Li-ion conductivity in the lithium-based thiophosphate solid electrolyte was stated to consist of the distribution of structural unit PS_4^{3-} tetrahedral geometry, which is recommended as a conductive framework for lithium conduction. The thiophosphate solid-state electrolytes have higher Li-ion conductivity but lower chemical stability than the oxide-based solid-state electrolytes. The chemical sensitivity of the sulfide-based electrolytes to moisture requires complicated preparation under the argon environment, which increases the manufacturing cost. In a nutshell, solid sulfide electrolytes are believed to be promising for ASSBs. The sulfide-based solid electrolytes have been extensively investigated, while choosing a sulfide electrolyte with good chemical stability is quite challenging. For instance, $\text{Li}_{10}\text{GeP}_2\text{S}_{12}$ solid electrolyte displays the highest ionic conductivity

of $\sim 10^{-2}$ S cm $^{-1}$ but is unstable against Li metal anode and is highly sensitive to moisture.

Thio-LISICON

The combination of Li_4SiO_4 and $\gamma\text{-Li}_3\text{PO}_4$ produces LISICON, in which the O atoms are replaced by the S atoms, resulting in an escalation to the thio-LISICON with 3-order higher Li $^{+}$ conductivity [120,121]. The structure of LiGeS_4 is composed of hexagonal (close-packed) sulfide ions, and Li and Ge ions are distributed over the octahedral and tetrahedral sites. Most importantly, Li_3S_6 (octahedra) is linked via edge sharing along the b axis forming $(\text{LiS}_6)_{\infty}$. GeS_4 (tetrahedra) is isolated and connected to the $(\text{LiS}_6)_{\infty}$ chain along edge sharing. Li_1S_4 (tetrahedra) is linked with Li_3S_6 (octahedra) via edge sharing, although Li_2S_4 (tetrahedra) is also linked to the octahedra via face sharing. There are many interstitial positions between the Li_1S_4 tetrahedra and $(\text{LiS}_6)_{\infty}$ chains, and lithium unoccupation was found in the interstitial site. The Li distribution in Li_4GeS_4 remains analogous to that of Li_3PS_4 except for the Li1 tetrahedra. Three Li sites are represented: Li3, Li2, and Li1*, corresponding to octahedral, tetrahedral, and tetrahedral sites, respectively. The tetrahedral site in Li_3PS_4 , Ge $^{4+}$, is substituted by P $^{5+}$, and the Li2 and Li3 sites have identical coordination in Li_4GeS_4 . There is a Li1* site in the Li_3PS_4 structure, similar to the interstitial site in LiGeS_4 located between Li_1S_4 tetrahedra and $(\text{LiS}_6)_{\infty}$ chains. Figure 10A and B depicts the Li_1S_4 tetrahedra, Li1* S_4 tetrahedra, and $(\text{LiS}_6)_{\infty}$ chains. Li_3PS_4 consists of an octahedral Li3 site and 2 tetrahedral Li1* sites, which design the chains along the b axis. Li diffusion may occur via a pathway comprising Li1*-Li3-Li1*. In Li_4GeS_4 , there was no significant deviation. Li_4GeS_4 shows no lithium occupancy at the interstitial Li1* site, whereas Li_3PS_4 has partial occupancy at these 2 sites [122]. In thio-LISICON, Li-ion conductivity strongly depends on the polarizability and size of constituent ions; thus, Ge-based thio-LISICON has higher Li conductivities than the counterpart of Si-based thio-LISICON. The argyrodite electrolyte was created using the same approach and had the same conduction mechanism [123,124]. The sulfide (S $^{2-}$) has higher atomic size and polarizability than oxide (O $^{2-}$), which increases the volume of the lattice for fast Li $^{+}$ conduction [121].

Li_3PS_4

Tachez et al. [125] reported that the chemically stable phase Li_3PS_4 could be synthesized using a stoichiometric ratio of $\text{Li}_2\text{S}\text{-P}_2\text{S}_5$. The ionic conductivity of Li_3PS_4 is 3×10^{-7} S cm $^{-1}$ at ambient temperature. The $\beta\text{-Li}_3\text{PS}_4$ phase has a higher ionic conductivity than the $\gamma\text{-Li}_3\text{PS}_4$ phase. When the temperature is below 195 °C, the $\beta\text{-Li}_3\text{PS}_4$ phase converts to the low Li-ion conductive $\gamma\text{-Li}_3\text{PS}_4$ phase. The $\gamma\text{-Li}_3\text{PS}_4$ phase (space group: Pmn_2_1) has 6 Li-ion sites with 2 fully occupied positions of 4b and 2a. The arrangement of the PS_4 tetrahedra in the crystal structure is shown in Fig. 10C. The $\beta\text{-Li}_3\text{PS}_4$ phase (space group: $Pmna$) has 3 Li-ion sites of 4b, 4c, and 8d in Fig. 10D. The Li occupation of 4c, 4b, and 8d sites in $\beta\text{-Li}_3\text{PS}_4$ is about 30%, 70%, and 100%, respectively. The BV method determines the ion transport path and energy barrier. Figure 10C shows the diffusion channels of the $\gamma\text{-Li}_3\text{PS}_4$ phase. Lepley et al. [126] reported that it is challenging for the Li-ion to migrate along the b axis. The migration pathways along the c and a axes include the interstitial sites, such as the hopping of lithium ions via 4b-2a sites within the PS_4 tetrahedral layer, as represented by a green arrow with the most favorable energetic conditions. A threshold

of 1.09 eV is required for interlayer ion migration along the a axis, and moving from 4b to 4b is challenging. Ion migration along the b axis is smoother than along the c axis, while conduction along the a axis is less favorable. The overall conduction along the b axis is also linked to the chain of 8d-8b-8d represented by the green-colored arrows. The Li-ion hopping within the tetrahedral PS_4 via 8d-8b-8d is much smoother than the channel from 8d to 8d, represented by the red arrows (one PS_4 layer to another PS_4) in Fig. 10C and D [22,127]. Some other MX_4 ($M = \text{P, Si, and Ge}$; $X = \text{O, S}$) materials with tetrahedral arrangements are likely to have identical structural variations and structure–property associated with Li_3PS_4 . The nanoporous morphology of $\beta\text{-Li}_3\text{PS}_4$ has been produced with metastable phase stability, showing the highest Li $^{+}$ conductivity of 1.6×10^{-4} S cm $^{-1}$ at RT [128].

$\text{Li}_{10}\text{GeP}_2\text{S}_{11}$

Currently, the outstanding LISICON solid electrolyte is LGPS, which exhibited the highest lithium ion conductivity of 1.2×10^{-2} S cm $^{-1}$ at RT [57]. One kind of conductive frame is made up of $(\text{Ge}_{0.5}\text{P}_{0.5})\text{S}_4$ tetrahedra joined with octahedral (LiS_6) by simple edge sharing to create a 1D chain coupled with tetrahedral (PS_4) via corner sharing. The Li-ion can migrate from one point to the next along the c axis in a zigzag conduction pattern. Li-ion migration channels are provided by tetrahedrally coupled Li sites 8f and 16h; however, the conductive framework chains octahedrally coordinating Li site 4d are inactive for ion conduction in Fig. 10E and F [67]. Adams and Prasada Rao [129] found the low-energy lithium site 4c by MD calculations and concluded that the 4c Li site participated in the conduction perpendicular to the 1D chain. By first-principles calculations, Mo et al. [68] projected that LGPS is a 3D rather than a 1D conductor due to the notable Li hopping in the ab plane and vacant space between LiS_4 tetrahedra and $(\text{Ge}_{0.5}\text{P}_{0.5})\text{S}_4$ tetrahedra. Nevertheless, the Li-ion migration along the ab plane is very slow. The Li-ion conductivity in the ab plane has been prophesied to be 9.0×10^{-4} S cm $^{-1}$ at RT. The LGPS electrolyte has a high value for Li-ion conductivity and is nearly the conventional liquid electrolyte. Nonetheless, the high cost of germanium (Ge) precludes commercial-scale development and implementation in ASSBs. In view of this, Ge has been substituted by Sn and Si to achieve cost-effectiveness, but this reduces its ionic conductivity [130]. $\text{Li}_{9.54}\text{Si}_{1.74}\text{P}_{144}\text{S}_{11.7}\text{Cl}_3$ as an emerging solid-state electrolyte for ASSBs showed the highest Li-ion conductivity of 2.5×10^{-2} S cm $^{-1}$ [119]. The LGPS structure has 1D conductive frameworks made up of the edge sharing of the tetrahedra of MX_4 ($M = \text{P, Si}$ and $X = \text{Cl, S}$) connected by tetrahedra PX_4 ($X = \text{Cl, S}$) in Fig. 10G and H. The active Li-ion is positioned at interstitial sites of 4c, 8f, and 16h; their highest Li-ion conductivity is credited to the 3D ion migration in the crystal structure.

Argyrodites $\text{Li}_{7-x}\text{PS}_6\text{X}_x$

Another family of sulfide-type electrolytes is known as argyrodites. The argyrodites are derived from Ag_8GeS_6 [131] and $\text{Cu}_6\text{PS}_5\text{Cl}$ [132], which exhibit high Ag $^{+}$ and Cu $^{+}$ ion conductivity of Ag_8AlSe_6 . First, Deisereth et al. [133] presented a new class of Li-ion conductive argyrodites $\text{Li}_{7-x}\text{PS}_6\text{X}_x$ ($\leq x \leq 1$; $X = \text{I, Br, Cl}$) in 2008, and their lithium ion conductivity ranges from 10^{-3} to 10^{-4} S cm $^{-1}$. Rao and Adams [134] reported a high Li-ion conductivity of 7×10^{-3} and 3×10^{-3} S cm $^{-1}$ for $\text{Li}_6\text{PS}_5\text{Br}$ and $\text{Li}_6\text{PS}_5\text{Cl}$ at RT, respectively. The difference in Li-ion conductivity

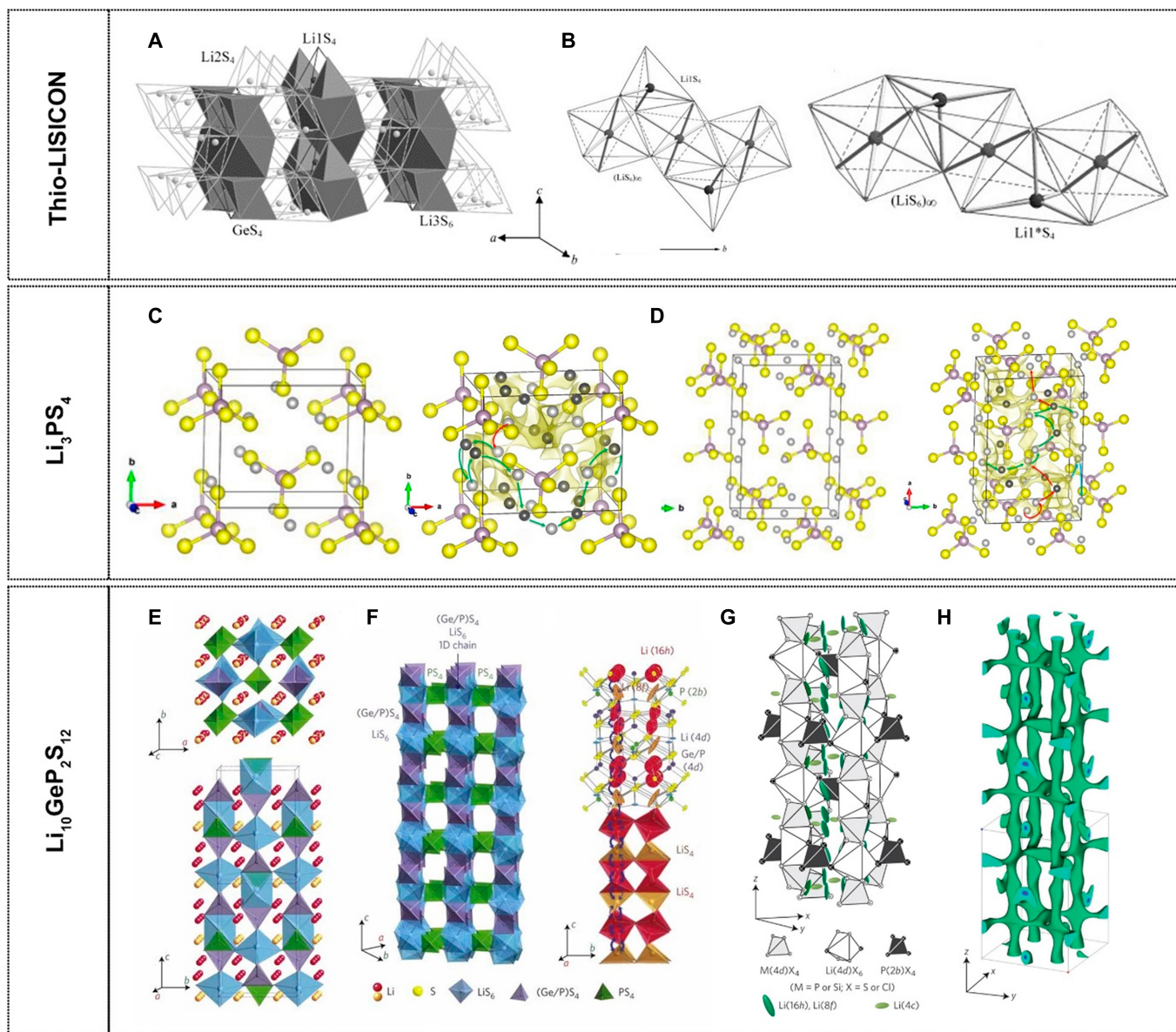


Fig. 10. (A) Crystal structure of Li_4GeS_4 . The schematic of the Li conduction channels in Li_4GeS_4 and Li_3PS_4 is shown. (B) Li1S_4 tetrahedra (Li_4GeS_4), $(\text{LiS}_6)_{\infty}$ chains (both structure), and Li11S_4 tetrahedra (Li_3PS_4). Reprinted with permission from [122]. Copyright 2002, Elsevier. (C) Atomic structure of γ - Li_3PS_4 and schematic illustration of Li-ion migration pathways in γ - Li_3PS_4 . (D) Atomic structure of β - Li_3PS_4 and schematic illustration of Li-ion migration channels in β - Li_3PS_4 . The green-colored arrows, blue-colored arrows, and red-colored arrows show smooth, moderate, and difficult migration pathways, respectively. Reprinted with permission from [127]. Copyright 2019, Elsevier. (E) Crystal structure of $\text{Li}_{10}\text{GeP}_2\text{S}_{12}$ (LGPS). (F) 1D conduction framework in the LGPS formed by LiS_6 and $(\text{Ge}_0.5\text{P}_0.5)\text{S}_4$, which is coordinated via edge sharing. These chains are linked by the corner sharing with PS_4 and the zigzag conduction pathway of the Li-ion along the c axis. Reproduced with permission from [67]. Copyright 2011, Springer Nature. (G) Crystal structure of the $\text{Li}_{9.54}\text{Si}_{1.74}\text{P}_{144}\text{S}_{11.7}\text{Cl}_3$ electrolytes and the conductive structure comprises 1D polyhedral chains and $\text{Li}(4d)\text{X}_6$ and $\text{M}(4d)\text{X}_4$ linked by $\text{P}(2b)\text{X}_4$. Li is positioned on the interstitial site of $\text{Li}(4c)$, $\text{Li}(8f)$, and $\text{Li}(16h)$. (H) Nuclear distributions of Li in $\text{Li}_{9.54}\text{Si}_{1.74}\text{P}_{144}\text{S}_{11.7}\text{Cl}_3$ electrolytes. Reproduced with permission from [119]. Copyright 2016, Springer Nature.

between these solid electrolytes lies in the difference in anion disorder due to the partial substitution between the S^{2-} and X^- sites. The argyrodite electrolytes have 3 lithium sites and 3D conduction pathways, which consist of interlinked cage networks around anion sites. The equilibrium $48h$ (Li1) site has the minimum energy, and $24g$ (Li2) is the interstitial site between the Li1 sites in Fig. 11A and B. In this network cage, 3 Li_2 molecules and 3 Li1 molecules form a low-energy hexagon, and 4 hexagons are linked by interstitial $\text{Li3}(16e)$ molecules in order to form a cage-like structure around anion sites. Further 3D conductive pathway cages are interconnected to

form another set of ion conduction channels. $\text{Li}_6\text{PS}_5\text{I}$ exhibited a higher activation barrier between the Li3 and Li1 sites, leading to low Li-ion conduction as compared to $\text{Li}_6\text{PS}_5\text{X}$ with smaller ($\text{X}^- = \text{Cl}^-$ and Br^-) anion [135–137]. According to Minafra et al. [138], replacing P^{5+} in the argyrodite $\text{Li}_6\text{PS}_5\text{Br}$ structure with Si^{4+} can increase the size of the unit cell. Due to this variation, additional Li-ion can be driven from the equilibrium site to another transition site of $24g$, improving the migration of Li-ions. The outcomes are a 3-fold increment in the Li^+ conductivity of $2.4 \times 10^{-3} \text{ S cm}^{-1}$ at RT for $\text{Li}_{6.35}\text{P}_{0.65}\text{Si}_{0.35}\text{S}_5\text{Br}$.

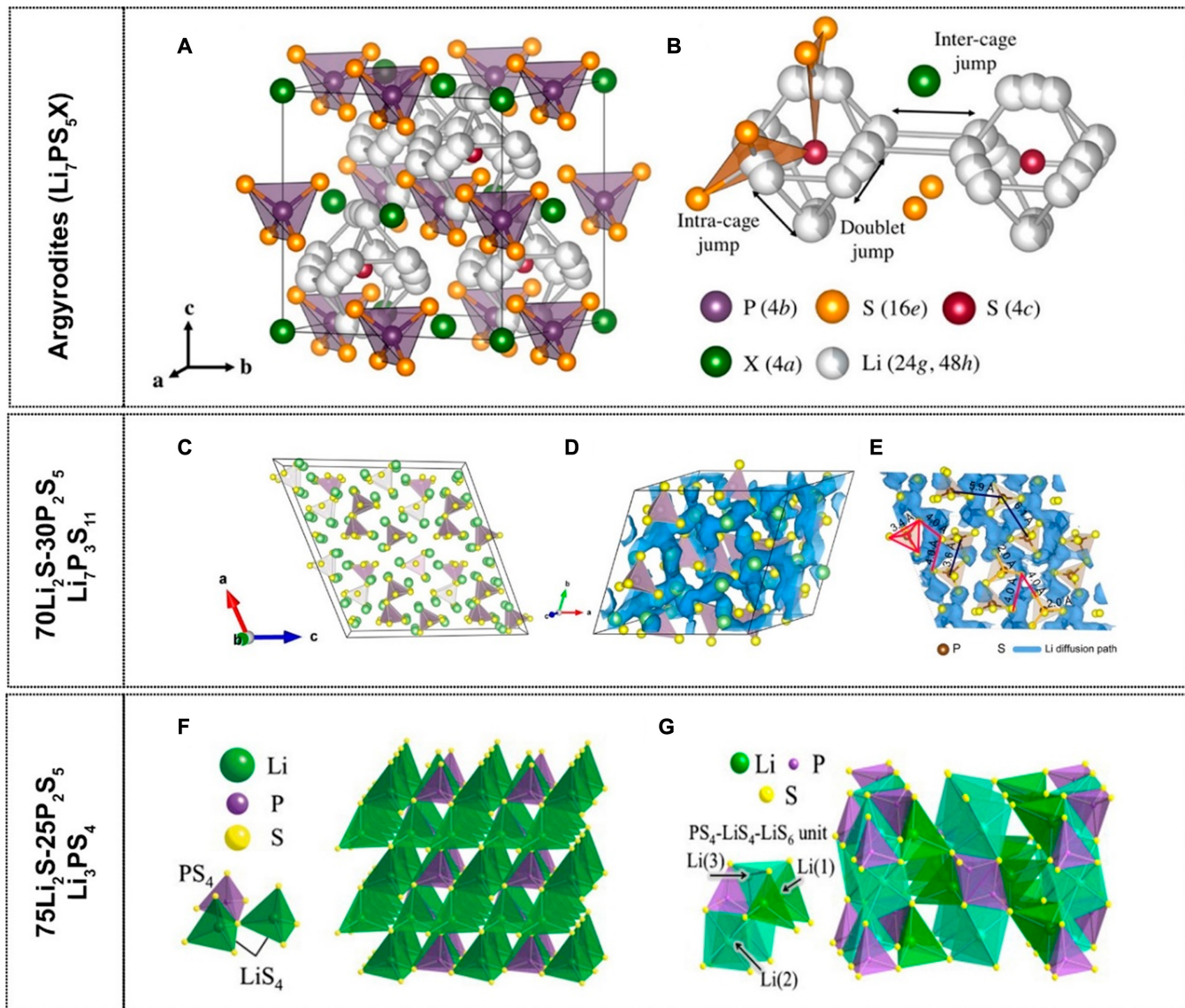


Fig. 11. (A) Structure of $\text{Li}_6\text{PS}_5\text{X}$ ($\text{X} = \text{I, Br, and Cl}$). In the crystal structure of $\text{Li}_6\text{PS}_5\text{X}$, X^- positioned a cubic close-packed lattice with the tetrahedra (PS_4^{3-}) in the octahedral sites. (B) S^{2-} and the corner of the tetrahedra (PS_4^{3-}) form polyhedra that enclose 2 Li sites. The lithium sites generate localized cages that allow for multiple jump processes. Jumps between the lithium sites (48h-24g-48h, double jump), i.e., inter-cage jumps and intra-cage jumps (48h-48h), are possible. The inter-cage jumps are prone to govern the long-range migration. The position disorder between the 4c and 4a sites influences the ionic conductivity expressively. Adopted with permission from [137]. Copyright 2017, American Chemical Society. (C) Crystal structure of the solid $\text{Li}_7\text{P}_3\text{S}_{11}$ electrolytes. The PS_4 (tetrahedra) and lithium (green) and sulfur (yellow) atoms are shown. (D) Iso-surface of probability density distribution in blue; $\text{P}(\text{r})$ of Li-ions in $\text{Li}_7\text{P}_3\text{S}_{11}$ with $P = 0.001$ at 600 K from AIMD simulation. Adopted with permission from [70]. Copyright 2016, American Chemical Society. (E) Pair distribution function, $G(\text{r})$, achieved the AIMD simulation at 500 K. Adopted with permission from [194]. Copyright 2018, American Chemical Society. (F) Crystal structure of the $\gamma\text{-Li}_3\text{PS}_4$ phase. (G) Crystal structure of the $\beta\text{-Li}_3\text{PS}_4$ phase. Reprinted with permission from [142]. Copyright 2010, Elsevier.

$\text{Li}_2\text{S-P}_2\text{S}_5$ binary glass and glass-ceramics

The binary system of $\text{Li}_2\text{S-P}_2\text{S}_5$ glass and glass-ceramics is a remarkable solid electrolyte for solid-state batteries. The crystallization parameter of the parent Li_3PS_4 glass system results in the various types of sulfide solid electrolytes, such as $\text{Li}_2\text{P}_2\text{S}_6$ ($50\text{Li}_2\text{S-50P}_2\text{S}_5$), $\text{Li}_4\text{P}_2\text{S}_6$ ($67\text{Li}_2\text{S-33P}_2\text{S}_5$), $\text{Li}_7\text{P}_3\text{S}_{11}$ ($70\text{Li}_2\text{S-30P}_2\text{S}_5$), Li_3PS_4 ($75\text{Li}_2\text{S-25P}_2\text{S}_5$), and Li_7PS_6 ($78\text{Li}_2\text{S-22P}_2\text{S}_5$). The Li^+ conductivity of the binary system of $\text{Li}_2\text{S-P}_2\text{S}_5$ can be tuned by changing the synthesis parameters, including annealing temperature, time, and stoichiometric ratio of Li_2S as well as P_2S_5 [139]. The Li-ion conductivity of the annealed glass-ceramic electrolytes depends on their composition due to the various phases crystallized from the glass precursors.

The glass-ceramics achieved by annealing the $70\text{Li}_2\text{S-30P}_2\text{S}_5$ glass composition at 250 to 360 °C exhibit a Li-ion conductivity of $10^{-3} \text{ S cm}^{-1}$, which is larger than their parent glass composition. After the in-depth analysis, it was found that the main crystalline phase formed in the $70\text{Li}_2\text{S-30P}_2\text{S}_5$ glass composition at 250 to 360 °C was $\text{Li}_7\text{P}_3\text{S}_{11}$ with triclinic cell geometry (space group $P-1$). The structure of $\text{Li}_7\text{P}_3\text{S}_{11}$ consists of $\text{P}_2\text{S}_7^{4-}$ (corner-shared di-tetrahedra) and PS_4^{3-} (tetrahedra) surrounded by the lithium ions in Fig. 11C. The lithium-ion conduction is due to the large number of interstitial sites and large spaces between the PS_4^{3-} tetrahedra and $\text{P}_2\text{S}_7^{4-}$ di-tetrahedra. In the $\text{Li}_7\text{P}_3\text{S}_{11}$ structure, the ion diffusion channels form the 3D networks in which all Li-ion are connected to each other by empty

S_4 tetrahedra in Fig. 11D and E. The Li sites are completely occupied, suggesting that the Li-ion can migrate collectively [70]. Li^+ migrates between the stable regions within a jump length (4.3 Å) of the $Li_7P_3S_{11}$ metastable phase in the glass-ceramics. In the $Li_7P_3S_{11}$ metastable phase, part of the Li-ions participates in ion transportation. The difference between immobile and mobile and Li ions is directly connected with the lithium sites or the Li-Li bonds [140,141]. The structural framework, specifically the LiS_4 tetrahedral-based networks of $Li_7P_3S_{11}$ metastable phase with a large Li jump length, will be a key attribute in exploring the new superionic conductors.

With the increasing ratio of Li_2S , the Li_3PS_4 phase is also crystallized with the composition of the $75Li_2S-25P_2S_5$ glass composition at 220 to 700 °C. The Li_3PS_4 phase is often supposed to be a thio-LISICON III phase due to its third compositional region of the reported $Li_3PS_4-Li_4GeS_4$ binary system. There are 3 structural polymorphs of Li_3PS_4 : the high-temperature α - Li_3PS_4 phase, moderate-temperature β - Li_3PS_4 phase, and low-temperature γ - Li_3PS_4 phase. The γ - Li_3PS_4 phase was first discovered in 1984 with an ionic conductivity of $3 \times 10^{-7} S cm^{-1}$ at RT [70]. The PS_4^{3-} tetrahedra are positioned and isolated from each other and are linked with LiS_6 (octahedron) by edge sharing. The apex of the PS_4^{3-} forms zigzag arrangements and is also described above in detail. The identical zigzag arrangements are also observed in the α - Li_3PS_4 phase. The structural differences of the γ - Li_3PS_4 , β - Li_3PS_4 , and α - Li_3PS_4 phases can be elucidated based on the PS_4^{3-} tetrahedron arrangements in Fig. 11F and G. The β - Li_3PS_4 phase displayed a Li-ion conductivity of $3.0 \times 10^{-2} S cm^{-1}$ at 500 K due to the suitable arrangement of the PS_4^{3-} tetrahedron for Li-ion conduction [142]. An identical thio-LISICON III crystallization with increased Li_2S concentration, such as $78Li_2S-22P_2S_5$ glass composition by controlling the crystallization kinetics, shows a Li-ion conductivity of $8.5 \times 10^{-4} S cm^{-1}$ at RT [143]. A new crystalline phase identical to the thio-LISICON II analog and the Li_2PS_6 phase was also detected when the glass sample of $78Li_2S-22P_2S_5$ was heated at 150 to 280 °C with the highest ionic conductivity of $1.78 \times 10^{-3} S cm^{-1}$ [144]. By increasing the Li_2S part, a $Li_{3.25}P_{0.95}S_4$ crystal precipitates at the $80Li_2S-20P_2S_5$ composition, which is a thio-LISICON II (P deficient) analog and has a monoclinic crystal structure with an ionic conductivity of $\sim 10^{-3} S cm^{-1}$ at RT [145]. The Li-ion migration mechanism of these glasses and glass ceramics is a tremendous challenge for materials chemists. AIMD simulation and first-principles calculation is a valuable tool to explore the Li-ion conduction pathway within the PS4 tetrahedron structural framework containing glass and glass ceramics.

Challenges and Resolving Strategies

Design fast ionic migration in solid electrolytes

The ionic conductivity and activation energy of the solid electrolytes is strongly correlated with the ion migration related to the conductive frameworks, defects, and moveable ions. In specific conductive frameworks, the mobile ion prefers positioning the sites with the lowest energy, and ion hopping between these sites is accessible, which leads to ion conduction. The ionic conductivity requires a continuous ion hopping across a long distance to connect the channels between neighboring locations in the crystalline structures. The different locations of mobile ions along the conductive channels need to maintain a relatively smooth energy landscape or a low

migration energy barrier. Wang et al. [57] explained the basis for developing superionic conductors and exposed the important effects of the anion-host matrix on the ion conduction. These findings revealed how body-centered cubic (bcc) anion conductive networks allowed lithium ions to diffuse inside a framework of interlinked tetrahedral sites with equivalent energies, resulting in a low activation energy barrier of the $Li_7P_3S_{11}$ and LGPS solid electrolytes. Non-bcc packing frameworks, i.e., the hexagonal closed-packed and face-centered cubic, exhibited a higher energy barrier. Unfortunately, the bcc packing structure is a rare structural system in lithium-contained sulfide and oxide materials. Apart from the 3D frameworks enabling ionic conductors, the layered structure materials with the 2D ion diffusion exhibit promising solid electrolytes.

Defect introduction

The material with perfect crystallinity is hard to obtain since intrinsic and extrinsic defects are always introduced during the practical manufacturing process. More importantly, we have discussed all the defects in the above section, which are directly related to having a significant influence on ion conduction. Typically, the moveable ions do not entirely fill the position in the ion conductor, causing many vacancies for ion migration. For this purpose, the aliovalent ion substitution and doping are usually considered as a realistic strategy to regulate the defect formation in the crystalline electrolytes, which has been verified to be effective in many kinds of ionic conductors. With a small quantity of the foreign element doping or substitution at active ion sites, there are remarkable effects on increasing the concentration of mobile ions and vacancies.

Concerted ion diffusion

In the above section, we also explained the classic diffusion model, which elucidates the ion migration as the ion hopping of individual ions from one site to another. In the migration mechanism, an ion diffuses one position to other via an energy landscape, and the highest energy of the energy barrier along the migration path is the activation energy. The low activation energy (E_a) and high concentration of the charge carriers such as interstitials or vacancies are needed to design the superionic conductor. The classic diffusion model cannot explain why materials with similar energy landscapes, for example, NASICON and Garnet, exhibit different activation barriers. The investigation of these fundamental issues is helpful in designing novel superionic conductors, particularly the crystal structure that deviates from the bcc packing structures. He et al. [146] studied the migration in the LGPS (bcc anion packing) and LLZO, $Li_{1.3}Al_{0.3}Ti_{1.7}(PO_4)_3$ (LATP) (non-bcc packing) superionic conductor by AIMD simulation. It is found that most Li-ion migrates in a highly cooperated/concerted manner, i.e., simultaneous hopping of multi-ion into nearby sites. The energy barrier of the concerted migration calculated by NEB methods is consistent with the activation energies obtained from experiments. The low energy barrier for the multi-ion cooperated migration is a relatively flat energy landscape along the Li-ion migration channels. Using the classic migration model, the energy landscapes have a larger energy barrier (higher E_a) than that of the concerted migration mechanism. As a superionic conductor is only triggered at precise composition with high lithium concentration, a configuration of mobile ions and the interaction between the ions are ignored in the classical diffusion model. More importantly, the configuration of mobile

ions under strong ion-ion interaction is a key factor to attaining the concerted migration in the superionic conductors. To design a superionic conductor, the insertion of mobile ions into the high-energy sites triggers the concerted ion diffusion with a lower energy barrier. The insertion of the Li-ion into the high energy sites is attained by high lithium concentration in the structure and aliovalent substitution of nonlithium cations with lesser valences.

Conductive and facilitative framework for ion conduction

The energy barrier of moveable ions in the crystalline structure depends on the crystal structure and the bonding interaction of skeleton ions. The particular concepts related to the conductive and facilitative framework for ion conduction are described below.

Lattice polarizability

Mobile ion polarizability is defined as the capability to create instantaneous dipoles. In general, the large size is also more polarizable. The saddle point must be passed during ion hopping; the anharmonic relaxational motion is determined by the skeleton lattice in Fig. 12A [147]. Polarizability is directly related to bond strength, where anions with higher polarizability

are likely to have large electronic clouds and weak bond connections. Several researchers have explored the effects of altering the lattice polarizability on ionic migration in lithium ionic conductors [148–150]. These findings also represented higher anion polarizability and lower activation barrier for the ion migration in Fig. 12B. Several examples of ion conductors that alter the strength of the local bond interaction and the anion framework, as well as their effects on the conductivity, are represented in Fig. 12C.

Lattice softness

A polarizable and softer anion framework aids ionic migration by lowering the Debye frequency. Debye frequency is a measure of all vibrational lattice features, and a single ion jump is most likely influenced by a few distinct phonon modes. The changes in the energy landscape for the Li-ion migration due to lattice softening are represented in Fig. 12B. During lattice softening, the bonding interaction between skeleton ions and mobile ions becomes weaker, allowing the local jump mode to oscillate, thereby lowering the activation barrier. In this regard, Se has not only a greater ionic radius than S but also an identical formal charge, making it appropriate and more polarizable to design a

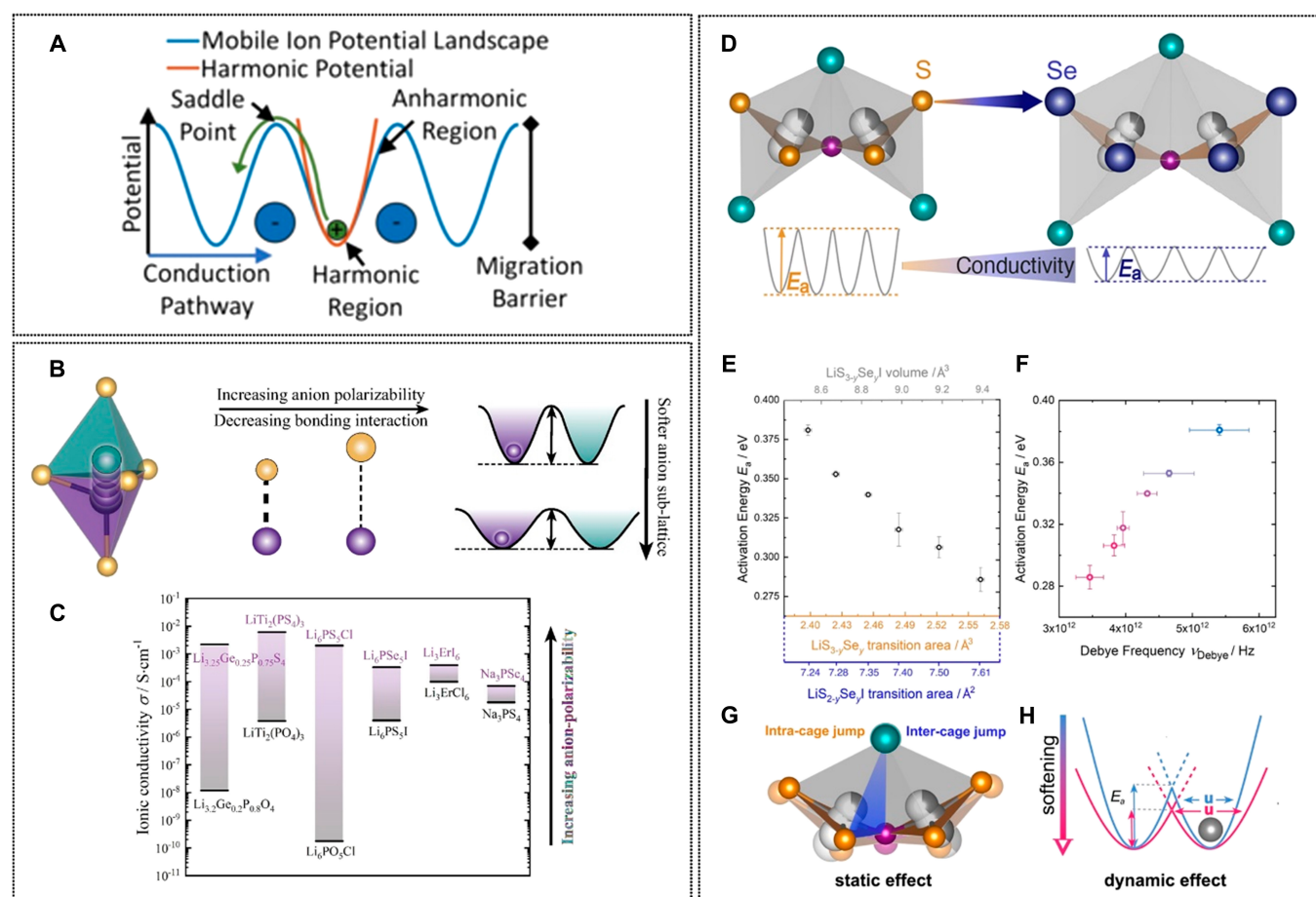


Fig. 12. (A) Classical ion migration mechanism in which ion hops across the energy barrier in the energy landscape because of host lattice and nearby mobile ion. Adopted with permission from [147]. Copyright, APS. (B) Schematic illustration of mobile ion and respective energy landscape. With increasing polarizability, the anion undergoes a weak and longer bond that softens the anion lattice and lowers the energy barrier. Reprinted with permission from [195,196]. Copyright 2020, Wiley-VCH GmbH. (C) The ionic conductivity of various materials displaying the anion polarizability can alter ionic migration significantly [196]. (D) Effects of the substitution of S with Se in $\text{Li}_6\text{PS}_{5.2}\text{Se}_{0.8}\text{I}$. (E) Relationship between the transition area of Li-ion migration and the activation barrier. (F) Relationship between the activation barrier and lattice dynamics and the linear relation of the Debye frequency and activation barrier. (G) Schematic illustration of the migration pathway and broader bottlenecks. (H) Schematic representation of the influence of lattice softening on the ionic jump. Adopted with permission from [149]. Copyright 2020, American Chemical Society.

softer framework such as $\text{Li}_6\text{PS}_{5-x}\text{Se}_x\text{I}$ [149] and $\text{Li}_6\text{PS}_{5-x}\text{Se}_x\text{Cl}$ and $\text{Li}_6\text{PS}_{5-x}\text{Se}_x\text{Br}$ [150,151]. The activation barrier is generally decreased by introducing the Se more polarizable anion. The activation barrier decreases with increased volume of the diffusion path that regulates ions jumping within Li-ion cages and interchanging jumps. Lattices become softer as selenium content increases in Fig. 12D to F. Along with the volume of diffusion paths, the polarizability and softness of the lattice are also important for the design of superionic conductor. Xu et al. [152] showed that the DFT calculation explored the effects of the lattice volume, stability of the Li^+ occupation, and diffusion in the face-centered cubic (fcc) crystal structure. By controlling the non-Li element candidates within the crystal structure, low energy barriers can be attained by achieving the desired electronegativity difference between the anion and the non-Li cation element.

Matrix disorder

The creation of structural disorder is an effective strategy to increase the ionic conductivity in solid electrolytes. For example, the $\text{Li}_6\text{PS}_5\text{Cl}$ and $\text{Li}_6\text{PS}_5\text{Br}$ solid electrolytes exhibit higher ionic conductivity than $\text{Li}_6\text{PS}_5\text{I}$. The high ionic conductivity of $\text{Li}_6\text{PS}_5\text{Cl}$ and $\text{Li}_6\text{PS}_5\text{Br}$ has been attributed to anion disorder, which facilitates long-range ion migration. A structurally ordered $\text{Li}_6\text{PS}_5\text{I}$ solid electrolyte disrupts long-range ion migration and allows mobile ions to migrate over long distances via a Li jump migration path [152]. The argyrodites have 2 Li-ion sites, i.e. 24g and 48h Wyckoff positions, which form Li-ion cages around S^{2-} on the Wyckoff 4f position. Three kinds of inequivalent site jumps are demonstrated in Fig. 13A, i.e., 48h-48h intra-cage jump, 48h-24g-48h doublet jump, and 48h-48h inter-cage jump [137,153]. Br and Cl at the S^{2-} and X^- positions display a small fraction of anion site disorder [135,136]. No site disorder happens for I in the $\text{Li}_6\text{PS}_5\text{X}$ structure because of the big size mismatch between I^- and S_2^- . The X^- sites are nearby to the bottleneck path for the Li-ion jump. If the site disorder is located, a significantly lower activation barrier can be achieved [137,154]. The substitution of the $\text{Li}_{6+x}\text{P}_{1-x}\text{Ge}_x\text{S}_5\text{I}$ solid electrolyte with Ge^{4+} has demonstrated the advantages of site disorder for Li-ion conduction [155]. With cumulative $\text{Li}^+/\text{Ge}^{4+}$ fraction, the lattice volume enlarges and the degree of site disorder increases, resulting in a flat energy landscape as well as an improved Li-ion conductivity in $\text{Li}_{6+x}\text{P}_{1-x}\text{Ge}_x\text{S}_5\text{I}$ [156]. With the cumulative $\text{M}^{4+}/\text{P}^{5+}$ ratio ($\text{M} = \text{Sn}$ and Si), Zeier discovered the structural variation and its influences on the Li-ion conduction as compared to the variation found in $\text{Li}_{6+x}\text{P}_{1-x}\text{Ge}_x\text{S}_5\text{I}$. The activation barrier for a solid solution containing $\text{Li}_{6+x}\text{P}_{1-x}\text{Ge}_x\text{S}_5\text{I}$ was drastically reduced as the energy landscape was flattened out over the activation of local site disorder between I^- and S^{2-} [157] in Fig. 13B. Recently, Banik et al. [158] studied the effect of anionic and cationic substitution on the electrochemical stability of $\text{Li}_6\text{PS}_5\text{X}$ electrolytes with a combined experiment and computation approach. In $\text{Li}_6\text{PS}_5\text{CN}$, the cyanide ions have an orientational disorder that allows for complex interplay of lattice polarizability to reduce the activation barriers [159]. A new synthesis method has been developed to engineer the disorder in $\text{Li}_6\text{PS}_5\text{Br}$. Fast cooling (i.e., quenching) can be used to kinetically trap the desired anion disorder to increase the ionic conductivity, as evidenced by higher anion site disorders at elevated temperatures. By rapidly cooling, the anion site disorder is increased at high temperatures, thus allowing to kinetically trap the anticipated anion disorder, thereby increasing the ionic conductivity as shown in Fig. 13C to H [160].

In the $\text{Li}_{6+x}\text{P}_{1-x}\text{Ge}_x\text{S}_5\text{I}$ electrolytes, Hogrefe et al. [161] investigated the effect of cation substitution (P^{5+} versus Ge^{4+}) on the Li-ion conduction. $\text{Li}_6\text{PS}_5\text{I}$ exhibited low ionic conductivity. Substituting P^{5+} with Ge^{4+} produced the S^{2-}/I^- anion site disorder, and Li-ion does occupy many empty sites between the Li-rich cages in the $\text{Li}_6\text{PS}_5\text{I}$ framework. Li site disordered has a marvelous impact on both long-range Li-ion transport and local ion dynamics. A Ge-rich sample also exhibits the reduced activation barrier, and the Li-ions have access to an interconnected pathway that permits fast Li^+ exchanges between the Li cages in Fig. 14A. By the introduction of Sb^{5+} into Li_4GeS_4 , an expansion of the unit cell is detected. An additional Li-ion position is formed, and polyhedra (SbS_4^{3-}) is also located, leading to an improved local polyhedral linkage and higher disorder in the structure. By inducing structural disorder to enhance configurational entropy, a 2-order increase in Li-ion conductivity is achieved, as shown in Fig. 14B [162]. $\text{Li}_7\text{Zn}_{0.5}\text{SiS}_6$ represents a tetragonal structure with ordered Li and Zn positions at RT, which undergoes a transition to a higher symmetry disorder with $F43m$ structure above a temperature higher than 411.1 K. The activation energy barrier decreases with the transition from the ordered $I4$ structures to the disordered $F43m$ in Fig. 14C [163]. Introducing a minor quantity of Zn^{2+} effectively controls lithium order in $\text{Li}_7\text{Zn}_{0.5}\text{SiS}_6$. The local disorder can increase the ionic conductivity of $\text{Li}_{10}\text{GeP}_2\text{S}_{12}$ by a factor of 3. In LGPS, the ion dynamics are sensitively dependent on the structural disorder [164,165]. A defect concentration is crucial in understanding and controlling the ion dynamics in materials with high ionic conductivity.

Rotational motion of the polyanion

The rotational motion produced a regularly varying potential surface throughout the high-performance material, prompting ionic conduction [166]. For example, at a higher temperature, $\alpha\text{-Na}_3\text{PO}_4$ and $\alpha\text{-Li}_2\text{SO}_4$ show a plastic crystal behavior and exhibit ion conduction ability through paddle-wheel rotation of the polyanion [167,168]. However, the substitution of bigger-size polyanion (i.e., MO_4 ; $\text{M} = \text{W}, \text{V}, \text{Se}$, and Mo) in these 2 electrolytes does not cause the enhancement of the ionic conductivity as expected. Zhao et al. [169] explained that the irregular phenomenon belongs to the substitution of larger-size polyanions inhibiting the rotational motion effect of polyanion. Meanwhile, this finding also gives a reasonable explanation on the experimental result that the ionic conductivity of the solid electrolyte of $\text{Li}_{10}\text{MP}_2\text{S}_{12}$ ($\text{M} = \text{Ge}, \text{Si}, \text{Se}$) is noted to decrease with increases in the radius of the M^{4+} ion or unit cell size. A schematic representation of the rotational motion of the polyanion is shown in Fig. 15.

Prediction of stable electrochemical window

The stable electrochemical window/electrochemical stable window of solid electrolytes is a key issue in developing ASSBs with high energy density and long life. In comparison to modification (such as doping) on well-known solid electrolytes, a high-throughput screening on less-explored contender materials with good ionic conductivities values and wide stable electrochemical window can give a big database for solid electrolyte selection, hence greatly expediting ASSB development. The forecast of the stable electrochemical window is also carried out by different methods. Stable electrochemical window prediction is presently based on indirect and direct decomposition

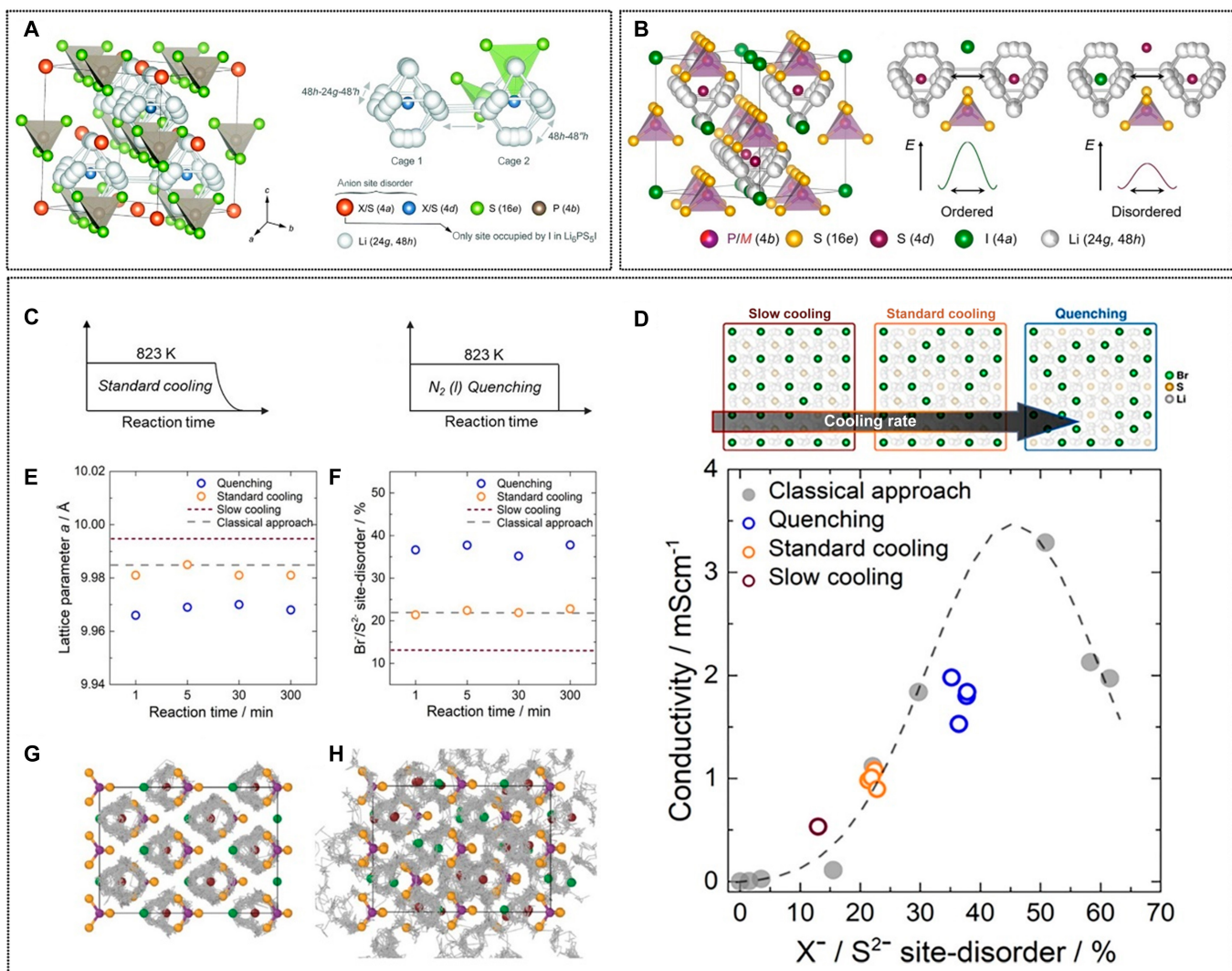


Fig. 13. (A) Structure of argyrodite $\text{Li}_6\text{PS}_5\text{X}$ ($\text{X} = \text{Cl}, \text{Br}, \text{I}$). Two lithium positions (48h, 24g) form an octahedral geometry and 3 kinds of jumps. Reproduced from [154] with permission from the Royal Society of Chemistry. (B) Structure of $\text{Li}_6\text{P}_{1-x}\text{M}_x\text{S}_5\text{I}$ ($\text{M} = \text{Si, Ge, or Sn}$). The Li migration via inter-cage jump (48h-48h) in the fully ordered structure with flattening energy landscape represented by decreasing the transition state is shown. Adopted with permission from [157]. Copyright 2019, American Chemical Society. (C) Grinded $\text{Li}_6\text{PS}_5\text{Br}$ precursor injected into the furnace at 823 K following the standard cooling and quenched cooling by liquid N_2 . (D) Comparative study of Li-ion conductivities of $\text{Li}_6\text{PS}_5\text{X}$ with different degrees of $\text{S}^{2-}/\text{Br}^-$ site disorder obtained by standard cooling, slow cooling, and quenching. As the disorder increases in the graph, the low-energy percolation paths open up, which improves Li-ion conductivity. (E) Variation in the lattice parameter is due to applied cooling approaches. (F) $\text{S}^{2-}/\text{Br}^-$ site disorder versus the reaction time of all samples where the rapid cooling process kinetically traps the high degree of disorder. The disorder leads to larger mean square displacements of the cations, and successful jumps can be found between the Li-ion cages only if the disorder is present. (G) Sites disordered. (H) Ordered structure. Adopted with permission from [160]. Copyright 2019, American Chemical Society.

analysis methods (IDAM and DDAM) that involve kinetically/thermodynamically favorable decomposition routes, resulting in a substantial deviation between the experimental and predicted stable electrochemical window. Different excellent contender solid electrolytes are continuously ignored in the screening due to the underpredict stable electrochemical window. Shi et al. described a stable electrochemical window prediction method that allows for the dynamical discovery of suitable composition pathways based on the electronic conductivities of all indirect and direct decomposition analysis methods (IDAM and DDAM). A high-throughput computation strategy is achieved on the stable electrochemical window of 328 potential Li-ion conductors with lower ion migration energy barriers from prior research, yielding good agreement with the experimental data for $\text{Li}_{10}\text{GeP}_2\text{S}_{12}$ and LLZO in Fig. 16A and B. The additional screening with different stability

tests, 6 earlier overlooked fluorides with stable electrochemical window greater than 4 V, oxidation potentials greater than 6 V and outstanding phase stability (convex hull energy of 1 meV/atom), and interfacial compatibility with 7 classic cathodes are effectively reclaimed as outstanding candidate solid electrolytes. KLiYF_5 and Li_3ScF_6 have the greatest overall performance among them in Fig. 16C [170].

The stable electrochemical window of Li_5SiBS_6 was also examined by the dynamic's presentation of the decomposition routes (indirect and direct decomposition analysis methods). Meanwhile, the finding is recommended that a broad stable electrochemical window of the Li_5SiBS_6 solid electrolyte initiates from the PS_4 tetrahedra. The dynamic decomposition route of Li_5SiBS_6 yields a stable electrochemical window value. O- Li_5SiBS_6 (orthorhombic) and T- Li_5SiBS_6 (tetragonal) have stable electrochemical window ranges of 1.4 to 2.2 V and 1.3

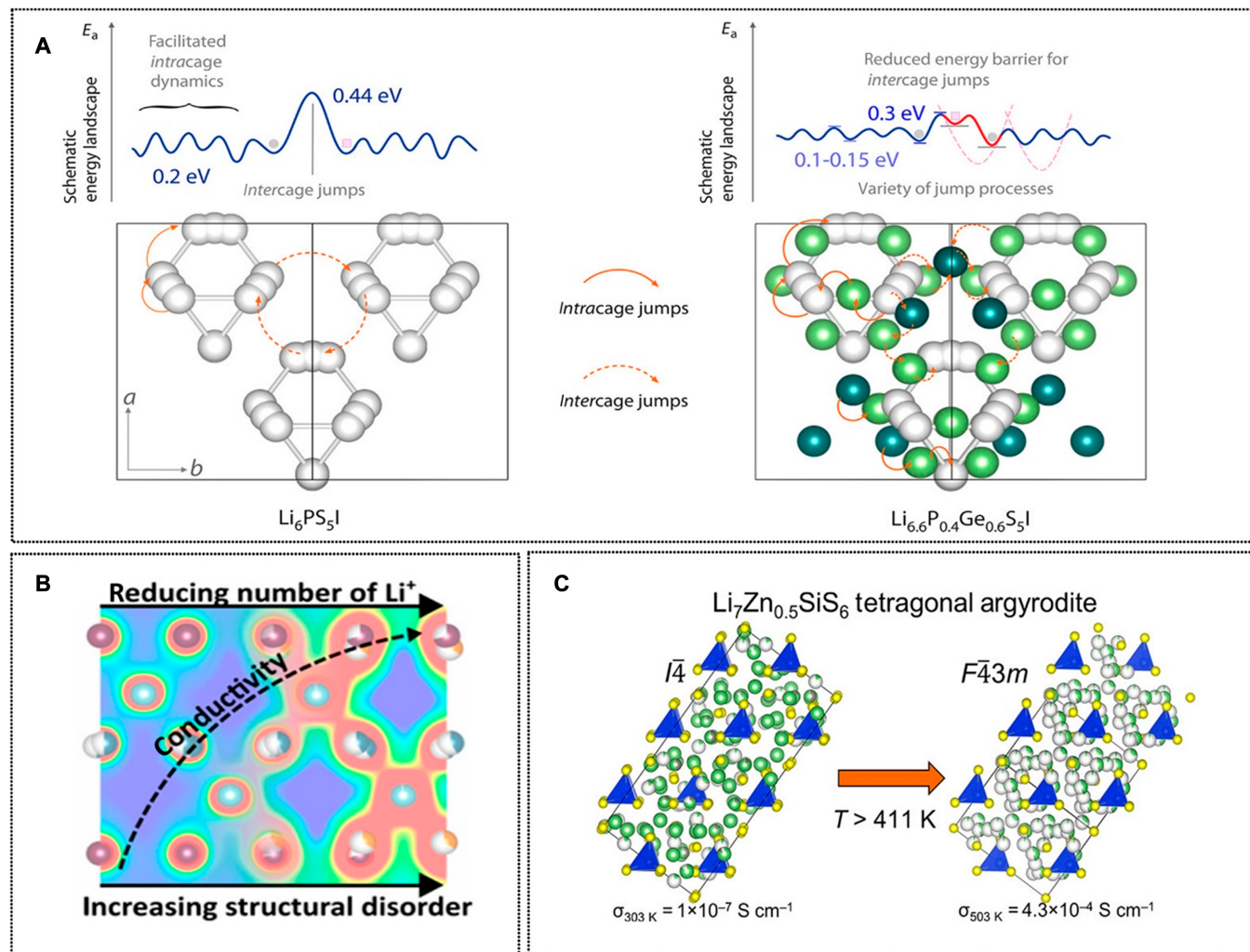


Fig.14. (A) Distribution of Li-ions in the $\text{Li}_{6+x}\text{P}_{1-x}\text{Ge}_x\text{S}_5\text{I}$ structure with (left) 0% Ge and (right) 60% Ge. The arrows show the jump direction with an energy landscape diagram. Adopted with permission from [161]. Copyright 2022, American Chemical Society. (B) Relationship between the ionic conductivity and structural disorder in thio-LISICON. Adopted with permission from [162]. Copyright 2022, American Chemical Society. (C) Transition between disordered $F\bar{4}3m$ and ordered $\bar{I}4$ structures of $\text{Li}_7\text{Zn}_{0.5}\text{SiS}_6$. Adopted with permission from [163]. Copyright 2022, American Chemical Society.

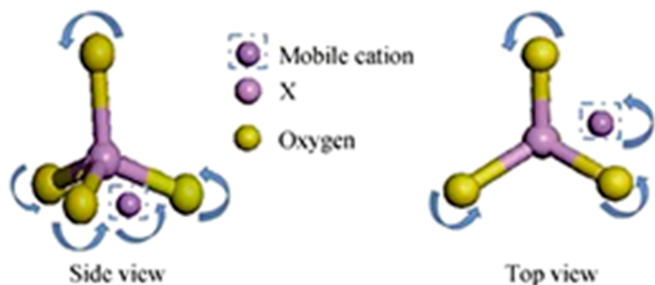


Fig.15. A graphic illustration of the rotational motion of the polyanion and cation diffusion, top and side views. Reprinted with permission from [169]. Copyright 2018, Springer Nature.

to 2.4 V, respectively. T- Li_2SiS_3 has a stable electrochemical window of around 1.5 to 2.1 V, which is slightly smaller than O- Li_2SiS_6 and T- Li_2SiS_6 . The tetrahedral structure of SiS_4 and BS_4 serves to stabilize the electrochemical window of the solid electrolyte. During lithiation/delithiation, the decomposition paths and respected equilibrium products of the

Li_5SiBS_6 solid electrolyte are illustrated at various voltages in Fig. 17A and B. It should be noted that the decomposition paths and their respective products of O- Li_5SiBS_6 and T- Li_5SiBS_6 and solid electrolytes are identical [171].

Correlated/concerted ion migration

Ion transport occurs through the complex transport mechanisms in superionic conductors. Ions can diffuse via highly coordinated mechanisms in which clusters of mobile ions move in near-synchronous cooperation. Shi et al. [172] found that Li-ion conductivity in Li_2CO_3 stems from the knock-off mechanism involving the cooperative motion of interstitial and lattice lithium ions. Mo et al. discovered that lithium ions migrate in a highly concerted/coordinated fashion, and that multiple ions hop concurrently into close positions within picoseconds is also analyzed by Li-ion dynamics from AIMD simulations. In LGPS, LLZO, and LATP, a typical concerted/coordinated ion migration mechanism is shown in Fig. 18A to F. The migration energy barriers of this concerted Li-ion migration were computed using ab initio as well as NEB computation methods. Using these methods, the energy barriers of

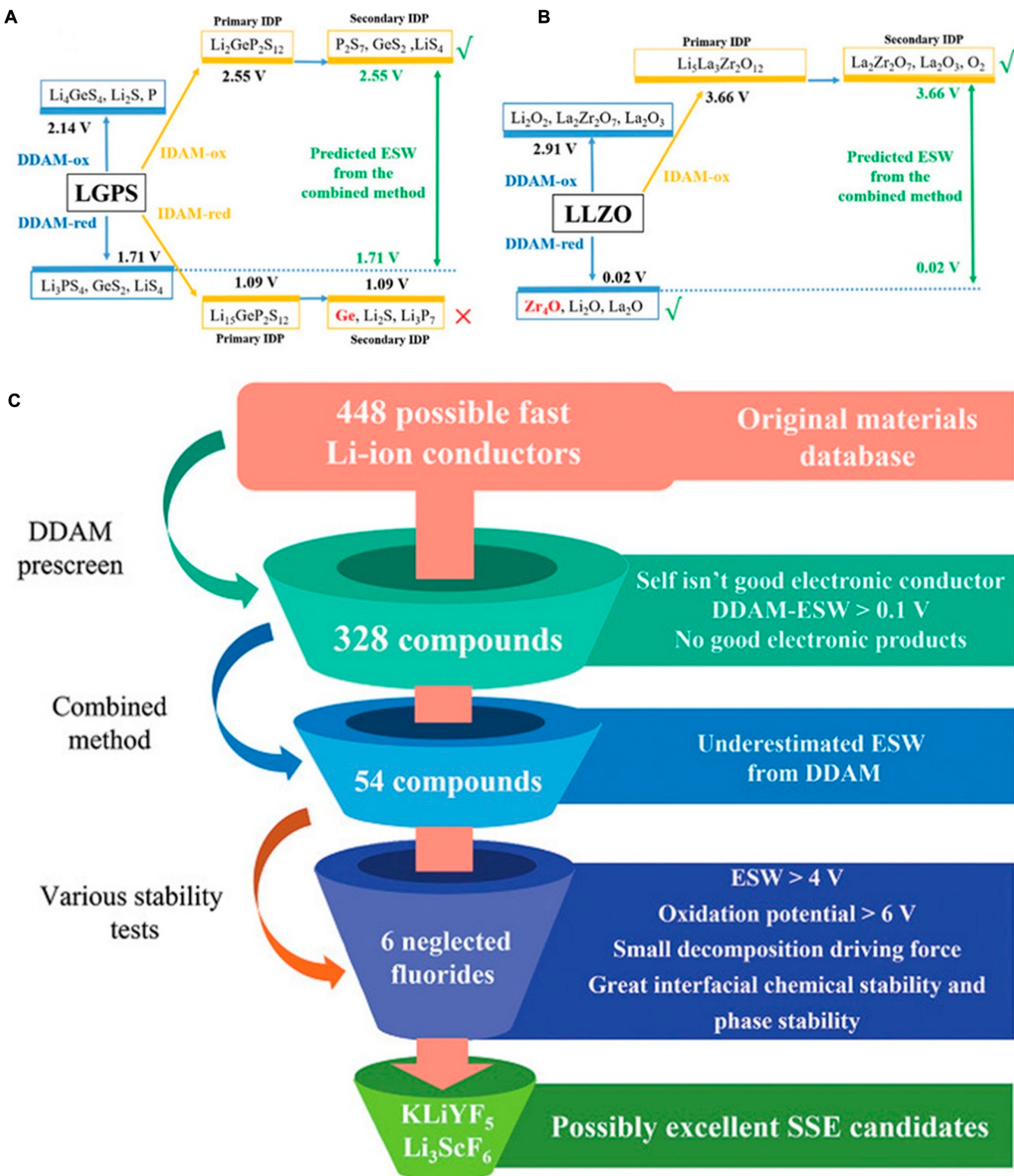


Fig. 16. Analysis of the decomposition of $\text{Li}_{10}\text{GeP}_2\text{S}_{12}$ (LGPS) (A) and garnet (LLZO) (B) by combining methods. (C) A high-throughput screening system was established to choose ignored materials as promising solid electrolyte candidates from the material database of superionic conductors. Reproduced with permission from [170]. Copyright 2022, John Wiley and Sons.

LATP, LLZO, and LGPS were calculated to be 0.27, 0.26, and 0.20 eV, respectively [146]. The computed concerted migration energy barriers are consistent with the activation energies derived from AIMD simulations and experiment values [67,106,173].

Further, Shi and colleagues [174,175] demonstrated that the relationships between crystal structure, ion distribution and concerted ion migration, and diffusion properties can be utilized to optimize ion mobility in the conductive framework by

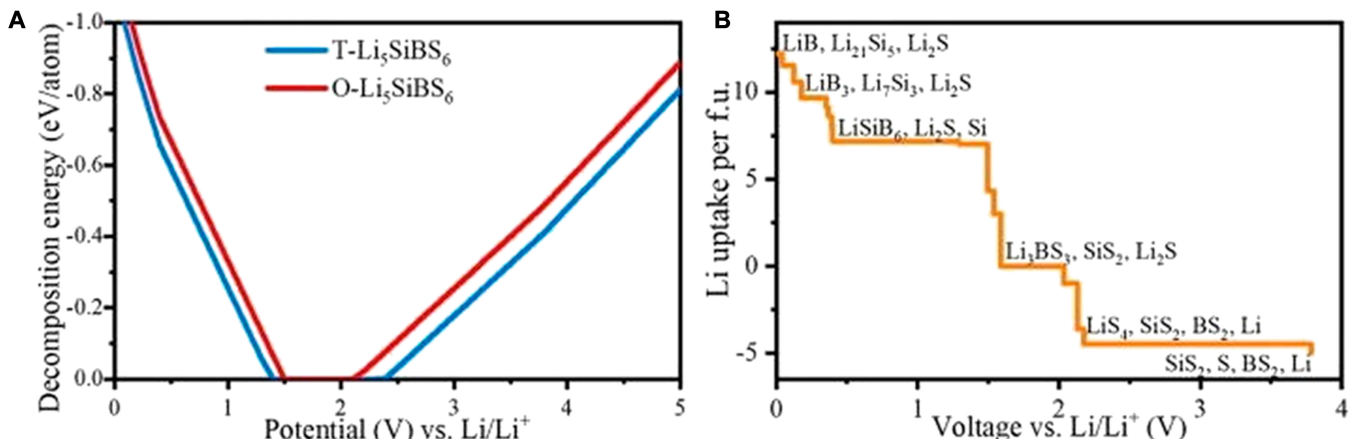


Fig.17.(A) Decomposition energy graph of the O-Li₅SiBS₆ and T-Li₅SiBS₆ solid electrolytes. (B) Decomposition pathway of the O-Li₅SiBS₆ and T-Li₅SiBS₆ solid electrolytes and their products. Reprinted with permission from [171]. Copyright 2022, AIP.

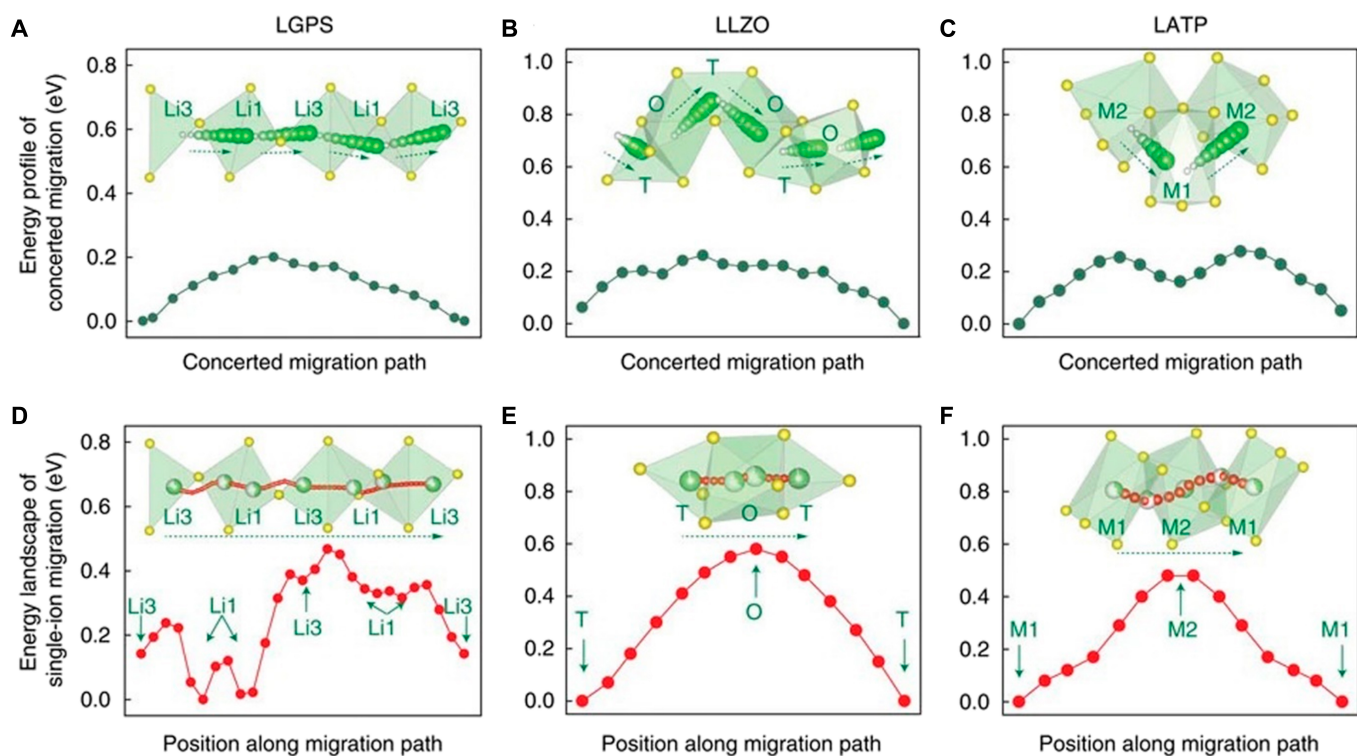


Fig.18. Migration energy barrier. (A) Li₁₀GeP₂S₁₂ (LGPS). (B) LLZO. (C) Li_{1.3}Al_{0.3}Ti_{1.7}(PO₄)₃ (LATP). (D to F) Migration energy landscape of the lithium-ion along the ion pathway and respective sites. Reproduced with permission from [146]. Copyright 2017, Springer Nature.

modifying lithium contents and site energetics by rational doping/substitutions. Moreover, they also found that such concerted mechanism can also work in duel ion systems [172].

Microscopic physical imaging and multiscale computation

Ion conduction behavior in electrolytes can be regulated by analyzing microscopic images of ion conduction characteristics. Microscopic images of ion conduction in an electrolyte can provide a clear picture of the kinetic behavior of the ions, which is vital to solid battery performance. The research progress of multiscale calculation methods such as BV [176], first-principles calculation, MD, finite element analysis, phase-field simulation, and ML [177] is applied to LIBs (lithium-ion batteries) and the combination of experimental and simulation methods is

observed. It can be helpful in presenting a comprehensive picture of ion transport on an electronic microscopic scale. In order to study ion transport in composite solid electrolytes through phase-field simulation (PFS), effective medium theory (EMT) is also used to extract the multiscale lithium ion migration mechanism and construct the theoretical design of a conductive framework [178,179]. PFS has emerged as a popular mesoscale material computing tool for studying phase transformations, phase transitions, and microstructure evolution. PFS has proven to be a critical tool in the energy sciences for optimizing and designing energy materials. PFS has a broad spectrum as time scale and length scale, bridging the gap between atomic simulations including DFT, Monte Carlo (MC), MD, and other macroscale range media approaches shown in Fig. 19A. Classically, the length scale for PFS can

vary between nanometers to meters, and the time scale from microseconds to days, correspondingly. A benefit of PFS is that it can access length scales analogous to the characterization techniques, for example, scanning electron microscopy (SEM) and transmission electron microscopy (TEM), enabling a straight evaluation between experimental findings and simulation predictions. The open-sourcing of PFS tools is a key component of allowing an open-source multiscale simulation framework represented in Fig. 19B. This framework will combine cutting-edge simulation tools such as DFT, ML, Calphad (phase diagram calculation), MC, and MD with PFS [180]. In multiscale simulation networks, atomic-level calculations can be achieved by using the DFT approach in order to determine the energy landscape and thermodynamic potential of the targeted materials or ion conductors. While MC and MD perform microscopic calculations and deliver microscopic characteristics such as diffusivity, it can be more expedited by ML [181].

Based on kinetics and thermodynamic regulations of microstructure evaluation and production, phase-field modeling has been used to create a wide range of microstructures. The structural properties of the matrix interface are key part for the microstructure morphology and interface ion conductivity. Hu et al. [179] established the phase-field model for the β -Li₃PS₄ solid electrolyte, which permits the creation of nanoporous microstructures with varying connectivity patterns and porosities based on the energy of the surface as well as depth, as proposed by the DFT calculation. A DFT calculated surface ionic conductivity of 3.14×10^{-3} S cm⁻¹ and an experimentally calculated bulk ionic conductivity of 8.93×10^{-7} S cm⁻¹ for β -Li₃PS₄ are shown in Fig. 20A and B. The created 1,600 3D microstructures presented various kinds of ionic connectivity pattern enabled microstructure as well as their respective $J_x(r)$ distributions (along the x axis, the applied electric field of 10 V/m) as shown in Fig. 20C to E. One to three microstructure rod-like fillers aligned along the x axis displayed a high ionic conductivity of σ_{xx} ($\sim 3.41 \times 10^{-4}$ S cm⁻¹), whereas a microstructure with rod-shaped fillers aligned along the y axis had a low ionic conductivity σ_{yy} ($\sim 1.96 \times 10^{-6}$ S cm⁻¹). The microscopic physical

image is more complicated to describe. There are numerous experimental methods for characterizing the ion transport image, such as nuclear magnetic resonance technology, solid-state magnetic resonance imaging, SEM, optical microscope, TEM, and neutron depth profiling technology [17,182]. As shown in Fig. 20F, the phase-field multiscale model is commonly used to propose the microstructure patterns as well as the effective characteristics of solid electrolytes.

A Practical Approach to Design a Superionic Conductor

Elucidating the fundamental structural principles that govern ionic migration in solid electrolytes will allow the discovery of new ionic conductors. Furthermore, enlightening the properties of ionic conductors and electrochemical stabilities are key factors in the advancement of solid electrolytes. The computational and experimental approaches for designing high-performance solid electrolytes are listed in Table 2. The strategies in designing superionic conductors are worth considering for the development of compositions based on multicomponent systems. The sulfide-based electrolytes are the foundation of pseudo-binary systems of Li₂S-P₂S₅. For example, among the numerous compositions along the Li₂S-P₂S₅ baseline, the Li₃PS₄ (75Li₂S-25P₂S₅) structure contains PS₄³⁻, and Li₇P₃S₁₁ (30Li₂S-30P₂S₅) is an equimolar combination of PS₄³⁻ and P₂S₇⁴⁻, both of which shows high Li-ion conductivities in the order of 10^{-3} to 10^{-2} S cm⁻¹.

In the previous section, the computation research progress of the ion conduction mechanism in superionic conductors has been overviewed in detail. The practical routes for designing of various solid electrolyte systems are thoroughly reviewed previously [10,183-191]. Here, in order to attain a better understanding of the experimental design of new superionic conductors, we summarize the development strategies for performance improvement, including synthesis methods, structural characterization, as well as chemical and electrochemical stabilities, in Fig. 21.

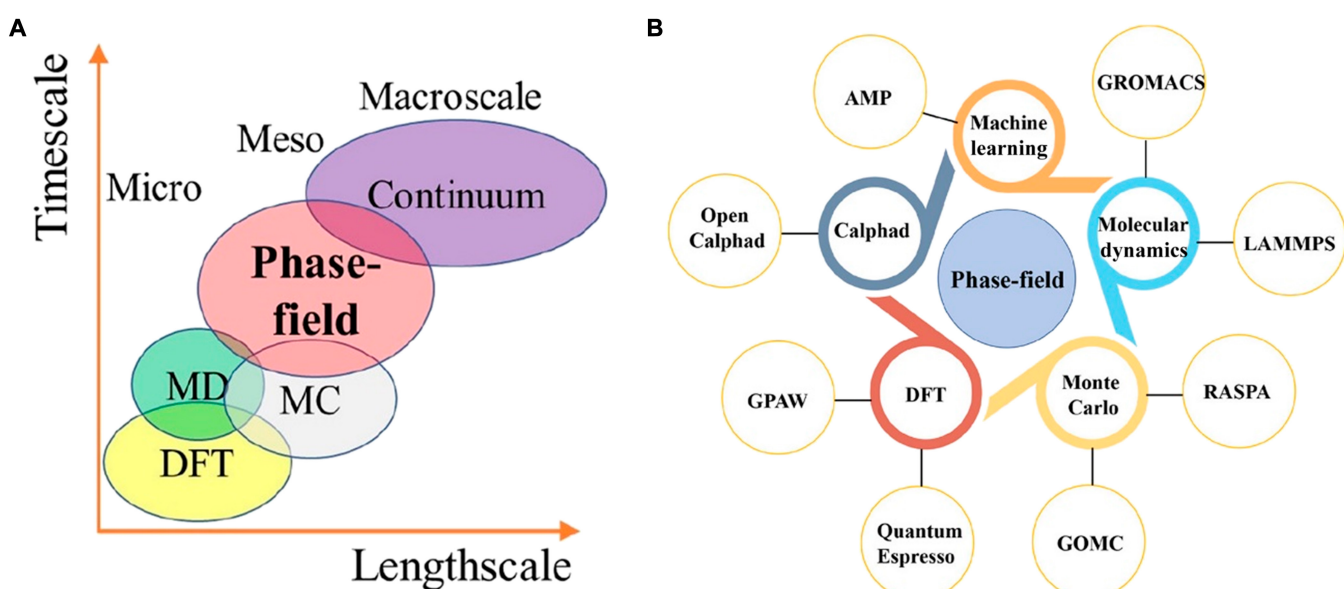


Fig.19.(A) Representation of the phase-field simulation (PFS) method. (B) Representation of the multiscale simulation approaches, which simulate the PFS with MC, MD, DFT, Calphad, and ML by open-source software. Adopted with permission from [180]. Copyright 2020, American Chemical Society.

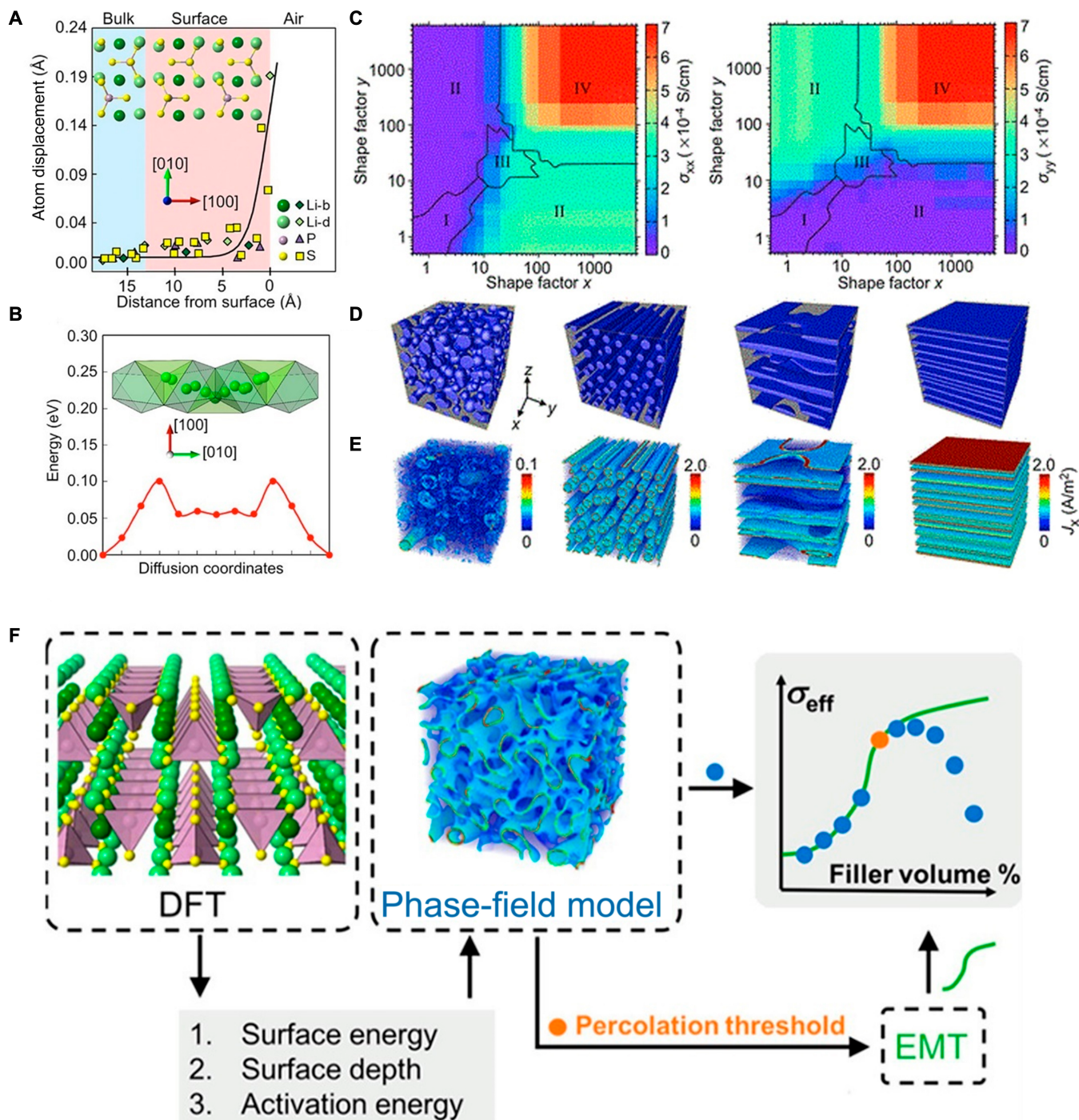


Fig.20. (A) Atom displacements with (100) surface normal of β -Li₃PS₄ materials attained by DFT simulation, where atom coordinates in a bulk β -Li₃PS₄ material as a reference. (B) Activation energy profile of the lithium-ion diffusion calculated by the NEB calculations. (C) Phase picture presentation of the phase connectivity of 1,600 two-phase microstructure designs produced by phase-field modeling, and the calculated ion conductivity of σ_{xx} as well as σ_{yy} . (D) Microstructure patterns produced by the different shape factors of $(x, y) = (1, 1), (3,000, 1), (20, 20)$, and $(3,000, 3,000)$ from left to right with the 0–3, 1–3, 2–3, and 2–2 kinds of connectivity, respectively. (E) Their respective equilibrium current densities $J_x(r)$ when an electric field of 10 V/m directed the x axis. (F) Schematic illustration of the calculation of the multiscale modeling. Adopted with permission from [179]. Copyright 2017, American Chemical Society.

Future Perspective

1. Defects and vacancies are crucial for migration. The location, type, and concentration of defects in the superionic conductor can significantly affect ion migration. These factors can be recognized and understood better by combining computational and experimental approaches (Fig. 22A). In

order to design new ionic conductors, it is also important to detect interaction and regularity both experimentally and theoretically between defects and mobile ions.

2. A finer crystalline structure with higher ion migration and a lower activation barrier needs to be identified. Several models have been anticipated to explain the

Table 2. The roadmap of experimental and computational approaches to characterize the properties of solid electrolyte from the atomic scale to microscale.

Properties of solid electrolytes	Experimental techniques	Computational approach
Ion migration (diffusion)	Nuclear magnetic resonances	NEB AIMD BV Monte Carlo simulation
Crystal local structure	XRD XPS XAS TEM	DFT calculation First-principles calculation MD, atomic-scale structure
Microscale structure	SEM/TEM HAADF SEM EDX	×
Composition OR 3D composition profile	XRD Neutron depth tomography Raman spectroscopy	×
Electrode/electrolyte interface	XPS ToF-SIMS HR-TEM/SEM Impedance spectroscopy CV Symmetric cell Asymmetric cell	First principle calculation Voltage profile (IDAM and DDAM) Phase equilibria Thermodynamic stability window MD DFT Chemical potential profile

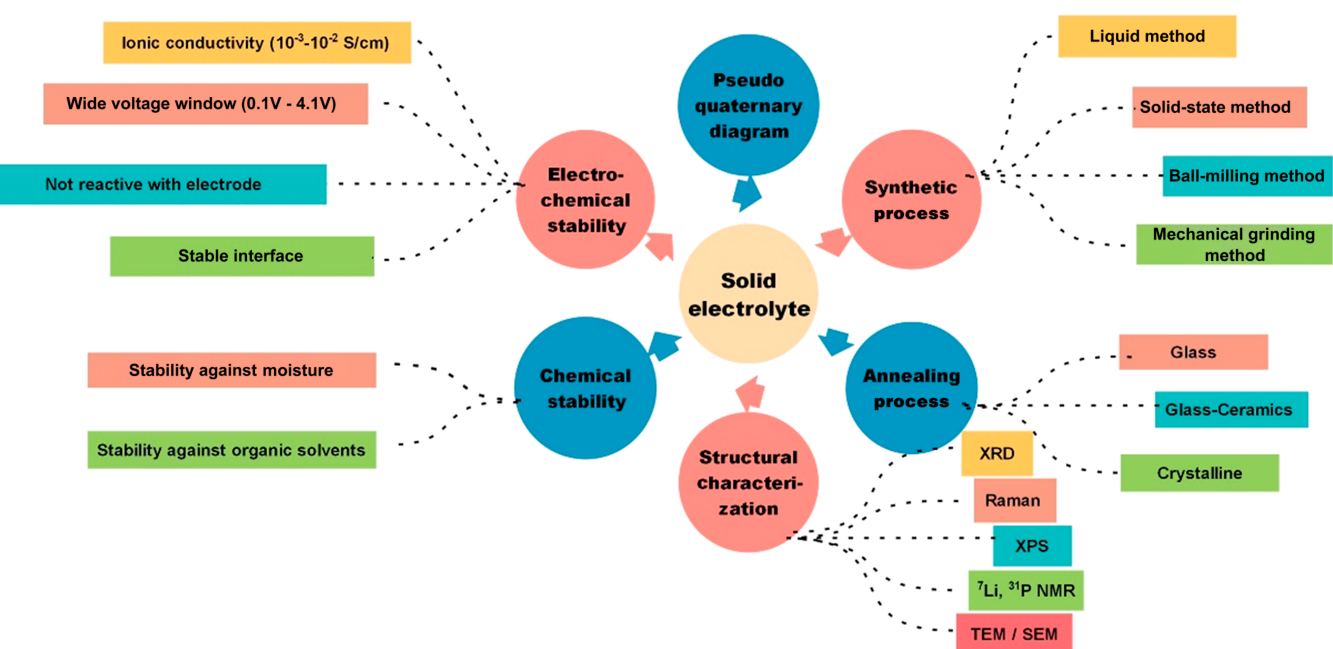


Fig. 21. The schematic diagram of steps for the experimental approach to explore the new superionic conductor.

migration of mobile ions such as Li^+ , Na^+ , and K^+ in crystalline structures, but there is still a deviation in experiments. A general and comprehensive model is required to construct the correlation between ion migration and lattice structure. First-principles and NEB calculations can be applied in this regard.

3. A concerted/coordinated ion migration mechanism displays unexpected increases in ionic conductivity of 2 to 5 orders of magnitude (Fig. 22B). Introducing new materials with concerted (cooperated) migration can increase the accessibility of superionic conductors for ASSBs.

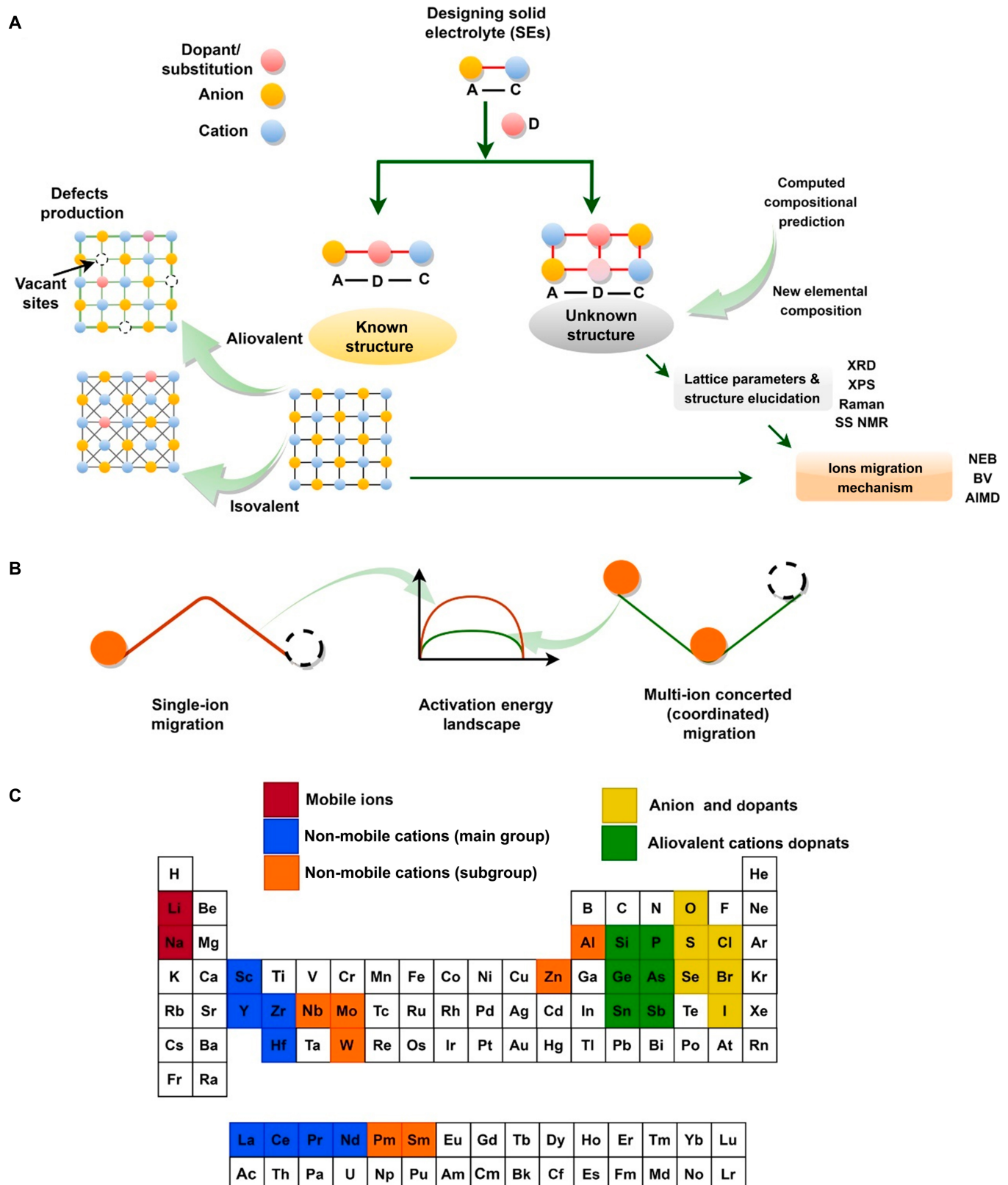


Fig.22.(A) Schematic diagram for designing the high-performance solid electrolytes. (B) A designed electrolyte enables multi-ion concerted migration mechanism. (C) Suggested dopant candidates for the ternary ionic conductors in the periodic table.

4. Compositional modifications can change the electrostatic interactions within the lattice, triggering the inductive effects, which also need to be explored and considered in a new ionic conductor. For example, in $\text{Li}_{10}\text{Ge}_{1-x}\text{Sn}_x\text{P}_2\text{S}_{12}$, Sn^{4+} leads to a decrease of electron density in the $\text{M}^{4+}-\text{S}^{2-}$ bonds, owing to its larger ionic radius and lower electronegativity than Ge^{4+} . With the addition of Sn content, the higher electron density on S^{2-} atoms results in stronger coulombic forces between S^{2-} and Li-ion, thereby enlarging the activation barrier and lowering the ionic motion [192]. The effects of the lattice softness suggest that coulombic interactions between Li-ion and lattice anion should be low in order to decrease the activation barrier.
5. Metal halides (MX) are good candidates as dopants to enhance the ionic conductivity of the sulfide SSEs (solid-state electrolytes), although they are ineffective at reducing moisture sensitivities. By cation doping in Fig. 22A to C, sulfide-based electrolytes have a much higher ionic conductivity than their oxide dopants. Moreover, metal dopants have a small effect on reducing the moisture sensitivity of sulfide-based SSE. In contrast, oxide-based dopants reduce the moisture sensitivity of sulfur-based solid electrolytes.
6. In ceramics or polymers, the mechanism of ion migration and how surface functionalities of inorganic additives interact with the polymer chain is still not entirely understood. Additionally, MD simulations have often yielded some primary findings in this context. Developing a clear image of interfaces and ion migration will likely require characterization approaches with atomic resolution and advanced theoretical calculations.
7. Designing of an outstanding superionic conductor with a flat energy landscape and high ionic conductivity at a wide range of temperatures is the first step toward attaining a solid-state battery with excellent safety. The engineering environment for full battery assembly largely depends on mechanical and physical characteristics, while electrode/electrolyte interfaces are also challenging. Real applications require additional parameters to be adjusted, such as power density, energy density, and battery cycle life.
8. SSEs are more expensive to manufacture than traditional liquid electrolytes. Various economic methods can be developed to maximize the commercial feasibility of SSE and increase opportunities. Liquid-phase synthesis is much more attractive for commercialization than solid-state synthesis because it eliminates complex procedures, enables mass production, and decreases reaction time. The thin layer of a solid electrolyte can limit inactive materials and production costs, improving the volumetric energy density as well as the gravimetric energy density of solid-state batteries. Tape casting and solution casting are common ways to prepare ceramics-in-polymer membranes.
9. Exploring new materials and structures that support fast ionic conductivity should be intensified. Combining high-throughput computing techniques with experiments will assist in identifying new ionic conductors.

Acknowledgments

Funding: This work was supported by the National Natural Science Foundation of China (grant nos. U1932205 and 52002197), the Key R&D Program of Shandong Province (grant no. 2021CXGC010401), and the “Taishan Scholars Program” (grant no. ts201712035). **Author contributions:** M.K.T. conceived the figures, analyzed the data, and wrote the manuscript. P.Z. and M.J. helped with editing of the paper. N.Z. and X.G. revised, edited, and supervised this project. **Competing interests:** The authors declare that they have no competing interests.

Data Availability

All data related to this study are present in the paper.

References

1. Feng X, Fang H, Wu N, Liu P, Jena P, Nanda J, Mitlin D. Review of modification strategies in emerging inorganic solid-state electrolytes for lithium, sodium, and potassium batteries. *Joule*. 2022;6(3):543–587.
2. Liu Q, Jiang L, Zheng P, Sun J, Liu C, Chai J, Li X, Zheng Y, Liu Z. Recent advances in stability issues of inorganic solid electrolytes and composite solid electrolytes for all-solid-state batteries. *Chem Rec*. 2022;22(10):e202200116.
3. Kong L, Li C, Jiang J, Pecht MG. Li-ion battery fire hazards and safety strategies. *Energies*. 2018;11(9):2191.
4. Chombo PV, Laoonual Y. A review of safety strategies of a Li-ion battery. *J Power Sources*. 2020;478:228649.
5. Chen R, Qu W, Guo X, Li L, Wu F. The pursuit of solid-state electrolytes for lithium batteries: From comprehensive insight to emerging horizons. *Mater Horiz*. 2016;3:487–516.
6. Liang X, Wang L, Wu X, Feng X, Wu Q, Sun Y, Xiang H, Wang J. Solid-state electrolytes for solid-state lithium-sulfur batteries: Comparisons, advances and prospects. *J Energy Chem*. 2022;73:370–386.
7. Zhao N, Khokhar W, Bi Z, Shi C, Guo X, Fan L-Z, Nan C-W. Solid garnet batteries. *Joule*. 2019;3:1190–1199.
8. Wu J, Liu S, Han F, Yao X, Wang C. Lithium/sulfide all-solid-state batteries using sulfide electrolytes. *Adv Mater*. 2021;33:2000751.
9. Zhang Q, Cao D, Ma Y, Natan A, Aurora P, Zhu H. Sulfide-based solid-state electrolytes: Synthesis, stability, and potential for all-solid-state batteries. *Adv Mater*. 2019;31:1901131.
10. Tufail MK, Ahmad N, Yang L, Zhou L, Naseer MA, Chen R, Yang W. A panoramic view of $\text{Li}_7\text{P}_3\text{S}_{11}$ solid electrolytes synthesis, structural aspects and practical challenges for all-solid-state lithium batteries. *Chin J Chem Eng*. 2021;39:16–36.
11. Khurram Tufail M, Ahmad N, Zhou L, Faheem M, Yang L, Chen R, Yang W. Insight on air-induced degradation mechanism of $\text{Li}_7\text{P}_3\text{S}_{11}$ to design a chemical-stable solid electrolyte with high Li_2S utilization in all-solid-state Li/S batteries. *Chem Eng J*. 2021;425:130535.
12. Tufail MK, Zhou L, Ahmad N, Chen R, Faheem M, Yang L, Yang W. A novel air-stable $\text{Li}_7\text{Sb}_{0.05}\text{P}_{2.95}\text{S}_{10.5}\text{I}_{0.5}$ superionic conductor glass-ceramics electrolyte for all-solid-state lithium-sulfur batteries. *Chem Eng J*. 2021;407:127149.
13. Guo J, Zhao X, Herisson De Beauvoir T, Seo J-H, Berbano SS, Baker AL, Azina C, Randall CA. Recent progress in

- applications of the cold sintering process for ceramic-polymer composites. *Adv Funct Mater.* 2018;28:1801724.
14. Kanimozhi G, Naresh N, Kumar H, Satyanarayana N. Review on the recent progress in the nanocomposite polymer electrolytes on the performance of lithium-ion batteries. *Int J Energy Res.* 2022;46:7137–7174.
 15. Bi Z, Huang W, Mu S, Sun W, Zhao N, Guo X. Dual-interface reinforced flexible solid garnet batteries enabled by in-situ solidified gel polymer electrolytes. *Nano Energy.* 2021;90:106498.
 16. Wu J, Chen L, Song T, Zou Z, Gao J, Zhang W, Shi S. A review on structural characteristics, lithium ion diffusion behavior and temperature dependence of conductivity in perovskite-type solid electrolyte $\text{Li}_{3x}\text{La}_{2/3-x}\text{TiO}_3$. *Funct Mater Lett.* 2017;10:1730002.
 17. Gao J, Zhao Y-S, Shi S-Q, Li H. Lithium-ion transport in inorganic solid state electrolyte. *Chin Phys B.* 2016;25:018211.
 18. Sendek AD, Yang Q, Cubuk ED, Duerloo K-AN, Cui Y, Reed EJ. Holistic computational structure screening of more than 12 000 candidates for solid lithium-ion conductor materials. *Energy Environ Sci.* 2017;10:306–320.
 19. Kahle L, Marcolongo A, Marzari N. High-throughput computational screening for solid-state Li-ion conductors. *Energy Environ Sci.* 2020;13:928–948.
 20. Avdeev M, Sale M, Adams S, Rao RP. Screening of the alkali-metal ion containing materials from the Inorganic Crystal Structure Database (ICSD) for high ionic conductivity pathways using the bond valence method. *Solid State Ionics.* 2012;225:43–46.
 21. Muy S, Voss J, Schlem R, Koerver R, Sedlmaier SJ, Maglia F, Lamp P, Zeier WG, Shao-Horn Y. High-throughput screening of solid-state li-ion conductors using lattice-dynamics descriptors. *iScience.* 2019;16:270–282.
 22. Xiao R, Li H, Chen L. High-throughput design and optimization of fast lithium ion conductors by the combination of bond-valence method and density functional theory. *Sci Rep.* 2015;5:14227.
 23. Meutzner F, Nestler T, Zschornak M, Canepa P, Gautam GS, Leoni S, Adams S, Leisegang T, Blatov VA, Meyer DC. Computational analysis and identification of battery materials. *Phys Sci Rev.* 2019;4:20180044.
 24. Lim M-S, Jhi S-H. First-principles study of lithium-ion diffusion in β - Li_3PS_4 for solid-state electrolytes. *Curr Appl Phys.* 2018;18(5):541–545.
 25. Mahmood A, Irfan A, Ahmad F. Quantum chemical analysis and molecular dynamics simulations to study the impact of electron-deficient substituents on electronic behavior of small molecule acceptors. *Comput Theor Chem.* 2021;1204:113387.
 26. Xu Z, Xia Y. Progress, challenges and perspectives of computational studies on glassy superionic conductors for solid-state batteries. *J Mater Chem A.* 2022;10:11854–11880.
 27. Mahmood A, Abdullah MI, Nazar MF. Quantum chemical designing of novel organic non-linear optical compounds. *Bull Korean Chem Soc.* 2014;35(5):1391–1396.
 28. Mahmood A, Saqib M, Ali M, Abdullah MI, Khalid B. Theoretical investigation for the designing of novel antioxidants. *Can J Chem.* 2012;91:126–130.
 29. Nolan AM, Zhu Y, He X, Bai Q, Mo Y. Computation-accelerated design of materials and interfaces for all-solid-state lithium-ion batteries. *Joule.* 2018;2:2016–2046.
 30. Mahmood A, HussainTahir M, Irfan A, Khalid B, Al-Sehemi AG. Computational designing of triphenylamine dyes with broad and red-shifted absorption spectra for dye-sensitized solar cells using multi-thiophene rings in π -spacer. *Bull Korean Chem Soc.* 2015;36:2615–2620.
 31. Fujimura K, Seko A, Koyama Y, Kuwabara A, Kishida I, Shitara K, Fisher CAJ, Moriwake H, Tanaka I. Accelerated materials design of lithium superionic conductors based on first-principles calculations and machine learning algorithms. *Adv Energy Mater.* 2013;3:980–985.
 32. Zhang B, Tan R, Yang L, Zheng J, Zhang K, Mo S, Lin Z, Pan F. Mechanisms and properties of ion-transport in inorganic solid electrolytes. *Energy Storage Mater.* 2018;10:139–159.
 33. Han J, Zhu J, Li Y, Yu X, Wang S, Wu G, Xie H, Vogel SC, Izumi F, Momma K, et al. Experimental visualization of lithium conduction pathways in garnet-type $\text{Li}_7\text{La}_3\text{Zr}_2\text{O}_{12}$. *Chem Commun.* 2012;48:9840–9842.
 34. KC S, Longo RC, Xiong K, Cho K. Point defects in garnet-type solid electrolyte ($\text{c-Li}_3\text{La}_3\text{Zr}_2\text{O}_{12}$) for Li-ion batteries. *Solid State Ionics.* 2014;261:100–105.
 35. Chen C, Du J. Lithium ion diffusion mechanism in lithium lanthanum titanate solid-state electrolytes from atomistic simulations. *J Am Ceram Soc.* 2015;98:534–542.
 36. Zhang Z, Shao Y, Lotsch B, Hu Y-S, Li H, Janek J, Nazar LF, Nan C-W, Maier J, Armand M, et al. New horizons for inorganic solid state ion conductors. *Energy Environ Sci.* 2018;11:1945–1976.
 37. Sun Y, Guan P, Liu Y, Xu H, Li S, Chu D. Recent progress in lithium lanthanum titanate electrolyte towards all solid-state lithium ion secondary battery. *Crit Rev Solid State Mater Sci.* 2019;44:265–282.
 38. Zhan X, Lai S, Gobet MP, Greenbaum SG, Shirpour M. Defect chemistry and electrical properties of garnet-type $\text{Li}_7\text{La}_3\text{Zr}_2\text{O}_{12}$. *Phys Chem Chem Phys.* 2018;20:1447–1459.
 39. Lang B, Ziebarth B, Elsässer C. Lithium ion conduction in $\text{LiTi}_2(\text{PO}_4)_3$ and related compounds based on the NASICON structure: A first-principles study. *Chem Mater.* 2015;27(14):5040–5048.
 40. Lu X, Wang S, Xiao R, Shi S, Li H, Chen L. First-principles insight into the structural fundamental of super ionic conducting in NASICON $\text{MTi}_2(\text{PO}_4)_3$ ($\text{M} = \text{Li, Na}$) materials for rechargeable batteries. *Nano Energy.* 2017;41:626–633.
 41. Arbi K, Rojo JM, Sanz J. Lithium mobility in titanium based Nasicon $\text{Li}_{1+x}\text{Ti}_{2-x}\text{Al}_x(\text{PO}_4)_3$ and $\text{LiTi}_{2-x}\text{Zr}_x(\text{PO}_4)_3$ materials followed by NMR and impedance spectroscopy. *J Eur Ceram Soc.* 2007;27(13–15):4215–4218.
 42. Arjmandi HR, Grieshammer S. Defect formation and migration in Nasicon $\text{Li}_{1+x}\text{Al}_x\text{Ti}_{2-x}(\text{PO}_4)_3$. *Phys Chem Chem Phys.* 2019;21:24232–24238.
 43. Oka M, Kamisaka H, Fukumura T, Hasegawa T. Interstitial diffusion of fluoride ions in LaOF by DFT-based first-principles calculations. *Comput Mater Sci.* 2019;167:92–99.
 44. Deng Y, Eames C, Chotard J-N, Lalère F, Seznec V, Emge S, Pecher O, Grey CP, Masquelier C, Islam MS. Structural and mechanistic insights into fast lithium-ion conduction in Li_4SiO_4 – Li_3PO_4 solid electrolytes. *J Am Chem Soc.* 2015;137(28):9136–9145.
 45. Sebastian L, Jayashree RS, Gopalakrishnan J. Probing the mobility of lithium in LISICON: Li^+/H^+ exchange studies in $\text{Li}_2\text{ZnGeO}_4$ and $\text{Li}_{2+2x}\text{Zn}_{1-x}\text{GeO}_4$. *J Mater Chem.* 2003;13:1400–1405.
 46. Long L, Wang S, Xiao M, Meng Y. Polymer electrolytes for lithium polymer batteries. *J Mater Chem A.* 2016;4:10038–10069.

47. Berthier C, Gorecki W, Minier M, Armand MB, Chabagno JM, Rigaud P. Microscopic investigation of ionic conductivity in alkali metal salts-poly(ethylene oxide) adducts. *Solid State Ionics*. 1983;11:91–95.
48. Blessings of mixed neutrinos. *Nature*. 2001;412:1.
49. Henderson WA, Brooks NR, Young VG. Single-crystal structures of polymer electrolytes. *J Am Chem Soc*. 2003;125:12098–12099.
50. Johansson P, Tegenfeldt J, Lindgren J. Modelling amorphous lithium salt-PEO polymer electrolytes: Ab initio calculations of lithium ion-tetra-, penta- and hexaglyme complexes. *Polymer*. 1999;40(15):4399–4406.
51. Borodin O, Smith GD. Molecular dynamics simulations of poly(ethylene oxide)/LiI melts. 1. Structural and conformational properties. *Macromolecules*. 1998;31:8396–8406.
52. Stoeva Z, Martin-Litas I, Staunton E, Andreev YG, Bruce PG. Ionic conductivity in the crystalline polymer electrolytes $\text{PEO}_6\text{-LiXF}_6$, $X = \text{P, As, Sb}$. *J Am Chem Soc*. 2003;125(15):4619–4626.
53. Gadjourova Z, Andreev YG, Tunstall DP, Bruce PG. Ionic conductivity in crystalline polymer electrolytes. *Nature*. 2001;412:520–523.
54. Ratner MA, Johansson P, Shriver DF. Polymer electrolytes: Ionic transport mechanisms and relaxation coupling. *MRS Bull*. 2000;25:31–37.
55. Islam MS, Driscoll DJ, Fisher CAJ, Slater PR. Atomic-scale investigation of defects, dopants, and lithium transport in the LiFePO_4 olivine-type battery material. *Chem Mater*. 2005;17:5085–5092.
56. Jónsson H, Mills G, Jacobsen KW. Nudged elastic band method for finding minimum energy paths of transitions. In: *Classical and quantum dynamics in condensed phase simulations*. Singapore: World Scientific; 1998; p. 385–404.
57. Wang Y, Richards WD, Ong SP, Miara LJ, Kim JC, Mo Y, Ceder G. Design principles for solid-state lithium superionic conductors. *Nat Mater*. 2015;14:1026–1031.
58. Dietrich C, Sadowski M, Siculo S, Weber DA, Sedlmaier SJ, Weldert KS, Indris S, Albe K, Janek J, Zeier WG. Local structural investigations, defect formation, and ionic conductivity of the lithium ionic conductor $\text{Li}_4\text{P}_2\text{S}_6$. *Chem Mater*. 2016;28:8764–8773.
59. Du YA, Holzwarth NAW. Li ion diffusion mechanisms in the crystalline electrolyte $\gamma\text{-Li}_3\text{PO}_4$. *J Electrochem Soc*. 2007;154:A999.
60. Du YA, Holzwarth NAW. Mechanisms of Li^+ diffusion in crystalline γ - and β - Li_3PO_4 electrolytes from first principles. *Phys Rev B*. 2007;76:174302.
61. Ivanov-Shitz AK, Kireev VV, Mel'nikov OK, Demianets LN. Growth and ionic conductivity of $\gamma\text{-Li}_3\text{PO}_4$. *Crystallogr Rep*. 2001;46:864–867.
62. Huggins RA. Recent results on lithium ion conductors. *Electrochim Acta*. 1977;22:773–781.
63. Wang B, Chakoumakos BC, Sales BC, Kwak BS, Bates JB. Synthesis, crystal structure, and ionic conductivity of a polycrystalline lithium phosphorus oxynitride with the $\gamma\text{-Li}_3\text{PO}_4$ structure. *J Solid State Chem*. 1995;115:313–323.
64. Al-Qawasmeh A, Howard J, Holzwarth NAW. Li_4SnS_4 and Li_4SnSe_4 : Simulations of their structure and electrolyte properties. *J Electrochem Soc*. 2017;164(1):A6386–A6394.
65. Al-Qawasmeh A, Holzwarth NAW. Computational study of Li ion electrolytes composed of Li_3AsS_4 alloyed with Li_4GeS_4 . *J Electrochem Soc*. 2016;163:A2079–A2088.
66. Xu Z, Chen R, Zhu H. A Li_2CuPS_4 superionic conductor: A new sulfide-based solid-state electrolyte. *J Mater Chem A*. 2019;7:12645–12653.
67. Kamaya N, Homma K, Yamakawa Y, Hirayama M, Kanno R, Yonemura M, Kamiyama T, Kato Y, Hama S, Kawamoto K. A lithium superionic conductor. *Nat Mater*. 2011;10:682–686.
68. Mo Y, Ong SP, Ceder G. First principles study of the $\text{Li}_{10}\text{GeP}_2\text{S}_{12}$ lithium super ionic conductor material. *Chem Mater*. 2012;24:15–17.
69. Kaup K, Bishop K, Assoud A, Liu J, Nazar LF. Fast ion-conducting thioboracite with a perovskite topology and argyrodite-like lithium substructure. *J Am Chem Soc*. 2021;143(18):6952–6961.
70. Chu IH, Nguyen H, Hy S, Lin YC, Wang Z, Xu Z, Deng Z, Meng YS, Ong SP. Insights into the performance limits of the $\text{Li}_7\text{P}_3\text{S}_{11}$ superionic conductor: A combined first-principles and experimental study. *ACS Appl Mater Interfaces*. 2016;8:7843–7853.
71. Nam K, Chun H, Hwang J, Han B. First-principles design of highly functional sulfide electrolyte of $\text{Li}_{10-x}\text{SnP}_2\text{S}_{12-x}\text{Cl}_x$ for all solid-state Li-ion battery applications. *ACS Sustain Chem Eng*. 2020;8:3321–3327.
72. Liu B, Hu Q, Gao T, Liao P, Wen Y, Lu Z, Yang J, Shi S, Zhang W. Computational insights into the ionic transport mechanism and interfacial stability of the Li_2OHCl solid-state electrolyte. *J Mater*. 2022;8(1):59–67.
73. Chun H, Nam K, Hong SJ, Kang J, Han B. Design of a unique anion framework in halospinels for outstanding performance of all solid-state Li-ion batteries: First-principles approach. *J Mater Chem A*. 2021;9:15605–15612.
74. Zhu Y, He X, Mo Y. First principles study on electrochemical and chemical stability of solid electrolyte-electrode interfaces in all-solid-state Li-ion batteries. *J Mater Chem A*. 2016;4:3253–3266.
75. Richards WD, Miara LJ, Wang Y, Kim JC, Ceder G. Interface stability in solid-state batteries. *Chem Mater*. 2016;28:266–273.
76. Richards WD, Tsujimura T, Miara LJ, Wang Y, Kim JC, Ong SP, Uechi I, Suzuki N, Ceder G. Design and synthesis of the superionic conductor $\text{Na}_{10}\text{SnP}_2\text{S}_{12}$. *Nat Commun*. 2016;7:11009.
77. Ong SP, Mo Y, Richards WD, Miara L, Lee HS, Ceder G. Phase stability, electrochemical stability and ionic conductivity of the $\text{Li}_{10\pm 1}\text{MP}_2\text{X}_{12}$ ($\text{M} = \text{Ge, Si, Sn, Al or P, and X = O, S or Se}$) family of superionic conductors. *Energy Environ Sci*. 2013;6:148–156.
78. Holzwarth NAW, Lepley ND, Du YA. Computer modeling of lithium phosphate and thiophosphate electrolyte materials. *J Power Sources*. 2011;196:6870–6876.
79. Adams S, Rao RP. High power lithium ion battery materials by computational design. *Phys Status Solidi A*. 2011;208:1746–1753.
80. Adams S, Rao RP. Transport pathways for mobile ions in disordered solids from the analysis of energy-scaled bond-valence mismatch landscapes. *Phys Chem Chem Phys*. 2009;11:3210–3216.
81. Mazza D, Ronchetti S, Bohnké O, Duroy H, Fourquet JL. Modeling Li-ion conductivity in fast ionic conductor $\text{La}_{2/3-x}\text{Li}_3x\text{TiO}_3$. *Solid State Ionics*. 2002;149:81–88.
82. Brese NE, O'Keeffe M. Bond-valence parameters for solids. *Acta Crystallogr B*. 1991;47:192–197.
83. Inaguma Y, Katsumata T, Itoh M, Morii Y, Tsurui T. Structural investigations of migration pathways in lithium

- ion-conducting $\text{La}_{2/3-x}\text{Li}_{3x}\text{TiO}_3$ perovskites. *Solid State Ionics*. 2006;177(35-36):3037–3044.
84. Adams S, Rao RP. Ion transport and phase transition in $\text{Li}_{7-x}\text{La}_3(\text{Zr}_{2-x}\text{M}_x)\text{O}_{12}$ ($\text{M} = \text{Ta}^{5+}, \text{Nb}^{5+}$, $x = 0, 0.25$). *J Mater Chem*. 2012;22:1426–1434.
 85. Filsø MØ, Turner MJ, Gibbs GV, Adams S, Spackman MA, Iversen BB. Visualizing lithium-ion migration pathways in battery materials. *Chemistry*. 2013;19:15535–15544.
 86. Liu G, Xie D, Wang X, Yao X, Chen S, Xiao R, Li H, Xu X. High air-stability and superior lithium ion conduction of $\text{Li}_{3+3x}\text{P}_{1-x}\text{Zn}_x\text{S}_{4-x}\text{O}_x$ by aliovalent substitution of ZnO for all-solid-state lithium batteries. *Energy Storage Mater*. 2019;17:266–274.
 87. He B, Chi S, Ye A, Mi P, Zhang L, Pu B, Zou Z, Ran Y, Zhao Q, Wang D, et al. High-throughput screening platform for solid electrolytes combining hierarchical ion-transport prediction algorithms. *Sci Data*. 2020;7:151.
 88. Zhang L, He B, Zhao Q, Zou Z, Chi S, Mi P, Ye A, Li Y, Wang D, Avdeev M, et al. A database of ionic transport characteristics for over 29 000 inorganic compounds. *Adv Funct Mater*. 2020;30(35):2003087.
 89. Goodenough JB, Kim Y. Challenges for rechargeable Li batteries. *Chem Mater*. 2010;22:587–603.
 90. Zhu Y, Gonzalez-Rosillo JC, Balaish M, Hood ZD, Kim KJ, Rupp JLM. Lithium-film ceramics for solid-state lithionic devices. *Nat Rev Mater*. 2021;6:313–331.
 91. Shannon RD, Taylor BE, English AD, Berzins T, New Li solid electrolytes. In: *International Symposium on Solid Ionic and Ionic-Electronic Conductors*. Rome: Elsevier; 1977; p. 783–796.
 92. Rodger AR, Kuwano J, West AR. Li^+ ion conducting γ solid solutions in the systems $\text{Li}_4\text{XO}_4\text{-Li}_3\text{YO}_4$: $\text{X} = \text{Si, Ge, Ti}$; $\text{Y} = \text{P}$, as, V ; $\text{Li}_4\text{XO}_4\text{-LiZO}_2$: $\text{Z} = \text{Al, Ga, Cr}$ and $\text{Li}_4\text{GeO}_4\text{-Li}_2\text{CaGeO}_4$. *Solid State Ionics*. 1985;15:185–198.
 93. Bates JB, Dudney NJ, Gruzalski GR, Zuhra RA, Choudhury A, Luck CF, Robertson JD. Electrical properties of amorphous lithium electrolyte thin films. *Solid State Ionics*. 1992;53:647–654.
 94. Lacicita V, Artrith N, Ceder G. Structural and compositional factors that control the Li-ion conductivity in LiPON electrolytes. *Chem Mater*. 2018;30:7077–7090.
 95. Wolfenstine J, Allen JL, Sumner J, Sakamoto J. Electrical and mechanical properties of hot-pressed versus sintered $\text{LiTi}_2(\text{PO}_4)_3$. *Solid State Ionics*. 2009;180(14–16):961–967.
 96. Su Y, Falgenhauer J, Polity A, Leichtweiß T, Kronenberger A, Obel J, Zhou S, Schlettwein D, Janek J, Meyer BK. LiPON thin films with high nitrogen content for application in lithium batteries and electrochromic devices prepared by RF magnetron sputtering. *Solid State Ionics*. 2015;282:63–69.
 97. Epp V, Ma Q, Hammer E-M, Tietz F, Wilkening M. Very fast bulk Li ion diffusivity in crystalline $\text{Li}_{1.5}\text{Al}_{0.5}\text{Ti}_{1.5}(\text{PO}_4)_3$ as seen using NMR relaxometry. *Phys Chem Chem Phys*. 2015;17:32115–32121.
 98. Wang S, Ding Y, Zhou G, Yu G, Manthiram A. Durability of the $\text{Li}_{1+x}\text{Ti}_{2-x}\text{Al}_x(\text{PO}_4)_3$ solid electrolyte in lithium–sulfur batteries. *ACS Energy Lett*. 2016;1:1080–1085.
 99. Takahashi T, Iwahara H. Ionic conduction in perovskite-type oxide solid solution and its application to the solid electrolyte fuel cell. *Energy Convers*. 1971;11(3):105–111.
 100. Bohnke O. The fast lithium-ion conducting oxides $\text{Li}_{3x}\text{La}_{2/3-x}\text{-TiO}_3$ from fundamentals to application. *Solid State Ionics*. 2008;179(1–6):9–15.
 101. Bohnke O, Emery J, Fourquet J-L. Anomalies in Li^+ ion dynamics observed by impedance spectroscopy and 7Li NMR in the perovskite fast ion conductor $(\text{Li}_{3x}\text{La}_{2/3-x}\text{□}_{1/3-2x})\text{TiO}_3$. *Solid State Ionics*. 2003;158(1–2):119–132.
 102. Stramare S, Thangadurai V, Weppner W. Lithium lanthanum titanates: A review. *Chem Mater*. 2003;15(21):3974–3990.
 103. Lu J, Li Y. Perovskite-type Li-ion solid electrolytes: A review. *J Mater Sci Mater Electron*. 2021;32(8):9736–9754.
 104. Emery J, Buzare JY, Bohnke O, Fourquet JL. Lithium-7 NMR and ionic conductivity studies of lanthanum lithium titanate electrolytes. *Solid State Ionics*. 1997;99(1–2):41–51.
 105. Harada Y, Ishigaki T, Kawai H, Kuwano J. Lithium ion conductivity of polycrystalline perovskite $\text{La}_{0.67-x}\text{Li}_{3x}\text{TiO}_3$ with ordered and disordered arrangements of the A-site ions. *Solid State Ionics*. 1998;108(1–4):407–413.
 106. Murugan R, Thangadurai V, Weppner W. Fast lithium ion conduction in garnet-type $\text{Li}_5\text{La}_3\text{Zr}_2\text{O}_{12}$. *Angew Chem Int Ed*. 2007;46(41):7778–7781.
 107. Thangadurai V, Kaack H, Weppner W. Novel fast lithium ion conduction in garnet-type $\text{Li}_5\text{La}_3\text{M}_2\text{O}_{12}$ ($\text{M} = \text{Nb, Ta}$). *J Am Ceram Soc*. 2003;86(3):437–440.
 108. Xie H, Alonso JA, Li Y, Fernández-Díaz MT, Goodenough JB. Lithium distribution in aluminum-free cubic $\text{Li}_5\text{La}_3\text{Zr}_2\text{O}_{12}$. *Chem Mater*. 2011;23(16):3587–3589.
 109. Li Y, Han J-T, Wang C-A, Vogel SC, Xie H, Xu M, Goodenough JB. Ionic distribution and conductivity in lithium garnet $\text{Li}_7\text{La}_3\text{Zr}_2\text{O}_{12}$. *J Power Sources*. 2012;209:278–281.
 110. Buschmann H, Dölle J, Berendts S, Kuhn A, Bottke P, Wilkening M, Heitjans P, Senyshyn A, Ehrenberg H, Lotnyk A, et al. Structure and dynamics of the fast lithium ion conductor “ $\text{Li}_7\text{La}_3\text{Zr}_2\text{O}_{12}$ ”. *Phys Chem Chem Phys*. 2011;13(43):19378–19392.
 111. Geiger CA, Alekseev E, Lazic B, Fisch M, Armbruster T, Langner R, Fechtelkord M, Kim N, Pettke T, Weppner W. Crystal chemistry and stability of “ $\text{Li}_7\text{La}_3\text{Zr}_2\text{O}_{12}$ ” garnet: A fast lithium-ion conductor. *Inorg Chem*. 2011;50(3):1089–1097.
 112. Aktaş S, Özendir OM, Eker YR, Ateş S, Atav Ü, Çelik G, Klysubun W. Study of the local structure and electrical properties of gallium substituted LLZO electrolyte materials. *J Alloys Compd*. 2019;792:279–285.
 113. Awaka J, Takashima A, Kataoka K, Kijima N, Idemoto Y, Akimoto J. Crystal structure of fast lithium-ion-conducting cubic $\text{Li}_7\text{La}_3\text{Zr}_2\text{O}_{12}$. *Chem Lett*. 2010;40(1):60–62.
 114. Song S, Chen B, Ruan Y, Sun J, Yu L, Wang Y, Thokchom J. Gd-doped $\text{Li}_5\text{La}_3\text{Zr}_2\text{O}_{12}$ garnet-type solid electrolytes for all-solid-state Li-Ion batteries. *Electrochim Acta*. 2018;270:501–508.
 115. Naseer MA, Tufail MK, Ali A, Hussain S, Khan U, Jin H. Review on computational-assisted to experimental synthesis, interfacial perspectives of garnet-solid electrolytes for all-solid-state lithium batteries, journal of the electrochemical Society. 2021;168(6):60529.
 116. Aguadero A, Aguesse F, Bernuy-López C, Manalastas WW Jr, del Amo JML, Kilner JA. Improvement of transport properties in Li-conducting ceramic oxides. *Electrochim Soc Meet Abstr* 2015:503.
 117. Lotsch BV, Maier J. Relevance of solid electrolytes for lithium-based batteries: A realistic view. *J Electroceram*. 2017;38(2):128–141.
 118. Seino Y, Ota T, Takada K, Hayashi A, Tatsumisago M. A sulphide lithium super ion conductor is superior to liquid ion conductors for use in rechargeable batteries. *Energy Environ Sci*. 2014;7(2):627–631.
 119. Kato Y, Hori S, Saito T, Suzuki K, Hirayama M, Mitsui A, Yonemura M, Iba H, Kanno R. High-power all-solid-state

- batteries using sulfide superionic conductors. *Nat Energy*. 2016;1(4):16030.
120. Murayama M, Kanno R, Irie M, Ito S, Hata T, Sonoyama N, Kawamoto Y. Synthesis of new lithium ionic conductor thio-LISICON—lithium silicon sulfides system. *J Solid State Chem*. 2002;168(1):140–148.
 121. Bachman JC, Muy S, Grimaud A, Chang H-H, Pour N, Lux SF, Paschos O, Maglia F, Lupart S, Lamp P, et al. Inorganic solid-state electrolytes for lithium batteries: Mechanisms and properties governing ion conduction. *Chem Rev*. 2016;116(1):140–162.
 122. Murayama M, Kanno R, Kawamoto Y, Kamiyama T. Structure of the thio-LISICON, Li_4GeS_4 . *Solid State Ionics*. 2002;154–155:789–794.
 123. Kong S-T, Deiseroth H-J, Maier J, Nickel V, Weichert K, Reiner C. $\text{Li}_6\text{PO}_5\text{Br}$ and $\text{Li}_6\text{PO}_5\text{Cl}$: The first lithium-oxide-argyrodites. *Z Anorg Allg Chem*. 2010;636(11):1920–1924.
 124. Boulineau S, Courty M, Tarascon J-M, Viallet V. Mechanochemical synthesis of Li-argyrodite $\text{Li}_6\text{PS}_5\text{X}$ ($\text{X} = \text{Cl}, \text{Br}, \text{I}$) as sulfur-based solid electrolytes for all solid state batteries application. *Solid State Ionics*. 2012;221:1–5.
 125. Tachez M, Malugani J-P, Mercier R, Robert G. Ionic conductivity of and phase transition in lithium thiophosphate Li_3PS_4 . *Solid State Ionics*. 1984;14(3):181–185.
 126. Lepley ND, Holzwarth NAW, Du YA. Structures, Li^+ mobilities, and interfacial properties of solid electrolytes Li_3PS_4 and Li_3PO_4 from first principles. *Phys Rev B*. 2013;88(10):104103.
 127. Pan L, Zhang L, Ye A, Chi S, Zou Z, He B, Chen L, Zhao Q, Wang D, Shi S. Revisiting the ionic diffusion mechanism in Li_3PS_4 via the joint usage of geometrical analysis and bond valence method. *J Mater*. 2019;5(4):688–695.
 128. Liu Z, Fu W, Payzant EA, Yu X, Wu Z, Dudney NJ, Kiggans J, Hong K, Rondinone AJ, Liang C. Anomalous high ionic conductivity of nanoporous β -Li₃PS₄. *J Am Chem Soc*. 2013;135(3):975–978.
 129. Adams S, Prasada Rao R. Structural requirements for fast lithium ion migration in $\text{Li}_{10}\text{GeP}_2\text{S}_{12}$. *J Mater Chem*. 2012;22(16):7687–7691.
 130. Bron P, Johansson S, Zick K, Schmedt auf der Günne J, Dehnen S, Roling B. $\text{Li}_{10}\text{SnP}_2\text{S}_{12}$: An affordable lithium superionic conductor. *J Am Chem Soc*. 2013;135(42):15694–15697.
 131. Weisbach A. *Argyrodit. ein neues Silbererz*; 1886.
 132. Gagor A, Pietraszko A, Kaynts D. Structural aspects of fast copper mobility in $\text{Cu}_6\text{PS}_5\text{Cl}$ —The best solid electrolyte from $\text{Cu}_6\text{PS}_5\text{X}$ series. *J Solid State Chem*. 2008;181(4):777–782.
 133. Deiseroth HJ, Kong ST, Eckert H, Vannahme J, Reiner C, Zaiß T, Schlosser M. $\text{Li}_6\text{PS}_5\text{X}$: A class of crystalline Li-rich solids with an unusually high Li^+ mobility. *Angew Chem Int Ed*. 2008;47(4):755–758.
 134. Rao RP, Adams S. Studies of lithium argyrodite solid electrolytes for all-solid-state batteries. *Phys Status Solidi A*. 2011;208(8):1804–1807.
 135. Rayavarapu PR, Sharma N, Peterson VK, Adams S. Variation in structure and Li^+ -ion migration in argyrodite-type $\text{Li}_6\text{PS}_5\text{X}$ ($\text{X} = \text{Cl}, \text{Br}, \text{I}$) solid electrolytes. *J Solid State Electrochem*. 2012;16(5):1807–1813.
 136. Chen HM, Maohua C, Adams S. Stability and ionic mobility in argyrodite-related lithium-ion solid electrolytes. *Phys Chem Chem Phys*. 2015;17(25):16494–16506.
 137. Kraft MA, Culver SP, Calderon M, Böcher F, Krauskopf T, Senyshyn A, Dietrich C, Zevalkink A, Janek J, Zeier WG. Influence of lattice polarizability on the ionic conductivity in the lithium superionic argyrodites $\text{Li}_6\text{PS}_5\text{X}$ ($\text{X} = \text{Cl}, \text{Br}, \text{I}$). *J Am Chem Soc*. 2017;139(31):10909–10918.
 138. Minafra N, Culver SP, Krauskopf T, Senyshyn A, Zeier WG. Effect of Si substitution on the structural and transport properties of superionic Li-argyrodites. *J Mater Chem A*. 2018;6(2):645–651.
 139. Nagata H, Chikusa Y. Activation of sulfur active material in an all-solid-state lithium–sulfur battery. *J Power Sources*. 2014;263:141–144.
 140. Yamasaki H, Shirasawa A, Nishino N. DFT and MD simulations of Li-ion pathway in solid state sulfide $\text{Li}_7\text{P}_3\text{S}_{11}$ electrolyte. *Electrochem Soc Meet Abstr* 2010:600.
 141. Mori K, Enjuji K, Murata S, Shibata K, Kawakita Y, Yonemura M, Onodera Y, Fukunaga T. Direct observation of fast lithium-ion diffusion in a superionic conductor: $\text{Li}_7\text{P}_3\text{S}_{11}$ metastable crystal. *Phys Rev Appl*. 2015;4(5):54008.
 142. Homma K, Yonemura M, Kobayashi T, Nagao M, Hirayama M, Kanno R. Crystal structure and phase transitions of the lithium ionic conductor Li_3PS_4 . *Solid State Ionics*. 2011;182(1):53–58.
 143. Eom M, Kim J, Noh S, Shin D. Crystallization kinetics of $\text{Li}_2\text{S}-\text{P}_2\text{S}_5$ solid electrolyte and its effect on electrochemical performance. *J Power Sources*. 2015;284:44–48.
 144. Zhang Y, Chen R, Liu T, Shen Y, Lin Y, Nan C-W. High capacity, superior cyclic performances in all-solid-state lithium-ion batteries based on $78\text{Li}_2\text{S}-22\text{P}_2\text{S}_5$ glass-ceramic electrolytes prepared via simple heat treatment. *ACS Appl Mater Interfaces*. 2017;9(34):28542–28548.
 145. Hayashi A, Minami K, Tatsumisago M. High lithium ion conduction of sulfide glass-based solid electrolytes and their application to all-solid-state batteries. *J Non-Cryst Solids*. 2009;355(37–42):1919–1923.
 146. He X, Zhu Y, Mo Y. Origin of fast ion diffusion in super-ionic conductors. *Nat Commun*. 2017;8(1):15893.
 147. Brenner TM, Gehrmann C, Korobko R, Livneh T, Egger DA, Yaffe O. Anharmonic host-lattice dynamics enable fast ion conduction in superionic AgI . *Phys Rev Mater*. 2020;4(11):115402.
 148. Schlem R, Bernges T, Li C, Kraft MA, Minafra N, Zeier WG. Lattice dynamical approach for finding the lithium superionic conductor Li_3ErI_6 . *ACS Appl Energy Mater*. 2020;3(4):3684–3691.
 149. Schlem R, Ghidu M, Culver SP, Hansen A-L, Zeier WG. Changing the static and dynamic lattice effects for the improvement of the ionic transport properties within the argyrodite $\text{Li}_6\text{PS}_{5-x}\text{Se}_x\text{I}$. *ACS Appl Energy Mater*. 2020;3(1):9–18.
 150. Bernges T, Culver SP, Minafra N, Koerver R, Zeier WG. Competing structural influences in the Li superionic conducting argyrodites $\text{Li}_6\text{PS}_{5-x}\text{Se}_x\text{Br}$ ($0 \leq x \leq 1$) upon Se substitution. *Inorg Chem*. 2018;57(21):13920–13928.
 151. Koch B, Kong ST, Gün Ö, Deiseroth H-J, Eckert H. Site preferences and ion dynamics in lithium chalcocahide solid solutions with argyrodite structure: II. Multinuclear solid state NMR of the systems $\text{Li}_6\text{PS}_{5-x}\text{Se}_x\text{Cl}$ and $\text{Li}_6\text{PS}_{5-x}\text{Se}_x\text{Br}$. *Z Phys Chem*. 2022;236(6–8):875–898.
 152. Xu Z, Chen X, Chen R, Li X, Zhu H. Anion charge and lattice volume dependent lithium ion migration in compounds with fcc anion sublattices. *Npj Comput Mater*. 2020;6(1):47.
 153. de Klerk NJJ, Rosłoni I, Wagemaker M. Diffusion mechanism of Li argyrodite solid electrolytes for Li-ion batteries and prediction of optimized halogen doping: The effect of Li vacancies, halogens, and halogen disorder. *Chem Mater*. 2016;28(21):7955–7963.

154. Hanghofer I, Brinek M, Eisbacher SL, Bitschnau B, Volck M, Hennige V, Hanzu I, Rettenwander D, Wilkening HMR. Substitutional disorder: Structure and ion dynamics of the argyrodites $\text{Li}_6\text{PS}_5\text{Cl}$, $\text{Li}_6\text{PS}_5\text{Br}$ and $\text{Li}_6\text{PS}_5\text{I}$. *Phys Chem Chem Phys*. 2019;21(16):8489–8507.
155. Adelstein N, Wood BC. Role of dynamically frustrated bond disorder in a Li^+ superionic solid electrolyte. *Chem Mater*. 2016;28(20):7218–7231.
156. Kraft MA, Ohno S, Zinkevich T, Koerver R, Culver SP, Fuchs T, Senyshyn A, Indris S, Morgan BJ, Zeier WG. Inducing high ionic conductivity in the lithium superionic argyrodites $\text{Li}_{6+x}\text{P}_{1-x}\text{Ge}_x\text{S}_5\text{I}$ for all-solid-state batteries. *J Am Chem Soc*. 2018;140(47):16330–16339.
157. Ohno S, Helm B, Fuchs T, Dewald G, Kraft MA, Culver SP, Senyshyn A, Zeier WG. Further evidence for energy landscape flattening in the superionic argyrodites $\text{Li}_{6+x}\text{P}_{1-x}\text{M}_x\text{S}_5\text{I}$ ($\text{M} = \text{Si, Ge, Sn}$). *Chem Mater*. 2019;31(13):4936–4944.
158. Banik A, Liu Y, Ohno S, Rudel Y, Jiménez-Solano A, Gloskovskii A, Vargas-Barbosa NM, Mo Y, Zeier WG. Can substitutions affect the oxidative stability of lithium argyrodite solid electrolytes? *ACS Appl Energy Mater*. 2022;5(2):2045–2053.
159. Maughan AE, Ha Y, Pekarek RT, Schulze MC. Lowering the activation barriers for lithium-ion conductivity through orientational disorder in the cyanide argyrodite $\text{Li}_6\text{PS}_5\text{CN}$. *Chem Mater*. 2021;33(13):5127–5136.
160. Gautam A, Sadowski M, Prinz N, Eickhoff H, Minafra N, Ghidu M, Culver SP, Albe K, Fässler TF, Zobel M, et al. Rapid crystallization and kinetic freezing of site-disorder in the lithium superionic argyrodite $\text{Li}_6\text{PS}_5\text{Br}$. *Chem Mater*. 2019;31(24):10178–10185.
161. Hogrefe K, Minafra N, Hanghofer I, Banik A, Zeier WG, Wilkening HMR. Opening diffusion pathways through site disorder: The interplay of local structure and ion dynamics in the solid electrolyte $\text{Li}_{6+x}\text{P}_{1-x}\text{Ge}_x\text{S}_5\text{I}$ as probed by neutron diffraction and NMR. *J Am Chem Soc*. 2022;144(4):1795–1812.
162. Helm B, Minafra N, Wankmiller B, Agne MT, Li C, Senyshyn A, Hansen MR, Zeier WG. Correlating structural disorder to Li^+ ion transport in $\text{Li}_{4-x}\text{Ge}_{1-x}\text{Sb}_x\text{S}_4$ ($0 \leq x \leq 0.2$). *Chem Mater*. 2022;34(12):5558–5570.
163. Leube BT, Collins CM, Daniels LM, Duff BB, Dang Y, Chen R, Gaultois MW, Manning TD, Blanc F, Dyer MS, et al. Cation disorder and large tetragonal supercell ordering in the Li-rich argyrodite $\text{Li}_7\text{Zn}_{0.5}\text{SiS}_6$. *Chem Mater*. 2022;34(9):4073–4087.
164. Schweiger L, Hogrefe K, Gadermaier B, Rupp JLM, Wilkening HMR. Ionic conductivity of nanocrystalline and amorphous $\text{Li}_{10}\text{GeP}_2\text{S}_{12}$: The detrimental impact of local disorder on ion transport. *J Am Chem Soc*. 2022;144(22):9597–9609.
165. Dawson JA, Islam MS. A nanoscale design approach for enhancing the Li-ion conductivity of the $\text{Li}_{10}\text{GeP}_2\text{S}_{12}$ solid electrolyte. *ACS Mater Lett*. 2022;4(2):424–431.
166. Fang H, Jena P. Li-rich antiperovskite superionic conductors based on cluster ions. *Proc Natl Acad Sci*. 2017;114(42):11046–11051.
167. Jansen M. Volume effect or paddle-wheel mechanism—Fast alkali-metal ionic conduction in solids with rotationally disordered complex anions. *Angew Chem Int Ed Engl*. 1991;30(12):1547–1558.
168. Nilsson L, Thomas JO, Tofield BC. The structure of the high-temperature solid electrolyte lithium sulphate at 908K. *J Phys C Solid State Phys*. 1980;13(35):6441.
169. Zhao Q, Pan L, Li Y-J, Chen L-Q, Shi S-Q. Rotational motion of polyanion versus volume effect associated with ionic conductivity of several solid electrolytes. *Rare Metals*. 2018;37(6):497–503.
170. Lin S, Lin Y, He B, Pu B, Ren Y, Wang G, Luo Y, Shi S. Reclaiming neglected compounds as promising solid state electrolytes by predicting electrochemical stability window with dynamically determined decomposition pathway. *Adv Energy Mater*. 2022;12(45):2201808.
171. Ren Y, Liu B, He B, Lin S, Shi W, Luo Y, Wang D, Shi S. Portraying the ionic transport and stability window of solid electrolytes by incorporating bond valence-Ewald with dynamically determined decomposition methods. *Appl Phys Lett*. 2022;121(17):173904.
172. Shi S, Lu P, Liu Z, Qi Y, Hector LG Jr, Li H, Harris SJ. Direct calculation of Li-ion transport in the solid electrolyte interphase. *J Am Chem Soc*. 2012;134(37):15476–15487.
173. Aono H, Sugimoto E, Sadaoka Y, Imanaka N, Adachi G. Ionic conductivity and sinterability of lithium titanium phosphate system. *Solid State Ionics*. 1990;40–41:38–42.
174. Zhang Z, Zou Z, Kaup K, Xiao R, Shi S, Avdeev M, Hu Y-S, Wang D, He B, Li H, et al. Correlated migration invokes higher Na^+ -ion conductivity in NaSICON-type solid electrolytes. *Adv Energy Mater*. 2019;9(42):1902373.
175. Zou Z, Ma N, Wang A, Ran Y, Song T, Jiao Y, Liu J, Zhou H, Shi W, He B, et al. Relationships between Na^+ distribution, concerted migration, and diffusion properties in rhombohedral NaSICON. *Adv Energy Mater*. 2020;10(30):2001486.
176. Gao J, Chu G, He M, Zhang S, Xiao R, Li H, Chen L. Screening possible solid electrolytes by calculating the conduction pathways using Bond Valence method. *Sci China Phys Mech Astron*. 2014;57(8):1526–1536.
177. Wang A, Zou Z, Wang D, Liu Y, Li Y, Wu J, Avdeev M, Shi S. Identifying chemical factors affecting reaction kinetics in Li-air battery via *ab initio* calculations and machine learning. *Energy Storage Mater*. 2021;35:595–601.
178. Zou Z, Li Y, Lu Z, Wang D, Cui Y, Guo B, Li Y, Liang X, Feng J, Li H, et al. Mobile ions in composite solids. *Chem Rev*. 2020;120(9):4169–4221.
179. Hu J-M, Wang B, Ji Y, Yang T, Cheng X, Wang Y, Chen L-Q. Phase-field based multiscale modeling of heterogeneous solid electrolytes: Applications to nanoporous Li_3PS_4 . *ACS Appl Mater Interfaces*. 2017;9(38):33341–33350.
180. Hong Z, Viswanathan V. Open-sourcing phase-field simulations for accelerating energy materials design and optimization. *ACS Energy Lett*. 2020;5(10):3254–3259.
181. Hong Z, Viswanathan V. Phase-field simulations of lithium dendrite growth with open-source software. *ACS Energy Lett*. 2018;3(7):1737–1743.
182. Ran Y, Zhao Z-Y, Zhao Q, Wang D, Yu J, Shi S-Q. Brief overview of microscopic physical image of ion transport in electrolytes. *Acta Phys Sin*. 2020;69(22):226601.
183. Yu C, Zhao F, Luo J, Zhang L, Sun X. Recent development of lithium argyrodite solid-state electrolytes for solid-state batteries: Synthesis, structure, stability and dynamics. *Nano Energy*. 2021;83:105858.
184. Chen X, Guan Z, Chu F, Xue Z, Wu F, Yu Y. Air-stable inorganic solid-state electrolytes for high energy density lithium batteries: Challenges, strategies, and prospects. *InfoMat*. 2022;4(1):e12248.

185. Tao B, Ren C, Li H, Liu B, Jia X, Dong X, Zhang S, Chang H. Thio-/LISICON and LGPS-type solid electrolytes for all-solid-state lithium-ion batteries. *Adv Funct Mater.* 2022;32(34):2203551.
186. Kato Y, Hori S, Kanno R. $\text{Li}_{10}\text{GeP}_2\text{S}_{12}$ -type superionic conductors: Synthesis, structure, and ionic transportation. *Adv Energy Mater.* 2020;10(42):2002153.
187. Meng YS, Srinivasan V, Xu K. Designing better electrolytes. *Science.* 2022;378(6624):eabq3750.
188. Wang C, Fu K, Kammampata SP, McOwen DW, Samson AJ, Zhang L, Hitz GT, Nolan AM, Wachsman ED, Mo Y, et al. Garnet-type solid-state electrolytes: Materials, interfaces, and batteries. *Chem Rev.* 2020;120(10):4257–4300.
189. Tufail MK, Shah SSA, Hussain S, Najam T, MK Aslam. Chapter 12—A solid-state approach to a lithium-sulfur battery. In: Hepp AF, Kumta PN, Velikokhatnyi OI, Datta MK, editors. *Lithium-sulfur batteries*. Amsterdam (Netherlands): Elsevier; 2022. p. 441–488.
190. Famprikis T, Canepa P, Dawson JA, Islam MS, Masquelier C. Fundamentals of inorganic solid-state electrolytes for batteries. *Nat Mater.* 2019;18(12):1278–1291.
191. Kim KJ, Balaish M, Wadaguchi M, Kong L, Rupp JLM. Solid-state Li–metal batteries: Challenges and horizons of oxide and sulfide solid electrolytes and their interfaces. *Adv Energy Mater.* 2021;11(1):2002689.
192. Krauskopf T, Culver SP, Zeier WG. Bottleneck of diffusion and inductive effects in $\text{Li}_{10}\text{Ge}_{1-x}\text{Sn}_x\text{P}_2\text{S}_{12}$. *Chem Mater.* 2018;30(5):1791–1798.
193. Awaka J, Kijima N, Hayakawa H, Akimoto J. Synthesis and structure analysis of tetragonal $\text{Li}_7\text{La}_3\text{Zr}_2\text{O}_{12}$ with the garnet-related type structure. *J Solid State Chem.* 2009;182(8):2046–2052.
194. Chang D, Oh K, Kim SJ, Kang K. Super-ionic conduction in solid-state $\text{Li}_7\text{P}_3\text{S}_{11}$ -type sulfide electrolytes. *Chem Mater.* 2018;30(24):8764–8770.
195. Kaupp M, Metz B, Stoll H. Breakdown of bond length-bond strength correlation: A case study. *Angew Chem Int Ed.* 2000;39(24):4607–4609.
196. Muy S, Schlem R, Shao-Horn Y, Zeier WG. Phonon–ion interactions: Designing ion mobility based on lattice dynamics. *Adv Energy Mater.* 2021;11(15):2002787.